Diffusion MRI Modeling: Theory and Applications

By

A. Pasha Hosseinbor

A DISSERTATION SUBMITTED IN PARTIAL FULFILLMENT

OF THE REQUIREMENTS FOR THE DEGREE OF

Doctor of Philosophy

(Medical Physics)

at the

UNIVERSITY OF WISCONSIN – MADISON

2013

Date of final oral examination: 06/21/13

The dissertation is approved by the following members of the Final Oral Committee:

Andrew L. Alexander, Professor, Medical Physics

Barbara B. Bendlin, Assistant Professor, Medicine

Moo K. Chung, Associate Professor, Biostatistics and Medical Informatics

M. Elizabeth Meyerand, Professor, Medical Physics

Oliver Wieben, Assistant Professor, Medical Physics

Contents

List of Figures

List of Tables

Chapter 1

Introduction

1.1 Thesis Abstract

Diffusion magnetic resonance imaging (dMRI) is a non-invasive modality that quantifies the diffusion of water molecules in biological tissues, and thereby capable of probing tissue microstructure. An important mathematical descriptor of the diffusion profile is the ensemble average propagator (EAP), which describes the 3D average diffusion process of water molecules and possesses rich information regarding tissue architecture. The EAP is related to the measured MR signal attenuation by the Fourier transform. In this thesis we present two novel linear algorithms, each modeling the signal attenuation by a unique orthonormal basis, to estimate the EAP in dMRI: Bessel Fourier orientation reconstruction (BFOR) and the 4D hyperspherical harmonics (HSH). BFOR is an analytical EAP reconstruction scheme, while the HSH representation numerically estimates the EAP. Both methods can be used to estimate various clinically relevant quantitative

features of the 3D diffusion profile. A significant portion of this thesis is dedicated to validating these two methods in synthetic and *in vivo* datasets and comparing them to existing analytical EAP algorithms. We will demonstrate that the proposed methods are better or just as effective as existing ones, and that the HSH representation may be more appropriate to sparser sampling schemes than BFOR.

1.2 Motivation

Up until recently, the only way anatomists could obtain information about human brain anatomy, particularly cerebral white matter, was through cerebral dissection. However, since its inception in the late 1980s, diffusion magnetic resonance imaging (dMRI) has emerged as a unique non-invasive technique capable of quantifying the diffusion of water molecules in biological tissues like cerebral white matter. Depending on the structure of the tissue, water diffusion can be isotropic or anisotropic. In fibrous structures such as white matter, water molecules tend to diffuse along the fibers, whereas in cerebrospinal fluid they display no directional preference. By capturing the average diffusion of water molecules in biological tissues, dMRI is able to retrieve information about neural architecture *in vivo*.

The most widely used dMRI modality is diffusion tensor imaging (DTI) [18], which assumes that the 3D nature of diffusion anisotropy in tissues obeys a Gaussian distribution. The Gaussian assumption enables the anisotropy to be characterized by a 3 x 3 symmetric, positive definite matrix, termed the diffusion tensor. However, the Gaussian assumption over-simplifies water diffusion in biological tissues and thus has significant limitations. While the Gaussian assumption is sufficient for voxels containing a single

fiber orientation, it collapses for voxels with an intricate internal structure (e.g. multiple fiber orientations). In addition, although Gaussian diffusion is observed in biological tissues under certain experimental conditions, water diffusion also exhibits non-Gaussian behavior. For example, the movement of water molecules is restricted by various barriers such as axonal membranes and myelin sheaths, causing the diffusion to deviate from a Gaussian behavior.

The diffusion tensor is inextricably linked to Gaussian diffusion. A mathematical descriptor of the diffusion profile that does not invoke a specific assumption of diffusion behavior is needed to characterize complex neural architecture and describe non-Gaussian phenomena (e.g. restricted diffusion). One such descriptor is the ensemble average propagator (EAP), which describes the displacement distribution of diffusing water molecules. Many quantitative features of the diffusion profile can be derived from the EAP, and its reconstruction has become a major area of investigation within the (computational) dMRI community in recent years [29, 37, 59, 75, 80].

EAP imaging forms the heart of this thesis. Specifically, we will introduce a novel analytical EAP reconstruction scheme termed Bessel Fourier orientation reconstruction (BFOR). BFOR provides dMRI with a solid foundation, facilitating fast analytical computation of the EAP and various quantitative features of the diffusion profile. In addition to BFOR, we will also introduce a 4D hyperspherical harmonic (HSH) interpretation of the diffusion profile, which may be better suited to sparser sampling schemes than BFOR.

1.3 Outline and Original Contributions

In Chapters 2-4, we review the basic phyiscs of MRI (Chapter 2) and diffusion (Chapter 3), and provide an overview of dMRI techniques (Chapter 4). In Chapter 5, we introduce the BFOR technique, which we employ in a small clinical study investigating multiple sclerosis (MS) (Chapter 6). In Chapter 7, we develop a 4D hyperspherical interpretation of the 3D diffusion profile by introducing another mathematical representation of the EAP, the 4D HSH, which we compare to BFOR.

The contributions of this thesis are listed as follows:

1. The development of a fast, linear, robust, and analytical EAP reconstruction algorithm, termed Bessel Fourier orientation reconstruction (BFOR), for multiple b-value imaging.

2. Derivation of a general relationship between the q-space signal and the mean squared displacement (MSD)

3. Introduction of novel EAP metrics, such as the generalized fractional anisotropy (GFA) and q-space inverse variance (QIV).

4. Use of heat diffusion smoothing and signal extrapolation to mitigate the effects of noise and truncation artifacts/Gibbs' ringing, respectively.

5. Comparison of BFOR to other, well-established analytical EAP techniques, and thereby demonstrating that BFOR is better or just as effective as these existing methods.

6. The first clinical implementation of an analytical EAP reconstruction technique.

7. Introduction of a novel orthonormal basis, the 4D hyperspherical harmonics (HSH), for q-space signal and orientation distribution function (ODF) reconstructions.

8. The development of a 4D hyperspherical interpretation of the diffusion profile.

9. Derivation of a novel hyperspherical diffusivity metric, termed the mean chordal squared difference (MCSD).

10. Comparison of HSH basis to BFOR for signal and ODF reconstructions, and thereby demonstrating that HSH expends less fitting parameters than BFOR to achieve comparable signal and better ODF reconstructions.

Chapter 2

Physics of Magnetic Resonance

Magnetic resonance imaging (MRI) is a non-invasive medical imaging technique used to visualize the body's anatomical structures in detail. The main component of any MRI scanner is a powerful magnet used to expose a patient to a uniform magnetic field. MRI takes advantage of the fact that most of the human body is composed of water, and hence protons (^{1}H). Each water molecule has two hydrodgen nuclei or protons. When a patient is exposed to the scanner's powerful magnetic field, a slight majority of the protons become aligned in the direction of the field, inducing a net magnetization. In this chapter, we will explore in detail the underlying physics behind the induction of this equilibrium magnetization and its eventual transformation into a readable MR signal.

2.1 Review of Thermodynamics

Suppose we have a thermodynamically large system that is in constant thermal contact with the environment, with a temperature T, and both the volume of the system and the number of constituent particles are fixed. Let us label the exact states (microstates) that the system can occupy as j ($j = 1, 2, 3, ...$), and denote the total energy of the system when it is in microstate s as E_s. The canonical partition function of the system is then defined as

$$Z = \sum_j e^{-\frac{E_j}{k_B T}}, \tag{2.1}$$

where k_B denotes the Boltzmann's constant[1]. The term $e^{-\frac{E_j}{k_B T}}$ is known as the Boltzmann factor and is the mathematical representation of a microstate. The partition function can be viewed as a weighted (by energy) count of the number of states a system can occupy.

The probability P_j that the system occupies a particular microstate having energy E_j is

$$P_j \equiv P(E_j) = \frac{e^{-\frac{E_j}{k_B T}}}{Z} \tag{2.2}$$

We can interpret P_j in another way: if our system is composed of N particles and N_j

[1]The letter Z stands for the German word *Zustandssumme*, "sum over states." This notation illuminates another meaning of the partition function of a system: it is the weighted (by energy) sum of the microstates a system can occupy, where the microstate is described by the Boltzmann factor.

of these have energy E_j, then the probability that a randomly chosen particle occupies microstate E_j is $\frac{N_j}{N} = P_j$. The partition function plays the role of a normalizing constant in Eq. (2.2), ensuring that the probabilities add up to unity:

$$\sum_j P_j = \frac{1}{Z}\sum_j e^{-\frac{E_j}{k_B T}} = \frac{1}{Z} Z = 1$$

Hence, if all microstates are equally probable (equal energies), then the partition function is simply the total number of possible microstates.

The average energy of the system is

$$\langle E \rangle = \sum_j E_s P_j = \frac{1}{Z}\sum_j E_j e^{-\frac{E_j}{k_B T}} = \frac{k_B T^2}{Z}\frac{\partial Z}{\partial T}$$

2.2 Spin

Spin is an intrinsic form of angular momentum carried by electrons, protons, and neutrons. It is a solely quantum mechanical phenomenon, as spin has no counterpart in classical mechanics. Spin is one of two types of angular momentum that arise in quantum mechanics, the other being orbital angular momentum. Orbital angular momentum is the quantum mechanical analogue to the classical notion of angular momentum. The existence of spin angular momenum was verified by the Stern-Gerlach experiment.

In this section, we employ the following notation: $\vec{S}$ denotes the spin angular momentum, s denotes the spin quantum number (analogous to the orbital angular momentum quantum number l), and m_s the secondary spin quantum number. m_s ranges from $-s$ to $+s$ in steps of one, which generates $2s+1$ different values of m_s for a given s.

2.2.1 Spin Quantum Number

The spin quantum number s can assume both non-negative integer and, unlike the orbital angular momentum quantum number, half-integer values. Particles with half-integer spins, such as 1/2, 3/2, 5/2, are known as fermions, while those particles with integer spins, such as 0, 1, 2, are known as bosons. Electrons, neutrons, and protons are spin-1/2 particles, i.e. $s = 1/2$.

2.2.2 Spin Magnetic Moment

Any particle that possesses spin constitutes a magnetic moment, i.e. a particle's spin induces a spin magnetic moment. The spin magnetic moment, which we denote $\vec{\mu}_S$, for a sub-atomic particle of charge q, mass m, and spin angular momentum $\vec{S}$ is

$$\vec{\mu}_S = g\frac{q}{2m}\vec{S}, \tag{2.3}$$

where g is a dimensionless number, termed the g-factor, that depends on the particle. A particle's gyromagnetic ratio, γ, is defined as the ratio of the particle's magnetic moment to its total angular momentum. In the case where a particle's angular momentum is based soley on spin, i.e. no orbital angular momentum, the gyromagnetic ratio is then

$$\gamma = \frac{\vec{\mu}_S}{\vec{S}} = g\frac{q}{2m}$$

The gyromagnetic ratio of a proton (i.e. hydrogen nucleus) is γ_p = 2.67513e8 rad s^{-1} T^{-1}.

2.2.3 Spin Microstates

According to quantum mechanics, the component of angular momentum along any direction is quantized, i.e. can only take on discrete values:

$$S_i = \hbar m_s, \qquad m_s \in \{-s, -(s-1), ..., s-1, s\},$$

where S_i is the spin component along the i-axis (either x, y, or z) and $\hbar$ is the reduced Planck constant. Conventionally, the direction of $\vec{S}$ is chosen to be the z-axis:

$$S_z = \hbar m_s, \tag{2.4}$$

where S_z is the spin angular momentum component along the z-axis. For the rest of this chapter, we will adopt the convention of the spin direction being along the z-axis.

As mentioned previously, there are $2s + 1$ possible values of m_s for a given s. For a spin-1/2 particle then, there are only two possible values: $m_s = +1/2$ and $m_s = -1/2$. These m_s values correspond to quantum states in which the direction of spin is pointing along the $+z$ or $-z$ directions, respectively, and are often referred to as "spin up" and "spin down".

2.3 Spin Behavior in a Magnetic Field

Consider a system of N spin-1/2 particles, say protons. Since a proton possesses spin, it constitutes a magnetic moment, which is given by

$$\vec{\mu}_p = \gamma_p \vec{S} \tag{2.5}$$

In the absence of any external forces, the protons' spins are oriented randomly and so the net macroscopic magnetic moment of the system is zero. Lets expose our system to a uniform, external magnetic field $\vec{B} = B_o \hat{z}$. By convention, the direction of the applied field is called the longitudinal direction. The energy of a magnetic moment placed in an external magnetic field $\vec{B}$ is

$$E = -\vec{\mu}_p \cdot \vec{B} \tag{2.6}$$

Thus, the energy of an individual proton is

$$E = -\gamma_p B_o S_z = -m_s \gamma_p \hbar B_o \tag{2.7}$$

where we have taken $\vec{S} = S_z \hat{z}$. The proton can occupy one of two possible quantum states: spin up ($m_s = +1/2$) or spin down ($m_s = -1/2$). Thus, the proton can assume two possible energy values:

$$E_1 = -\frac{\gamma_p B_o \hbar}{2} \qquad \text{(Spin Up)}$$
$$E_2 = +\frac{\gamma_p B_o \hbar}{2} \qquad \text{(Spin Down)}$$

Spin up, thus, is the low energy state. These two energy states are separated by

$$\Delta E = \gamma_p \hbar B_o,$$

and this energy splitting is illustrated in Fig. 2.1.

The partition function for a single proton in this system is

$$Z = \sum_{j=1}^{2} e^{-\frac{E_j}{k_B T}} = 2\cosh\left(\frac{\gamma_p B_o \hbar}{2k_B T}\right) \tag{2.8}$$

The fraction of protons in the spin up state, i.e. probability a randomly chosen proton from the system is in spin up state, is

$$\frac{N_+}{N} = \frac{e^{\gamma_p \hbar B_o / 2k_B T}}{2\cosh\left(\frac{\gamma_p B_o \hbar}{2k_B T}\right)}, \tag{2.9}$$

while the fraction of protons in the spin down state is

$$\frac{N_-}{N} = \frac{e^{-\gamma_p \hbar B_o / 2k_B T}}{2\cosh\left(\frac{\gamma_p B_o \hbar}{2k_B T}\right)} \tag{2.10}$$

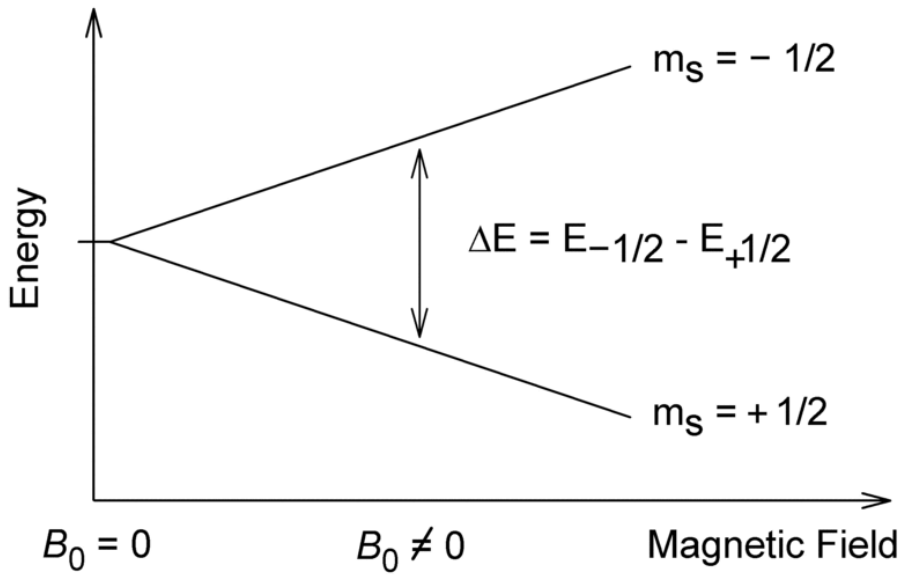

Figure 2.1: Consider a spin-1/2 particle. The particle then has two possible spin states: $m_s = 1/2$ and $m_s = -1/2$. In the absence of any external forces, these two states are degenerate - that is, they have the same energy - and so according to Eq. (2.2) the particle is equally likely to occupy any of the two states. When the particle is placed in a uniform magnetic field, the interaction between the particle's spin magnetic moment and the external magnetic field results in the two spin states having differing energies. These two spin states are now separated by ΔE, with spin up being the lowest energy state. Consequently, the particle is more likely to occupy the spin up state.

Note that $\frac{N_+}{N} > \frac{N_-}{N}$, indicating that a proton is more likely (higher probability) to be in the spin up state than spin down. The ratio of spin up protons to spin down ones is

$$\frac{N_+}{N_-} = \frac{e^{\gamma_p \hbar B_o/2k_BT}}{e^{-\gamma_p \hbar B_o/2k_BT}} = e^{\Delta E/k_BT}, \tag{2.11}$$

which indicates that there are more protons in the spin up state, i.e. the majority of protons will align themselves parallel to B_o instead of anti-parallel. Consequently, there will be a net magnetization along the $+z$-direction. For a system of protons at room temperature with magnetic field of 3 T, the ratio of spin up protons to spin down is about 1.00002057. Many, many protons are then needed in order to have a physically detectable magnetization.

The mean magnetic moment of the proton is

$$\begin{aligned}\langle \mu_p \rangle = \frac{1}{Z}\sum_{j=1}^{2} \mu_{p,j} e^{-\frac{E_j}{k_BT}} &= \frac{\frac{\gamma_p \hbar}{2}\left[e^{\gamma_p \hbar B_o/2k_BT} - e^{-\gamma_p \hbar B_o/2k_BT}\right]}{2\cosh\left(\frac{\gamma_p B_o \hbar}{2k_BT}\right)} \\ &= \frac{\gamma_p \hbar}{2}\tanh\left(\frac{\gamma_p B_o \hbar}{2k_BT}\right),\end{aligned} \tag{2.12}$$

where μ_p is the magnitute of the magnetic moment and we have used the fact that

$$\begin{aligned}\vec{\mu}_{p,1} &= -\frac{\gamma_p \hbar}{2}\hat{z} \qquad \text{(Spin Up)} \\ \vec{\mu}_{p,2} &= +\frac{\gamma_p \hbar}{2}\hat{z} \qquad \text{(Spin Down)}\end{aligned}$$

The bulk (mean) magnetization of the system is defined as

$$M = \frac{N}{V}\langle \mu_p \rangle, \tag{2.13}$$

where V is the volume of the system. Substituting Eq. (2.12) into (2.13), we have

$$M_z = \frac{\gamma_p \hbar N}{2V} \tanh\left(\frac{\gamma_p B_o \hbar}{2k_B T}\right) \tag{2.14}$$

Note that for argument x, $\tanh x \approx x$ when x is very small. Hence, when $\frac{\gamma_p B_o \hbar}{2k_B T}$ is very small, i.e. $\frac{\gamma_p B_o \hbar}{2} \ll k_B T$, the magnetization assumes a simpler form:

$$M_z \approx \frac{N}{V}\frac{\gamma_p^2 \hbar^2 B_o}{4k_B T}, \qquad \left(\frac{\gamma_p B_o \hbar}{2} \ll k_B T\right) \tag{2.15}$$

We can summarize this section as follows. We have N protons exposed to a uniform, magnetic field $B_o\hat{z}$. Such a scenerio is an example of a binary system because a proton can assume one of two possible states: spin up ($+z$-direction) or spin down ($-z$-direction). The system reaches thermal equilibrium when a majority of the protons' spins are aligned parallel to B_o, i.e. occupying spin up state, and so inducing a net magnetization along the $+z$-direction.

2.4 Precession

When a magnetic moment $\vec{\mu}$ is placed in an external magnetic field $\vec{B}$, the field exerts a torque on the moment given by

$$\vec{\tau} = \vec{\mu} \times \vec{B} \tag{2.16}$$

From classical mechanics, we know that

$$\vec{\tau} = \frac{d\vec{J}}{dt},$$

where $\vec{J} = \vec{L} + \vec{S}$ is the total angular momentum of our magnetic moment. Assuming it possesses no orbital angular momentum, i.e. $\vec{L} = 0$, we have

$$\vec{\tau} = \frac{d\vec{S}}{dt} = \frac{1}{\gamma}\frac{d\vec{\mu}}{dt} \tag{2.17}$$

Equating Eq. (2.16) and (2.17), we have

$$\frac{d\vec{\mu}}{dt} = \vec{\mu} \times \gamma\vec{B} \tag{2.18}$$

The quantity $\gamma\vec{B}$ has units of rad/s, implying that it's an angular frequency. In fact, $\vec{\omega} = \gamma\vec{B}$ is called the Larmor frequency, and it's the frequency at which the magnetic moment precess about $\vec{B}$. If we take $\vec{B} = B_o\hat{z}$, as in Sec. 2.3, then our magnetic moment precesses about the z-axis at frequency $\omega_o = \gamma B_o$, where $\|\vec{\omega}\| = \omega_o$.

Eq. (2.18) is pertinent to a single magnetic moment. For a macroscopic sample, however, it is more useful to focus on the magnetic moments per unit volume, or magnetization $\vec{M}$. For a system of volume V and composed of N magnetic moments, the magnetization is defined as

$$\vec{M} = \frac{1}{V}\sum_{j=1}^{N}\vec{\mu}_j = \frac{N}{V}\langle\vec{\mu}\rangle \tag{2.19}$$

If the system is composed of N identical magnetic moments, then $\vec{M} = \frac{N}{V}\vec{\mu}$. Collectively, we can write Eq. (2.18) as

$$\begin{aligned}
\frac{d\vec{\mu}_j}{dt} &= \gamma\vec{\mu}_j \times \vec{B} \\
\sum_{j=1}^{N}\frac{d\vec{\mu}_j}{dt} &= \sum_{j=1}^{N}\gamma\vec{\mu}_j \times \vec{B} \\
\frac{1}{V}\sum_{j=1}^{N}\frac{d\vec{\mu}_j}{dt} &= \frac{1}{V}\sum_{j=1}^{N}\gamma\vec{\mu}_j \times \vec{B} \\
\frac{d\vec{M}}{dt} &= \gamma\vec{M} \times \vec{B} = \vec{M} \times \vec{\omega}
\end{aligned} \tag{2.20}$$

Eq. (2.20) describes the Larmor precession of the nuclear magnetization $\vec{M}$ in an external magnetic field.

Lets solve Eq. (2.20) for the case where $\vec{B} = B_o\hat{z}$. We adopt the following notation:

$$\vec{M} = M_x\hat{x} + M_y\hat{y} + M_z\hat{z} = \vec{M}_{xy} + M_z\hat{z}$$
$$\vec{M}_{\perp} = M_x\hat{x} + M_y\hat{y},$$

where $\vec{M}_{\perp}$ denotes the transverse magnetization. As shown in Sec. 2.3, the spins will either align parallel or anti-parallel to B_o, so $\vec{M}_{\perp} = \mathbf{0}$ in this scenerio. Hence, we only need to focus on the longitudinal direction and Eq. (2.20) reduces to

$$\frac{dM_z}{dt} = 0, \tag{2.21}$$

which indicates that the longitudinal magnetization is constant with time. Eq. (2.14) is such a solution, and according to Eq. (2.20), it will precess about B_o at the Larmor frequency.

2.5 Excitation: Radiofrequency Field $\vec{B}_1$

In sections 2.3 and 2.4, we showed two notable effects occur when a collection of protons are exposed to an external magnetic field B_o. First, the protons' magnetic moments tend to align in the direction of B_o to induce a net magnetization, i.e. Eq. (2.14). Second, the net magnetization precesses about B_o at the Larmor frequency $\omega_o = \gamma_p B_o$. However, we can't physically measure this longitudinal magnetization as it does not constitute a readable signal.

To obtain a readable signal, a radiofrequency (RF) magnetic pulse $\vec{B}_1$ tuned to the Larmor frequency of the spins is applied in the xy (transverse) plane to excite the spins out of equilibrium. When the frequency of the RF pulse matches ω_o, resonance is said to occur. From a classical point of view, $\vec{B}_1$ applies a torque which "flips" the longitudinal magnetization vector by a prescribed angle away from its equilibrium position along z. Quantum mechanically, resonance results in the RF pluse imparting energy to the protons (excitation), causing their spins to flip away from the longitudinal direction. The flip angle is dependent on the strength of $\vec{B}_1$ and its duration. In a typical MRI system, $B_1 \ll B_o$ and the duration of B_1 is usually only a few milliseconds.

Tipping the equilibrium magnetization by any angle between 0° and 180° will result in a component of it lying in the transverse plane. If the excitation is set for a 90° flip angle, then upon turning off the RF pulse, the entire longitudinal magnetization has been flipped onto the transverse plane, where it then precesses in the xy-plane about B_o at the Larmor frequency.

Now given a transverse magnetization component, detection of the magnetization, and hence obtaining a readable signal, becomes possible via Faraday's law of induction. The same RF coil used to generate the RF pulse B_1 can be used to detect the precessing magnetization in the xy-plane. This detection occurs because the precessing magnetization, which constitutes a time varying magnetic field, induces a change in flux Φ through the coil, thereby creating an electromotive force (EMF) ϵ, where

$$\epsilon = -\frac{\partial \Phi}{\partial t} \tag{2.22}$$

The resulting time signal is called a free induction decay (FID) and represents the basic

MR signal that is recorded.

2.6 Relaxation

Eq. (2.20) is no longer valid after the application of a RF pulse. For convenience, lets assume the flip angle is 90°. When turned on, the RF pulse flips the longitudinal magnetization, i.e. Eq. (2.14), onto the transverse plane. Right after the RF pulse is turned off, two important processes arise: 1) the transverse component of the magnetization decays away, while 2) the longitudinal component returns to its thermal equilibrium state. These two processes are collectively termed relaxation phenomena, and Eq. (2.20) needs to be corrected by taking them into account.

2.6.1 Spin-Lattice Relaxation

After the magnetization has been flipped 90° onto the transverse plane, the longitudinal component becomes zero. Spin-lattice relaxation is the mechanism by which the longitudinal magnetization returns to its thermal equilibrium state, i.e. the state before the RF pulse was turned on, as given by Eq. (2.14). The recovery of the longitudinal component behaves according to

$$\frac{dM_z}{dt} = -\frac{M_z - M_o}{T_1}, \tag{2.23}$$

where M_o is the equilibrium magnetization and the spin-lattice relaxation time T_1 denotes the rate at which the longitudinal magnetization is recovered. The solution is

$$M_z(t) = M_o + (M_z(t=0) - M_o)e^{-t/T_1} \tag{2.24}$$

If the flip angle is 90°, then $M_z(0) = 0$; hence,

$$M_z = M_o(1 - e^{-t/T_1})$$

2.6.2 Spin-Spin Relaxation

The behavior of the transverse component of magnetization is descibed by

$$\frac{d\vec{M}_\perp}{dt} = \gamma\vec{M}_\perp \times \vec{B} - \frac{1}{T_2}\vec{M}_\perp, \tag{2.25}$$

where T_2 is the spin-spin relaxation time that characterizes the rate at which the transverse magnetization decays. For $\vec{B} = B_o$, Eq. (2.25) can be broken down to

$$\frac{dM_x}{dt} = \omega_o M_y - \frac{M_x}{T_2}$$
$$\frac{dM_y}{dt} = -\omega_o M_x - \frac{M_y}{T_2}$$

The solution to this system of coupled differential equations is

$$\begin{aligned} M_x(t) &= e^{-t/T_2}\left(M_x(0)\cos\omega_o t + M_y(0)\sin\omega_o t\right) \\ M_y(t) &= e^{-t/T_2}\left(M_y(0)\cos\omega_o t - M_x(0)\sin\omega_o t\right) \end{aligned} \tag{2.26}$$

A more simplified solution can be found if we treat M_x and M_y together instead of separately. Define

$$M_{xy} = M_x + iM_y \tag{2.27}$$

Then

$$\begin{aligned} \frac{dM_x}{dt} + i\frac{dM_y}{dt} &= \omega_o M_y - \frac{M_x}{T_2} - i\omega_o M_x - i\frac{M_y}{T_2} \\ \frac{d}{dt}\left(M_x + iM_y\right) &= \omega_o(M_y - iM_x) - \frac{1}{T_2}(M_x + iM_y) \\ \frac{dM_{xy}}{dt} &= -M_{xy}(i\omega_o + \frac{1}{T_2}) \end{aligned} \tag{2.28}$$

The solution to Eq. (2.28) is

$$M_{xy} = M_{xy}(0)e^{-i\omega_o t}e^{-t/T_2} \tag{2.29}$$

Taking the magnitude of $\tilde{M}$, we obtain

$$\|M_{xy}\| = M_o e^{-t/T_2}, \tag{2.30}$$

where we used the fact that for a 90° flip angle $\|M_{xy}(t=0)\| = M_o$. $\|M_{xy}\|$ is the signal we actually measure via the RF receiver coil, and is often termed the nuclear magnetic resonance (NMR) signal. Hence, Eq. (2.30) is the theoretical FID (i.e. what we expect it to be).

2.7 Bloch Equation

Combining Eqs. (2.23) and (2.25), we obtain the phenomenological Bloch equation [22], which completely describes the dynamics of nuclear magnetization:

$$\frac{d\vec{M}}{dt} = \gamma\vec{M} \times \vec{B} - \frac{M_x\hat{x} + M_y\hat{y}}{T_2} - \frac{M_z - M_o}{T_1}\hat{z} \tag{2.31}$$

Note that we solve Eq. (2.31) after the RF pulse has been turned off. If no RF pulse is applied, it reduces to Eq. (2.20).

If $\vec{B} = B_o\hat{z}$, then the solutions to Eq. (2.31) are given by Eqs. (2.24) and. The Bloch equation, for this specific case, can be written in matrix form as

$$\begin{pmatrix} \frac{dM_x}{dt} \\ \frac{dM_y}{dt} \\ \frac{dM_z}{dt} \end{pmatrix} = \begin{pmatrix} -1/T_2 & \gamma B_o & 0 \\ -\gamma B_o & -1/T_2 & 0 \\ 0 & 0 & -1/T_1 \end{pmatrix} \begin{pmatrix} M_x \\ M_y \\ M_z \end{pmatrix} + \begin{pmatrix} 0 \\ 0 \\ \frac{M_o}{T_1} \end{pmatrix}$$

2.8 Linear Magnetic Field Gradients

Thus far, we have described NMR. If the applied field is simply the main static field $B_o\hat{z}$, then all the spins possess the same Larmor frequency $\omega_o = \gamma B_o$. After application of an RF pulse, we measure an NMR signal via the decay of the transverse magnetization component, but this signal contains no particular spatial information. That is, we can not determine the specific origin of each component of the signal. In order to move from NMR to MRI, the signal needs to be spatially localized.

A gradient makes the magnetic field vary from one point to another. Hence, a gradient spatially localizes each magnetic moment, encoding each of them with a unique position and frequency. Consequently, we can distinguish the signal component generated from each magnetic moment.

2.8.1 Static Gradient Field

The simplest but most common and important case of a non-uniform magnetic field is a static (no time dependence) gradient field, which is a field pointing in the z-direction (as is B_o) but with an amplitude that varies with position, i.e $B_z(x, y, z)\hat{z}$. The gradient of B_z is defined mathematically as

$$\begin{aligned} \bigtriangledown B_z &= \frac{dB_z}{dx}\hat{x} + \frac{dB_z}{dy}\hat{y} + \frac{dB_z}{dz}\hat{z} \\ &= G_x\hat{x} + G_y\hat{y} + G_z\hat{z}, \end{aligned} \tag{2.32}$$

where G_x, G_y, and G_z are the gradients applied in the x, y, and z directions, respectively. They are assumed to be fixed with respect to space and have units of Tesla per unit distance. In many cases, the gradients vary linearly with spatial coordinates x, y, and z. We'll make this assumption, and so we obtain

$$B_z(x, y, z) = G_x x + G_y y + G_z z = \int \bigtriangledown B_z \cdot d\vec{r}, \tag{2.33}$$

where $\vec{r} = (x, y, z)$.

When we apply a gradient field, the total magnetic magnetic field applied to the system of protons becomes

$$\begin{aligned} \vec{B}_{tot}(\vec{r}) &= (B_o + G_x x + G_y y + G_z z)\hat{z} \\ &= (B_o + \vec{G} \cdot \vec{r})\hat{z}, \end{aligned} \tag{2.34}$$

where $\vec{G} = G_x\hat{x} + G_y\hat{y} + G_z\hat{z}$. Consequently, the Larmor frequency of the protons becomes

$$\vec{\omega}'(\vec{r}) = \gamma\vec{B}_{tot} = (\omega_o + \gamma\vec{G} \cdot \vec{r})\hat{z} \tag{2.35}$$

Eq. (2.35) shows that, via the gradients, the frequency of precession of the protons has become spatially encoded, and so each proton has a unique frequency depending on its spatial location.

It is important to note that the equilibrium magnetization given by Eq. (2.14) remains valid for the case of a gradient field. The only difference is that now it has become spatially encoded via the gradient field, so $M_z \rightarrow M_z(\vec{r})$.

2.8.2 Time-Varying Gradient Fields

In many MR applications, we deal with time-varying linear gradient fields, i.e. $B_z(\vec{r},t)\hat{z}$, where the gradients are a function of time. Hence, our magnetic field is no longer static and we have

$$\vec{B}_{tot}(\vec{r},t) = (B_o + \vec{G}(t)\cdot\vec{r})\hat{z} \tag{2.36}$$

and

$$\vec{\omega}'(\vec{r},t) = (\omega_o + \gamma\vec{G}(t)\cdot\vec{r})\hat{z} \tag{2.37}$$

2.9 Bloch Equation in a Non-uniform Magnetic Field

In the presence of a time-varying linear gradient field, the total magnetic field applied to system of protons is given by Eq. (2.36). We apply an RF pulse to flip the equilibrium magnetization. After turning it off, the Bloch equations describing the system are

$$\begin{pmatrix} \frac{\partial M_x}{\partial t} \\ \frac{\partial M_y}{\partial t} \\ \frac{\partial M_z}{\partial t} \end{pmatrix} = \begin{pmatrix} -1/T_2 & \omega' & 0 \\ -\omega' & -1/T_2 & 0 \\ 0 & 0 & -1/T_1 \end{pmatrix} \begin{pmatrix} M_x \\ M_y \\ M_z \end{pmatrix} + \begin{pmatrix} 0 \\ 0 \\ \frac{M_o}{T_1} \end{pmatrix}$$

where ω' is the magnitude of Eq. (2.37). Hence, we have

$$\begin{aligned} \frac{dM_{xy}}{dt} &= -M_{xy}(i\omega' + \frac{1}{T_2}) \\ \frac{dM_z}{dt} &= -\frac{M_z - M_o}{T_1}, \end{aligned}$$

We can see that the application of the gradient field does not affect the longitudinal magnetization M_z, so its solution is still given by Eq. (2.24). The solution to the transverse component is

$$\begin{aligned} \frac{dM_{xy}}{M_{xy}} &= -\frac{dt}{T_2} - i(\omega_o + \gamma\vec{G}(t)\cdot\vec{r})dt \\ \int_{M_{xy}(\vec{r},t=0)}^{M_{xy}(\vec{r},t)} \frac{dM_{xy}}{M_{xy}} &= -\int_0^t \frac{dt'}{T_2} - i\omega_o\int_0^t dt' - i\gamma\int_0^t \vec{G}(t')\cdot\vec{r}dt' \\ M_{xy}(\vec{r},t) &= M_{xy}(\vec{r},0)e^{-i\omega_o t}e^{-t/T_2}e^{-i\gamma\int_0^t \vec{G}(t')\cdot\vec{r}dt'} \end{aligned} \tag{2.38}$$

The effect of the gradient field is to spatially localize the transverse magnetization.

2.10 MR Signal Equation

In MR imaging systems, the receiver coil is ideally uniformly sensitive over the entire volume of interest. It is also designed to detect flux changes in the transverse direction. Therefore, the received time signal $s_r(t)$ is derived from the contributions of all precessing transverse magnetization in the volume:

$$s_r(t) = \int_{vol} M(\vec{r}, t) dV = \int_x \int_y \int_z M(\vec{r}, t) dz\ dy\ dx \tag{2.39}$$

Substituting Eq. (2.38), we obtain

$$s_r(t) = \int_{vol} M_{xy}(\vec{r}, 0) e^{-i\omega_o t} e^{-t/T_2} e^{-i\gamma \int_0^t \vec{G}(t') \cdot \vec{r} dt'} dV \tag{2.40}$$

Since the relaxation term e^{-t/T_2} and the phase term $e^{-i\omega_o t}$ exhibit no spatial dependence, they can be viewed as multiplicative factors of $s_r(t)$, and so we can ignore them. Eq. (2.40) then becomes

$$\begin{aligned} s_r(t) &= \int_{vol} M_{xy}(\vec{r}, 0) e^{-i\gamma \int_0^t \vec{G}(t') \cdot \vec{r} dt'} dV \\ &= \int_x \int_y \int_z M_{xy}(\vec{r}, 0) e^{-i\gamma \left[\int_0^t G_x(t') dt'\right] x} e^{-i\gamma \left[\int_0^t G_y(t') dt'\right] y} e^{-i\gamma \left[\int_0^t G_z(t') dt'\right] z} dz\ dy\ dx, \end{aligned}$$

or

$$s_r(t) = \int_x \int_y \int_z M_{xy}(x,y,z) e^{-2\pi i[k_x(t)x + k_y(t)y + k_z(t)z]} dz\ dy\ dx, \tag{2.41}$$

where

$$\begin{aligned} k_x &= \frac{\gamma}{2\pi} \int_0^t G_x(t')dt' \\ k_y &= \frac{\gamma}{2\pi} \int_0^t G_y(t')dt' \\ k_z &= \frac{\gamma}{2\pi} \int_0^t G_z(t')dt' \end{aligned} \tag{2.42}$$

are the time integrals of the gradient waveforms. Note that k_x, k_y, and k_z each have units of cycles per unit distance, and so are spatial frequencies.

Lets denote the 3D Fourier transform of $M_{xy}(\vec{r})$ as

$$\tilde{M}(k_x,k_y,k_z) = \int_x \int_y \int_z M_{xy}(x,y,z) e^{-2\pi i[k_x(t)x + k_y(t)y + k_z(t)z]} dz\ dy\ dx, \tag{2.43}$$

and doing a one-to-one correspondence, we immediately see that

$$s_r(t) = \tilde{M}(k_x,k_y,k_z) \tag{2.44}$$

Thus, according to Eq. (2.41), the received time signal is simply the Fourier transform of the initial transverse magnetization (i.e. the transverse magnetization extant right

after the RF pulse has been turned off). In other words, at any given time t, $s_r(t)$ equals the value of the 3D Fourier transform $M_{xy}(x, y, z)$ at some spatial frequency $\vec{k} = (k_x, k_y, k_z)$. In the MR literature, the Fourier transform space is often called "k-space," where k represents the spatial frequency variable. k-space is simply the space in which the measured MR signal $s_r(t)$ exists while its Fourier pair is the object space. The object space is simply the space in which the volume of interest, from which the signal emanates, exists.

Eq. (2.41) forms the cornerstone of MRI. It is important to note that this Fourier relationship between the signal and object spaces would be non-existant had the spins not been spatially encoded via a gradient field. Thus, the gradient field enables imaging of the nuclear magnetization by facilitating this Fourier relationship.

In MRI, the data (signal) is always acquired in k-space. The aim then is to retrieve the object that is the source of the signal (e.g. brain), which is achieved by taking the inverse Fourier transform of the acquired k-space data. This then produces an image of the object of interest.

Chapter 3

Physics of Diffusion

Fick's laws are the governing equations of diffusion processes. These laws are purely phenomenological, as they describe the diffusive transport of matter as an empirical fact without claiming that it derives from first principles. The phenomenological approach based on Fick's laws of diffusion is one of two equivalent ways in understanding the notion of diffusion. The other is the purely atomistic approach based on random walk theory. In this chapter, we will focus on the phenomenological approach of Fick's.

After deriving the diffusion equation from Fick's laws, we solve it for homogeneous isotropic and anisotropic media. The extension to diffusion MRI is then made by solving the Bloch equation for spin diffusion. Lastly, an imaging space frequently invoked in diffusion MR experiments, termed q-space, is discussed.

3.1 Fick's Laws of Diffusion

Consider particles diffusing through some medium. Fick's first law of diffusion relates the flux of diffusing particles $\mathbf{J}(\mathbf{r}, t)$ to the concentration of particles $C(\mathbf{r}, t)$, where $\mathbf{r} = (x, y, z)$ denotes position. It postulates that a flux of particles moves from regions of high concentration to regions of low concentration. Mathematically, it is stated as

$$\mathbf{J}(\mathbf{r}, t) = -D\nabla\mathbf{C}(\mathbf{r}, t), \tag{3.1}$$

where D dentoes the diffusion coefficient and has dimensions $[D] = L^2T^{-1}$. The diffusion flux $\mathbf{J}$ is the net number of particles traversing a unit area per unit time, i.e. amount of substance per unit area per unit time, and the concentration C is the number of particles per unit volume.

Usually, in diffusion processes the number of diffusing particles is conserved. For a diffusion species which obeys a conservation law, an equation of continuity can be formulated. In the case of molecular diffusion, the equation of continuity is

$$-\nabla \cdot \mathbf{J} = \frac{\partial C}{\partial t}, \tag{3.2}$$

which states that the sum of the fluxes leaving and entering the medium is equal to the accumulation (or loss) rate, i.e. inflow - outflow = accumulation (or loss) rate.

Fick's first law Eq. (3.1) and the equation of continuity (3.2) can be combined to

give an equation which is called Fick's second law,

$$\frac{\partial}{\partial t}C(\mathbf{r},t) = \nabla \cdot (D\nabla C(\mathbf{r},t)) \tag{3.3}$$

Fick's second law is also referred to as the diffusion equation. If D depends on position, i.e. $D = D(\mathbf{r})$, the equation is non-linear and difficult to solve analytically. If the diffusivity is spatially inpedendent, which is the case for a homogeneous medium, Eq. (3.3) simplifies to

$$\frac{\partial}{\partial t}C(\mathbf{r},t) = D\nabla^2 C(\mathbf{r},t) \tag{3.4}$$

3.2 Diffusion in Isotropic Media

If a droplet of ink is injected into a container of water, the color of the ink will diffuse through the container, and eventually the water will be colored homogeneously. Such a situation is an example of isotropic diffusion, where a particle is equally likely to diffuse in any one direction, i.e. the diffusion is not biased towards a specific direction. Water, like most liquids, constitutes an isotropic medium, whose physical and chemical properties are independent of direction. In isotropic media, the diffusivity D is a scalar quantity. In this section, we will solve the diffusion equation of various dimensions for isotropic media.

3.2.1 1D Isotropic Diffusion

We want to solve the diffusion equation

$$\frac{\partial}{\partial t}C(x,t) - D\frac{\partial^2 C(x,t)}{\partial x^2} = 0, \tag{3.5}$$

subject to the initial condition $C(x,0) = \delta(x - x_o)$, which simply means that a particle is initially concentrated at position x_o. Eq. (3.5) can be solved using Fourier analysis. Denoting the Fourier transform of $C(x,t)$ as $\tilde{C}(k,t)$, we have

$$\begin{aligned} C(x,t) &= \int_{-\infty}^{\infty} \tilde{C}(k,t)e^{2\pi ikx}dk \\ \tilde{C}(k,t) &= \int_{-\infty}^{\infty} C(x,t)e^{-2\pi ikx}dx \end{aligned}$$

We will solve Eq. (3.5) in Fourier space (k-space) by taking its Fourier transform, which results in

$$\frac{\partial \tilde{C}(k,t)}{\partial t} - D(2\pi ik)^2\tilde{C}(k,t) = 0 \tag{3.6}$$

Recognizing that the above equation is a first-order linear differential equation of the form $y' = -cy$, its solution is simply

$$\tilde{C}(k,t) = A(k)e^{-4\pi^2 k^2 Dt}$$

To solve for $A(k)$, we use the intial condition imposed on the concentration:

$$\begin{aligned}\tilde{C}(k,t=0) = A(k) &= \int_{-\infty}^{\infty} C(x,t=0)e^{-2\pi ikx}dx \\ &= \int_{-\infty}^{\infty} \delta(x-x_o)e^{-2\pi ikx}dx = e^{-2\pi ikx_o}\end{aligned}$$

Hence, the Fourier transform of the concentration is $\tilde{C}(k,t) = e^{-2\pi ikx_o}e^{-4\pi^2k^2Dt}$. To derive the concentration, we compute the inverse Fourier transform of $\tilde{C}$:

$$\begin{aligned}C(x,t) &= \int_{-\infty}^{\infty} e^{-4\pi^2k^2Dt}e^{2\pi ik(x-x_o)}dk \\ = e^{-\frac{(x-x_o)^2}{4Dt}} \int_{-\infty}^{\infty} e^{-4\pi^2Dt\left(k-\frac{i(x-x_o)}{4\pi Dt}\right)^2}dk &= \frac{1}{\sqrt{4\pi Dt}}e^{-\frac{(x-x_o)^2}{4Dt}}\end{aligned} \tag{3.7}$$

The concentration $C(x,t)$, whose dimension is number of particles per unit length, can be viewed as a probability density function (pdf). Specifically, $C(x,t)$ can be interpreted as the probability density that a particle, initially located at position x_o, diffuses to position x at some time t. In other words, it's the probability density that a particle has traversed a displacement $x-x_o$ at time t. Hence, denoting the pdf as $p(x,t|x_o,t=0)$, we equivalently have

$$P(x,t|x_o,t=0) = \frac{1}{\sqrt{4\pi Dt}}e^{-\frac{(x-x_o)^2}{4Dt}} \tag{3.8}$$

Eq. (3.8) describes a Gaussian distribution of mean $\mu = x_o$ and variance $\sigma^2 = 2Dt$. The mean squared displacement (MSD) of a particle, i.e. $\langle (x - x_o)^2 \rangle$, which is equivalent to the variance of x, is simply

$$MSD = \langle (x - x_o)^2 \rangle = \mathrm{Var}(x) = 2Dt \tag{3.9}$$

3.2.2 3D Isotropic Diffusion

The 3D isotropic diffusion system can be formulated analogously to the 1D case. We now want to solve

$$\frac{\partial}{\partial t} C(\mathbf{r}, t) = D \nabla^2 C(\mathbf{r}, t), \tag{3.10}$$

subject to the initial condition $C(\mathbf{r}, t = 0) = \delta(\mathbf{r} - \mathbf{r}_o)$. The method of solution is similar to the 1D case, and so the details will not be provided here. The solution to the above equation is

$$P(\mathbf{r}, t | \mathbf{r}_o, 0) = \frac{1}{(4\pi D t)^{3/2}} e^{-\frac{(\mathbf{r}-\mathbf{r}_o)^T (\mathbf{r}-\mathbf{r}_o)}{4Dt}}, \tag{3.11}$$

where we have interpreted the concentration as a 3D pdf and $\mathbf{r} = (x, y, z)$ and $\mathbf{r}_o = (x_o, y_o, z_o)$.

The MSD can be computed similarly to the 1D case:

$$MSD = \langle (\mathbf{r} - \mathbf{r}_o)^T (\mathbf{r} - \mathbf{r}_o) \rangle$$
$$= \int_{-\infty}^{\infty} \int_{-\infty}^{\infty} \int_{-\infty}^{\infty} [(x - x_o)^2 + (y - y_o)^2 + (z - z_o)^2] p(\mathbf{r}, t|\mathbf{r}_o, 0) dx\, dy\, dz$$
$$= 6Dt \quad (3.12)$$

3.3 Diffusion in Anisotropic Media

Suppose now that we inject a droplet of ink into a homogeneous, anisotropic medium. In this case, the color of the ink will not diffuse throughout the medium to color it homogeneously. Anisotropic media exhibit different diffusion properties in different directions, and so a particle is no longer equally likely to diffuse in any one direction. Instead, the diffusion will be dominant in a specific direction. In a homogeneous, anisotropic medium, the diffusion coefficient is no longer a scalar quantity, but a rank-2 tensor $\mathbf{D}$.

3.3.1 Properties of the Diffusion Tensor

The diffusion tensor $\mathbf{D}$ is a 3 x 3 symmetric, positive definite matrix. A symmetric matrix refers to any square matrix that equals its transpose, i.e. $\mathbf{D} = \mathbf{D}^T$, and a positive definite matrix refers to any square matrix whose eigenvalues are all positive. We write the diffusion tensor as

$$\mathbf{D} = \begin{pmatrix} D_{xx} & D_{xy} & D_{xz} \\ D_{xy} & D_{yy} & D_{yz} \\ D_{xz} & D_{yz} & D_{zz} \end{pmatrix}$$

We denote the eigenvalues of $\mathbf{D}$ as λ_1, λ_2, and λ_3, which are all positive due to the positive definiteness of $\mathbf{D}$. Likewise, we denote its eigenvectors as $\vec{\epsilon}_1$, $\vec{\epsilon}_2$, and $\vec{\epsilon}_3$, where each $\vec{\epsilon}_i$ is a 3 x 1 column vector. Hence, we have

$$\mathbf{D}\vec{\epsilon}_i = \lambda_i \vec{\epsilon}_i, \qquad i = 1, 2, 3$$

A positive definite, symmetric matrix is simply a special case of a Hermitian matrix. Hermitian matrices are especially easy to handle because of two key properties they exhibit:

1. The eigenvectors corresponding to different eigenvalues of a Hermitian matrix are orthonormal. Hence, the eigenvectors of $\mathbf{D}$ satisfy $\vec{\epsilon}_i^T \vec{\epsilon}_j = \delta_{ij}, \;\; i \neq j$.

2. The eigenvectors of a Hermitian matrix span the space, i.e. any Hermitian matrix is diagonalizable. Hence, we can express the diffusion tensor as

$$\mathbf{D} = \mathbf{E}\mathbf{\Lambda}\mathbf{E}^T, \tag{3.13}$$

where $\mathbf{E} = [\vec{\epsilon}_1 \;\; \vec{\epsilon}_2 \;\; \vec{\epsilon}_3]$, $\mathbf{\Lambda} = \text{diag}(\lambda_1, \lambda_2, \lambda_3)$, and $\lambda_1 \geq \lambda_2 \geq \lambda_3$.

3.3.2 3D Anisotropic Diffusion

The diffusion equation in a homogeneous, anisotropic medium is

$$\frac{\partial}{\partial t}C(\mathbf{r},t) - \nabla \cdot (\mathbf{D}\nabla C(\mathbf{r},t)) = 0, \tag{3.14}$$

and we again impose the initial condition $C(\mathbf{r}, t = 0) = \delta(\mathbf{r}-\mathbf{r}_o)$. The probability density that a particle intially at position $\mathbf{r}_o$ moves to position $\mathbf{r}$ at time t is then

$$P(\mathbf{r}, t|\mathbf{r}_o, 0) = \frac{1}{\sqrt{|\mathbf{D}|(4\pi t)^3}} e^{-\frac{(\mathbf{r}-\mathbf{r}_o)^T \mathbf{D}^{-1}(\mathbf{r}-\mathbf{r}_o)}{4t}} \tag{3.15}$$

In the diffusion MR literature, $P(\mathbf{r}, t|\mathbf{r}_o, 0)$ is called the diffusion propagator. It is important to mention that Eq. (3.15) and (3.11) are only pertinent to Gaussian, or free diffusion, which is the type diffusion that arises in an infinite, homogeneous medium. Hence, the diffusion tensor can be viewed as an inherent descriptor of Gaussian diffusion.

Eq. (3.15) is simply a multivariate normal distribution of mean $\mu = \mathbf{r}_o$ and covariance matrix

$$\Sigma \equiv E[(\mathbf{r} - \mathbf{r}_o)(\mathbf{r} - \mathbf{r}_o)^T] \equiv \begin{pmatrix} \sigma_{xx}^2 & \sigma_{xy}^2 & \sigma_{xz}^2 \\ \sigma_{xy}^2 & \sigma_{yy}^2 & \sigma_{yz}^2 \\ \sigma_{xz}^2 & \sigma_{yz}^2 & \sigma_{zz}^2 \end{pmatrix} = 2t\mathbf{D}$$

Hence, we have $\sigma_{xx}^2 = 2tD_{xx}$, $\sigma_{xy}^2 = 2tD_{xy}$, $\sigma_{xz}^2 = 2tD_{xz}$, etc. Thus, the diffusion tensor can be viewed as a covariance matrix, whose elements represent correlations between

molecular translational displacements. Its diagonal elements D_{xx}, D_{yy}, and D_{zz}, represent the variances of the molecular displacements along the same directions x, y, and z, respectively, while its off diagonal elements D_{xy}, D_{xz}, and D_{yz} represent covariances between molecular translational displacements in orthogonal directions, i.e. between x and y, x and z, and y and z, respectively.

Eq. (3.15) simplifies to (3.11) when $\mathbf{D} = D\mathbf{I}_{3\times 3}$, and so isotropic diffusion is a special case of anisotropic diffusion where the diffusion tensor is a scaled identity matrix. Whereas isotropic diffusion is characterized by a single paramter, D, anisotropic diffusion is characterized by 6 independent parameters (D_{xx}, D_{yy}, D_{zz}, D_{xy}, D_{xz}, and D_{yz}). Physically, this is because the structure of an anisotropic medium biases the translational displacements of molecules along paritcular directions and away from others.

The MSD of a molecule diffusing in a homogeneous, anisotropic medium is then

$$\begin{aligned} MSD &= \langle(\mathbf{r}-\mathbf{r}_o)^T(\mathbf{r}-\mathbf{r}_o)\rangle = E[(x-x_o)^2] + E[(y-y_o)^2] + E[(z-z_o)^2] \\ &= \sigma_{xx}^2 + \sigma_{yy}^2 + \sigma_{zz}^2 = 2t(D_{xx}+D_{yy}+D_{zz}) \\ &= \mathrm{Tr}(\Sigma), \end{aligned} \tag{3.16}$$

where Tr denotes trace.

3.4 Bloch-Torrey Equation

The Bloch-Torrey equation [69] is a generalization of the phenomenological Bloch equation, with added terms to incorporate the effects of the diffusion of magnetization.

The diffusion of magnetization, or equivalently spin diffusion, refers to the self-diffusion of the molecules containing the nuclear spins (e.g. water, which is composed of 2 ^{1}H nuclei), and arises under conditions of inhomogeneity in the magnetic field (note that the application of a gradient field makes the main magnetic field inhomogeneous).

Torrey, in his analysis, assumed the diffusion to be Gaussian [69], and hence described by the diffusion tensor in Eq. (3.15). The Bloch-Torrey equation, expressed in terms of the transverse magnetization component M_{xy}, is written as

$$\frac{\partial M_{xy}}{\partial t} = -i\omega_o M_{xy} - i\gamma(\mathbf{r}\cdot\mathbf{G})M_{xy} - M_{xy}/T_2 + \bigtriangledown^T \mathbf{D} \bigtriangledown M_{xy}, \tag{3.17}$$

where $M_{xy} = M_x + iM_y$, $\mathbf{r} = [x \;\; y \;\; z]^T$, $\mathbf{G} = [G_x \;\; G_y \;\; G_z]^T$, $\bigtriangledown = [\partial/\partial x \;\; \partial/\partial y \;\; \partial/\partial z]^T$, and $\mathbf{D}$ is the diffusion tensor. In order to solve the above partial differential equation for M_{xy}, we employ an ansatz solution of the form

$$M_{xy}(\mathbf{r},t) = A(t)e^{-i\omega_o t}e^{-t/T_2}e^{-i\gamma\mathbf{r}\cdot\int_0^t \mathbf{G}(t')dt'}, \tag{3.18}$$

where $A(t)$ represents the signal component arising due to molecular diffusion. Substituting Eq. (3.18) into (3.17), we obtain a formula for $A(t)$:

$$\begin{aligned} A(t) &= A(0)e^{-\gamma^2\int_0^t\left[\left(\int_0^{t'}\mathbf{G}(t'')dt''\right)^T\mathbf{D}\left(\int_0^{t'}\mathbf{G}(t'')dt''\right)\right]dt'} \\ &= A(0)e^{-\int_0^t \mathrm{Tr}(\mathbf{b}(t')\mathbf{D})dt'} \end{aligned} \tag{3.19}$$

where $\mathbf{b} = \mathbf{L}\mathbf{L}^T$ and $L(t') = \gamma \int_0^{t'} \mathbf{G}(t'')dt''$. The 3 x 3 matrix $\mathbf{b}$ is called the **b**-matrix. Note that $\mathrm{Tr}(\mathbf{b}(t)\mathbf{D})$ can also be written as $\mathbf{b} : \mathbf{D}$ (generalized dot product). Thus, we have

$$M_{xy}(\mathbf{r}, t) = A(0)e^{-\int_0^t \mathrm{Tr}(\mathbf{b}(t')\mathbf{D})dt'} e^{-i\gamma\mathbf{r}\cdot\int_0^t \mathbf{G}(t')dt'} e^{-i\omega_o t} e^{-t/T_2}$$

Since we are only concerned with the effect of molecular diffusion on the signal, we can ignore the terms related to spin phase, Larmor precession, and T_2 relaxation and focus exclusively on $A(t)$.

3.5 Pulsed Gradient Spin Echo Method for Diffusion Measurement

Eq. (3.19) can be further simplified if a pulsed gradient spin echo (PGSE) [68] sequence, illustrated in Fig. 3.1, is used to measure the diffusion. The PGSE sequence was pioneered by Stejskal and Tanner and is by far the most widely used approach for measuring diffusion in MRI. The general idea of the PGSE sequence is to excite the spin system with a $\pi/2$-RF pulse, spatially encode the spin system with a magnetic field gradient of duration δ, invert the spin phase with a π-RF pulse, apply a second field gradient with equal intensity and duration to the previous gradient and at a time Δ after the first gradient, and then acquire the echo[1] at time TE.

In the PGSE sequence, the gradient $\mathbf{G}$ assumes the simple form

[1]The acquired signal is often called "echo."

$$\mathbf{G}(t) = G(t)\mathbf{g},$$

where G is the magnitude of the gradient vector and $\mathbf{g} = [g_x \quad g_y \quad g_z]^T$ is a time-independent unit vector. Specifically,

$$G(t) = H(t_1) - H(t_1 - \delta) + H(t_2) - H(t_2 - \delta),$$

where $t_2 = t_1 + \Delta$ (refer to Fig. 3.1) and the symbol H denotes the Heaviside function. It is convenient to define a measure termed the b-value as

$$b = \int_0^{\mathrm{TE}} \mathbf{L}(t') \cdot \mathbf{L}(t') dt' \tag{3.20}$$

The b-value is a measure of the degree of diffusion-weighting generated by the diffusion gradient $\mathbf{G}$, and for a PGSE sequence, it assumes the form

$$b = (\gamma G \delta)^2 (\Delta - \delta/3) \tag{3.21}$$

The $\mathbf{b}$-matrix for a PGSE experiment becomes

$$\mathbf{b} = b\mathbf{g}\mathbf{g}^T = \begin{pmatrix} bg_x^2 & bg_x g_y & bg_x g_z \\ bg_x g_y & bg_y^2 & bg_y g_z \\ bg_x g_z & bg_y g_z & bg_z^2 \end{pmatrix}$$

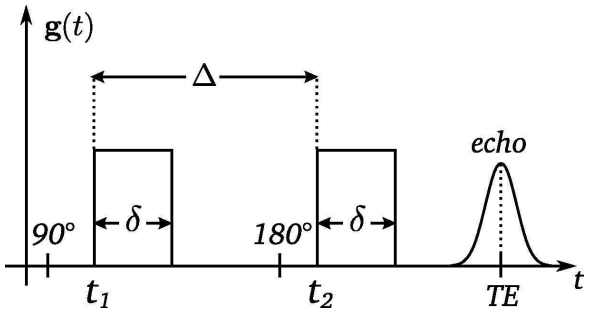

Figure 3.1: Pulsed gradient spin echo (PGSE) sequence proposed by [68]. Adapted from [14].

Consequently, the generalized dot product between **b** and **D** reduces down to a quadratic form:

$$\mathbf{b} : \mathbf{D} = b\mathbf{g}^T\mathbf{D}\mathbf{g}$$

Hence, Eq. (3.19), for a PGSE sequence, becomes

$$A(\mathrm{TE}) = A(0)e^{-b\mathbf{g}^T\mathbf{D}\mathbf{g}},$$

which is the famous Stejskal-Tanner relation [68]. For the case of isotropic diffusion, where $\mathbf{D} = D\mathbf{I}_{3\times 3}$, the above relation simplies to

$$A(\mathrm{TE}) = A(0)e^{-bD},$$

The Stejskal-Tanner formula is more commonly written as

$$S = S_o e^{-b\mathbf{g}^T\mathbf{D}\mathbf{g}}, \tag{3.22}$$

where $S = A(\mathrm{TE})$ denotes the measured diffusion-weighted signal and $S_o = A(0)$ the measured signal in the absence of a field gradient (i.e. $b = 0$). Eq. (3.22) establishes that the diffusion signal attenuates with respect to the b-value. It is important to emphasize that Eq. (3.22) is only valid for Gaussian diffusion, and this fact will be explored more thoroughly in the next section.

3.6 Q-Space Formalism

Lets introduce the wave-vector $\mathbf{q}$, which is defined as

$$\mathbf{q}(t) = \frac{\gamma}{2\pi}\int_0^t \mathbf{G}(t')dt' \tag{3.23}$$

Just like the $\mathbf{k}$ wave-vector of k-space, $\mathbf{q}$ is a spatial frequency. In addition, we will make two assumptions regarding the PGSE experiment:

1. The duration of the diffusion gradient pulse, δ, is considered to be infinitesimally short, i.e. $\delta \to 0$.

2. Molecular displacements taking place during the application of the gradient pulses are assumed to be negligible compared to the displacements happening during time Δ, i.e. $\delta \ll \Delta$.

These two assumptions are collectively termed the narrow pulse approximation (NPA) [23, 34]. As a result of Assumption 1, the field gradient becomes independent of time, i.e. $G(t) \rightarrow G$, thereby also making the wave-vector $\mathbf{q}$ time-independent:

$$\mathbf{q} = \frac{\gamma}{2\pi} \int_0^\delta \mathbf{G} dt = \frac{1}{2\pi} \gamma \delta \mathbf{G} \tag{3.24}$$

Using Eq. (3.24), we can express the b-value, given by Eq. (3.21), in terms of q:

$$b(q) = 4\pi^2 \tau_d q^2, \tag{3.25}$$

where $\tau_d = \Delta - \delta/3$ and is called the diffusion time. Thus, each b-value corresponds to a unique value in q-space.

Consider a spin (e.g. water molecule) inhabiting some volume of interest, i.e. a voxel. In the NPA regime, the relationship between the q-space signal attenuation $E(\mathbf{q})$ and the diffusion propagator $P(\mathbf{r}, \tau_d | \mathbf{r}_o, 0)$ becomes greatly simplified and is given by [23, 34]

$$E(\mathbf{q}) = \int \int P(\mathbf{r}, \tau_d | \mathbf{r}_o, 0) P(\mathbf{r}_o) e^{2\pi i \mathbf{q} \cdot (\mathbf{r} - \mathbf{r}_o)} d^3\mathbf{r} d^3\mathbf{r}_o, \tag{3.26}$$

where $P(\mathbf{r}, \tau_d | \mathbf{r}_o, 0)$ is the probability density that a spin at position $\mathbf{r}_o$ at time $t = 0$ ends up at position $\mathbf{r}$ at time τ_d; $P(\mathbf{r}_o)$ is the likelihood of finding a spin at position $\mathbf{r}_o$ at $t = 0$, and is assumed to be constant in the voxel. Let $\mathbf{p}$ denote the displacement vector

$\mathbf{p} = \mathbf{r} - \mathbf{r}_o$. The ensemble average propagator (EAP) is then defined as

$$P(\mathbf{p}) = \int P(\mathbf{r}, \tau_d | \mathbf{r}_o, 0) P(\mathbf{r}_o) d^3\mathbf{r}_o = \int P(\mathbf{p} + \mathbf{r}_o, \tau_d | \mathbf{r}_o, 0) P(\mathbf{r}_o) d^3\mathbf{r}_o, \tag{3.27}$$

and indicates the ensemble average likelihood for a water molecule residing in the voxel to undergo a net displacement $\mathbf{p}$ during the diffusion time τ_d. It is apparent from Eq. (3.27) that the EAP is an average of the diffusion propagator $P(\mathbf{r}, \tau_d | \mathbf{r}_o, 0)$ across all possible inital positions $\mathbf{r}_o$. The diffusion signal $E(\mathbf{q})$ is then related to the EAP by the following relationship [17, 23, 34]:

$$E(\mathbf{q}) = \int P(\mathbf{p}) e^{2\pi i \mathbf{q}\cdot\mathbf{p}} d^3\mathbf{p} \tag{3.28}$$

Eq. (3.28) is the 3D inverse Fourier transform of the EAP with respect to the displacement vector $\mathbf{p}$. The 3D Fourier transform of $E(\mathbf{q})$ yields $P(\mathbf{p})$:

$$P(\mathbf{p}) = \int E(\mathbf{q}) e^{-2\pi i \mathbf{q}\cdot\mathbf{p}} d^3\mathbf{q} \tag{3.29}$$

Hence, the diffusion signal acquired in q-space and the EAP are Fourier transform pairs in the NPA regime.

The Fourier relationship between the q-space signal and EAP is only valid in the NPA regime. The NPA assumptions, however, often do not hold for q-space diffusion MR experiments performed using conventional clinical MR systems. The gradient duration is rarely negligibly small, especially so at high b-values, and it is often comparable to the

diffusion time (i.e. $\delta \sim \Delta$). Several studies [15, 53, 75] have shown that even when the NPA assumptions do not hold, the Fourier relationship in Eq. (3.28) is still valid, and correct microstructural information can still be obtained. The diffusion displacements, however, will be consistently underestimated [75].

3.6.1 Gaussian Diffusion and the Insights Revealed by q-Space

In deriving the solution to the Bloch-Torrey equation for a PGSE sequence, given by Eq. (3.22), we assumed the diffusion was Gaussian and hence could be characterized by a rank-2 tensor. However, we have't directly shown that Eq. (3.22) is only valid for Gaussian diffusion. In other words, we have not formally established that the diffusion propagator is a Gaussian pdf. Using the q-space formalism, we can show that Eq. (3.15) and (3.22) are intimately linked.

In Sec. 3.5, we showed that the solution to the Bloch-Torrey equation for a PGSE sequence is given by Eq. (3.22), which we display again:

$$E(b) = \frac{S(b)}{S_o} = e^{-\gamma^2 \delta^2 G^2 \tau_d \mathbf{g}^T \mathbf{D} \mathbf{g}},$$

Using Eq. (3.25), we can express (3.22) as a function of q:

$$E(\mathbf{q}) = e^{-4\pi^2 \tau_d q^2 \mathbf{g}^T \mathbf{D} \mathbf{g}} = e^{-4\pi^2 \tau_d \mathbf{q}^T \mathbf{D} \mathbf{q}} \tag{3.30}$$

Eq. (3.30) is simply a multivariate Gaussian function. Taking its Fourier transform, we

obtain the EAP:

$$P(\mathbf{p}) = \int e^{-4\pi^2\tau_d \mathbf{q}^T\mathbf{D}\mathbf{q}} e^{-2\pi i \mathbf{q}\cdot\mathbf{p}} d^3\mathbf{q} = \frac{1}{\sqrt{|\mathbf{D}|(4\pi\tau_d)^3}} e^{-\frac{\mathbf{p}^T\mathbf{D}^{-1}\mathbf{p}}{4\tau_d}} \tag{3.31}$$

Eq. (3.31) is simply the Gaussian propagator encountered in Eq. (3.15). Thus, the q-space formalism directly links Eq. (3.22) to Gaussian diffusion.

*****

An alternative perspective on Gaussian diffusion can be obtained by studying $E(\mathbf{q})$ in the small-q (or low b) limit [17]. For very small q, Eq. (3.30) becomes

$$E(\mathbf{q}) \approx 1 - 4\pi^2\tau_d \mathbf{q}^T\mathbf{D}\mathbf{q}, \quad \text{(Gaussian signal decay in long-wavelength limit)} \tag{3.32}$$

Now, the expected value of $e^{-2\pi i \mathbf{q}\cdot\mathbf{p}}$ is given by $E(\mathbf{q})$, indicating that $E(\mathbf{q})$ is the characteristic function of the EAP:

$$E(\mathbf{q}) = \langle e^{-2\pi i \mathbf{q}\cdot\mathbf{p}} \rangle = \int P(\mathbf{p}) e^{2\pi i \mathbf{q}\cdot\mathbf{p}} d^3\mathbf{p}$$

Taylor expanding $e^{-2\pi i \mathbf{q}\cdot\mathbf{p}}$ so to express $E(\mathbf{q})$ in terms of the moments of the EAP, we have in the small-q regime[2]

$$E(\mathbf{q}) \approx 1 - \frac{(2\pi)^2}{2!}\mathbf{q}^T\langle \mathbf{p}\mathbf{p}^T\rangle \mathbf{q} + O(q^4)$$

The term $\langle \mathbf{p}\mathbf{p}^T\rangle$ is simply the covariance matrix of the EAP.

If the diffusion is Gaussian, than $\langle \mathbf{p}\mathbf{p}^T\rangle = 2\tau_d\mathbf{D}$ and we obtain

$$E(\mathbf{q}) = 1 - 4\pi^2\tau_d\mathbf{q}^T\mathbf{D}\mathbf{q} + O(q^4) \tag{3.33}$$

Clearly, to second order in q, one cannot distinguish the decay of $E(\mathbf{q})$ in Eq. (3.33) to that of Eq. (3.32). Therefore, in the small-q regime, the quadratic decay of $E(\mathbf{q})$ vs. q can be viewed as arising from a Gaussian displacement distribution. In other words, Gaussian diffusion is a low q-value (or low b-value) phenomenon.

3.6.2 Concluding Remarks on Q-Space

The q-space framework is a powerful, alternative means to studying diffusion because it produces a simple, Fourier relationship between the acquired diffusion signal and EAP. It thereby facilitates EAP imaging within diffusion MRI, which will be explored in great detail later in this work. Significantly, unlike the diffusion tensor which

[2]The EAP and diffusion signal are assumed to be even functions. Thus, the odd moments of the EAP are zero since the integral of the product of an odd and even function is always zero.

is intrinsically linked to Gaussian diffusion, the q-space formalism enables one to characterize the diffusion without a prior Gaussian assumption. In other words, the EAP is a natural mathematical descriptor of diffusion, unlike the diffusion tensor, because it does not require a specific mode of diffusion behavior.

3.7 Diffusion in Biological Tissue

Eq. (3.15) and (3.16) describe free diffusion, i.e. Gaussian diffusion, and so pertain only to an infinite, homogeneous medium. Biological tissues, however, differ largely from the condition of an "infinite, homogeneous medium." They are heterogeneous, containing multiple subcompartments. Exchange and transport between subcompartments may have to be considered, depending on the permeability of the barriers that divide them. White matter, specifically, is quite heterogeneous. Axons are ordered in fascicles and are surrounded by a complex extra-axonal environment composed of astrocytes, glia, and extracellular matrix molecules. In such a heterogeneous environment, the assumption of free diffusion is no longer sound and so the diffusion tensor becomes meaningless. In this section, we will explore several elementary diffusion processes in biological tissues that significantly deviate from the ideal Gaussian case.

3.7.1 Restricted Diffusion

Diffusion is restricted when boundaries in the medium impede the molecules from moving freely [50]. In white matter, it chiefly arises within the axonal space [5, 9]. Restricted diffusion effects depend on the shape of the restricting volumes (spherical,

cylindrical, planar walls) and the type of MRI experiment (constant or pulsed gradients), and so there is no unique analytical expression that could describe any configuration. However, an adequate understanding of restricted diffusion can be attained through its relation to the diffusion time. For simplicity, consider the case of water molecules residing within an axon of diameter d, as illustrated in Fig. 3.2. When the diffusion time τ_d is very short, most molecules do not have enough time to reach the axonal walls, and so they behave as though they were diffusing freely. As the diffusion time increases (and so the likelihood of a molecule striking a boundary), a larger fraction of molecules will strike the axonal walls, and their displacement distribution will consequently deviate from Gaussian behavior. Recall from Eq. (3.25) that longer diffusion times correspond to higher b-values, implying then that restricted diffusion is a high b-value phenomenon, which will be explored in greater depth in the next chapter.

One way to distinguish between ideal Gaussian diffusion and restricted diffusion is to plot $\sqrt{\text{MSD}}$ against $\sqrt{\tau_d}$, as shown in Fig. 3.3. For free diffusion there is a linear relation between the mean squared displacement and the diffusion time, as indicated by Eq. (3.16), with the trace of the diffusion tensor forming the slope. Considering the 1D case, the root mean squared displacement is given by the square root of Eq. (3.9):

$$\sqrt{\langle (x - x_o)^2 \rangle} = \sqrt{2D\tau_d}$$

In restricted diffusion, the root mean squared displacement deviates from linearity with respect to $\sqrt{\tau_d}$. Initially, at very short τ_d, which corresponds to $\sqrt{\text{MSD}} \ll d$, the plot is linear, indicating that restricted diffusion is nearly indistinguishable from free diffusion at low b-values. As $\sqrt{\text{MSD}} \to d$, the plot begins to curve, and it finally plateaus when $\sqrt{\text{MSD}}$ reaches the dimension of the restricting compartment - in the case of the axon of

diameter d, $\sqrt{\text{MSD}}$ levels off at d. Such non-linear behavior demonstrates that restricted diffusion is a non-Gaussian process.

3.7.2 Hindered Diffusion

To illustrate restricted diffusion, we considered the case of intra-axonal (i.e. situated within an axon) water molecules, where the main obstacle impeding free diffusion was the axonal wall. Lets now consider extra-axonal water molecules. Outside the axon, one finds various structures such as fibers, macromolecules, organelles, etc. The presence of such obstacles means that water molecules must travel longer paths to cover any given distance. In other words, molecules can no longer diffuse in a straight line between two locations, but must diffuse around structures that are impermeable to them. This phenomenon is referred to as tortuosity. Consequently, a longer diffusion time is needed to diffuse between the two locations. Such obstruction of the diffusion in the extra-axonal space is called hindered diffusion [9, 50], and is illustrated in Fig. 3.2.

Tortuosity is key feature of hindered diffusion. Classically, the tortuosity effect is expressed quantitatively using a tortuosity coefficient, λ, such that

$$D_{app} = \frac{D_o}{\lambda^2}, \tag{3.34}$$

where D_o is the diffusion coefficient observed in the absence of obstacles and D_{app} is the diffusion coefficient measured in the presence of obstacles. Note that $\lambda^2 \geq 1$. Eq. (3.34) shows that hindered diffusion results in a decrease in the diffusion coefficient, which will be explained in the next paragraph.

The intra-axonal space can be viewed as finite, with the axonal walls forming the demarcating barrier. The extra-axonal space, however, can be viewed as an infinite space peppered with various obstacles, having no real demarcation. For this reason, molecules can in principal diffuse over very large distances in hindered diffusion, as opposed to restricted diffusion. Thus, there will be no plateau in the plot of $\sqrt{\text{MSD}}$ vs. $\sqrt{\tau_d}$ for hindered diffusion. In fact, such a plot will be linear for hindered diffusion, except the slope (diffusion coefficient) will be less than the free diffusion case. The decrease in diffusivity in hindered diffusion is due to the longer diffusion time needed for a water molecule to go from point A to B, which is tantamount to the MSD increasing less with the diffusion time (refer to Fig. 3.2). At very short diffusion times (i.e. low b-values), however, hindered diffusion will be nearly indistinguishable from free diffusion.

Restricted and hindered diffusion have different effects on a water molecule's ability to diffuse. In restricted diffusion, once a water molecule strikes the axonal wall, its diffusion becomes restricted by the barrier and so it will minimally diffuse as a result. In hindered diffusion, however, a water molecule can diffuse from one location to another, but the rate at which it diffuses is reduced by the presence of various obstacles in the extra-axonal space.

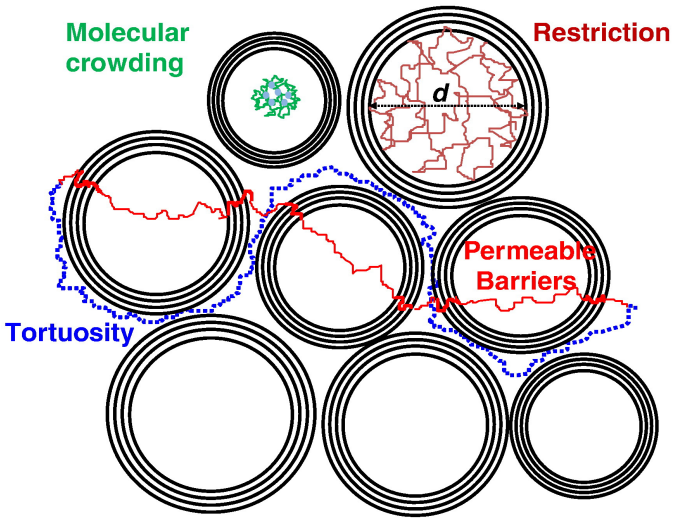

Figure 3.2: Restricted and hindered diffusion in white matter. Restricted diffusion is shown here arising within an axon of diameter d. Hindered diffusion occurs in the extra-axonal environment. Outside the axon, one finds various structures such as fibers and macromolecules. In going from A to B then, water molecules will have to move around the fibers, resulting in a tortuous trajectory instead of a straight line. Consequently, a longer diffusion time is needed to diffuse between A and B, which is tantamount to the MSD increasing less with the diffusion time. Adapted from [50].

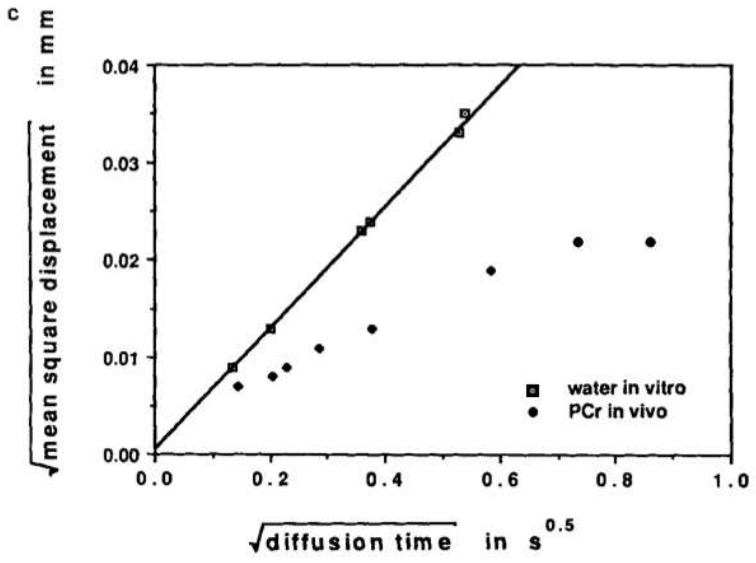

Figure 3.3: Free (Gaussian) and restricted diffusion vs. diffusion time. The root MSD is plotted against the square root of the diffusion time for water *in vitro* (no restricting boundaries) and for phosphocreatine *in vivo* in rat muscle. A line is also plotted using Eq. (3.9) for pure water, fitting the *in vitro* water data very well, as is expected for Gaussian diffusion. The phosphocreatine curve is initially linear but eventually levels off, suggesting that the diffusion of phosphocreatine in muscle cell is restricted. The size of this restricting volume can be roughly estimated to be 0.02 mm. Adapted from [55].

Chapter 4

Diffusion Magnetic Resonance Imaging

Diffusion magnetic resonance imaging (dMRI) is an MRI modality that allows for the *in vivo* and non-invasive mapping of water diffusion in biological tissues. Water molecules are in constant thermal motion, but this motion is constrained by the presence of surrounding structures, such as fibers, membranes, and surrounding tissue. Water diffusion patterns can therefore reveal microstructural properties of the underlying tissue, either normal or in a diseased state.

In Chapters 1 and 2, we discussed the underlying physics behind MRI and diffusion, respectively. In this chapter, we will bring everything together by discussing the imaging applications of the union between MRI and diffusion, i.e. dMRI. Specifically, we will explore several important dMRI methods.

4.1 Diffusion Tensor Imaging

Orgnaic tissues, such as the neural axons of white matter in the brain and muscle fibers in the heart, have internal fibrous structures similar to the anisotropy of some crystals. Hence, the diffusion of water in such tissues will be anisotropic. In 1994, Basser et al. [18] proposed to use the diffusion tensor, encountered in chapter 2, to map *in vivo* (via MR principles) diffusion anisotropy in biological tissues. This diffusion tensor imaging (DTI) approach has become the most widely used form of dMRI.

The underlying assumption of DTI is that diffusion in biological tissues is Gaussian, which is sound at low b-values. The diffusion signal attenuation and EAP within the DTI framework are given by Eq. (3.22) and (3.31), respectively, which we display again:

$$S(b) = S_o e^{-b\mathbf{g}^T\mathbf{D}\mathbf{g}} \quad \text{(DTI signal attenuation)}$$
$$P(\mathbf{p}) = \frac{1}{\sqrt{|\mathbf{D}|(4\pi\tau_d)^3}} e^{-\frac{\mathbf{p}^T\mathbf{D}^{-1}\mathbf{p}}{4\tau_d}} \quad \text{(DTI EAP)}$$

4.1.1 Diffusion Tensor Reconstruction

As mentioned in Chapter 2, the diffusion tensor is a symmetric rank 2 tensor, and therefore has 6 unique coefficients. The simplicity and elegance of DTI lies in the fact that a minimum of seven parameters is needed to model complex anatomical information: six to obtain the six unique tensor elements and one to obtain to estimate the $b = 0$ signal magnitude S_o. Hence, the diffusion-weighted signal S needs to be measured at

a minimum of seven unique gradient directions (one $b = 0$ and six diffusion-weighted) in order to not have an under-determined system. DTI is typically a single b-value technique, with the diffusion-weighted images acquired at $b \sim 1000$ s/mm^2.

Taking the natural logarithm of Eq. (3.22), we obtain

$$\ln(S) = \ln(S_o) - b(g_x^2 D_{xx} + g_y^2 D_{yy} + g_z^2 D_{zz} + 2g_x g_y D_{xy} + 2g_x g_z D_{xz} + 2g_y g_z D_{yz})$$

Now consider we have N total signal measurements, including both diffusion-weighted and $b = 0$ measurements, and denoted by the $N \times 1$ vector $\mathbf{y}$:

$$\mathbf{y} = [\ln(S_1) \;\; \ln(S_2) \;\; \cdots \;\; \ln(S_N)]^T$$

Then the $N \times 7$ design matrix is

$$\mathbf{A} = \begin{pmatrix} 1 & -bg_{x1}^2 & -bg_{y1}^2 & -bg_{z1}^2 & -2bg_{x1}g_{y1} & -2bg_{x1}g_{z1} & -2bg_{y1}g_{z1} \\ 1 & -bg_{x2}^2 & -bg_{y2}^2 & -bg_{z2}^2 & -2bg_{x2}g_{y2} & -2bg_{x2}g_{z2} & -2bg_{y2}g_{z2} \\ \vdots & \vdots & \vdots & \vdots & \vdots & \vdots & \vdots \\ 1 & -bg_{xN}^2 & -bg_{yN}^2 & -bg_{zN}^2 & -2bg_{xN}g_{yN} & -2bg_{xN}g_{zN} & -2bg_{yN}g_{zN} \end{pmatrix}$$

The 7×1 vector of unknown DTI parameters is

$$\mathbf{x} = [\ln(S_o) \;\; D_{xx} \;\; D_{yy} \;\; D_{zz} \;\; D_{xy} \;\; D_{xz} \;\; D_{yz}]^T$$

Thus, we have a linear model of the form $\mathbf{y} = \mathbf{Ax}$. This system of over-determined equations can be solved easily with linear least squares (LLS), which yields the vector of LLS estimated DTI parameters $\tilde{\mathbf{x}}$

$$\tilde{\mathbf{x}} = (\mathbf{A}^T\mathbf{A})^{-1}\mathbf{A}^T\mathbf{y} \tag{4.1}$$

4.1.2 Visualization of the Diffusion Tensor

An ellipsoid is the 3D analogue of the 2D ellipse and is defined as

$$\mathbf{p}^T\mathbf{Op} = 1,$$

where $\mathbf{p} = [x \;\; y \;\; z]^T$ and $\mathbf{O}$ is a 3 x 3 symmetric, positive definite matrix (e.g. diffusion tensor) with entries

$$\mathbf{O} = \begin{pmatrix} a & b & c \\ b & d & e \\ c & e & f \end{pmatrix}$$

In standard form then, the equation defining an ellipsoid can be written as

$$ax^2 + 2bxy + dy^2 + 2cxz + 2eyz + fz^2 = 1 \tag{4.2}$$

Now lets construct a surface of constant probability (i.e. isoprobability surface) by setting the exponent of the DTI EAP to a constant:

$$\frac{\mathbf{p}^T\mathbf{D}^{-1}\mathbf{p}}{4\tau_d} = k$$

Suppose $k = 1/4$

$$\mathbf{p}^T\mathbf{D}^{-1}\mathbf{p} = \tau_d$$

$$(D_{yy}D_{zz} - D_{yz}^2)x^2 + 2(D_{xz}D_{yz} - D_{xy}D_{zz})xy + (D_{xx}D_{zz} - D_{xz}^2)y^2 + 2(D_{xy}D_{yz} - D_{xz}D_{yy})xz$$
$$+ 2(D_{xy}D_{xz} - D_{xx}D_{yz})yz + (D_{xx}D_{yy} - D_{xy}^2)z^2 = |\mathbf{D}|\tau_d, \tag{4.3}$$

which is the equation of an ellipsoid. Hence, the isoprobability surface for Gaussian diffusion is an ellipsoid, or in other words, the EAP within the DTI framework can be visualized as a diffusion ellipsoid[1].

For the case of isotropic diffusion, where $\mathbf{D} = D\mathbf{I}_{3\times 3}$, Eq. (4.3) becomes

$$x^2 + y^2 + z^2 = (\sqrt{D\tau_d})^2, \tag{4.4}$$

which is the equation of a sphere. A sphere is simply an ellipsoid of zero eccentricity.

*****

[1]Any multivariate normal distribution can be visualized as an ellipsoid since its covariance matrix is symmetric, positive definite.

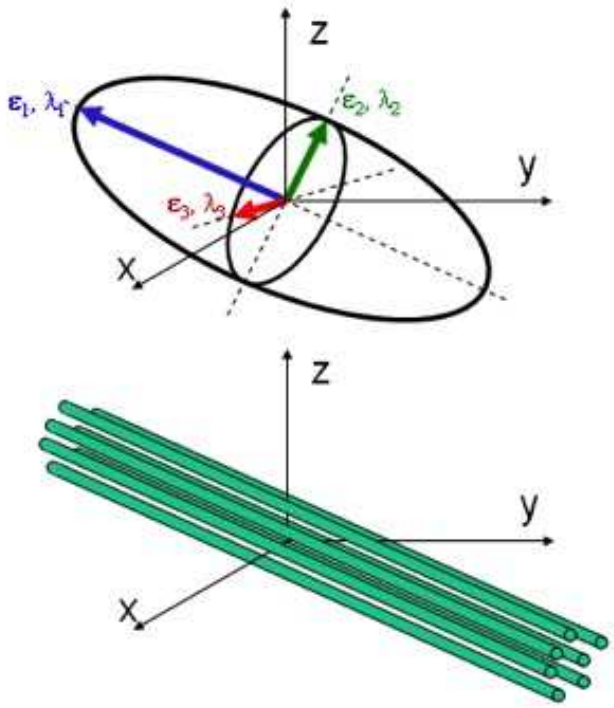

Figure 4.1: Any symmetric, positive definite matrix (e.g. diffusion tensor) can be visualized as an ellipsoid. Here, the diffusion ellipsoid for a single fiber bundle is shown in the principal frame, where the diffusion tensor's eigenvectors coincide with the semi-principal axes of the ellipsoid. The principal eigenvector $\vec{\epsilon}_1$, corresponding to the tensor's largest eigenvalue, λ_1, is coincident with the fiber orientation. Thus, the diffusion is most prominent parallel to the fiber tract. The length of each of the ellipsoid's semi-principal axes is related to the corresponding eigenvalue - the longest axis to λ_1 and etc. Adapted from [3].

Eq. (4.3) is in the lab frame of reference (i.e. the reference frame where the components of $\mathbf{D}$ are measured), where the molecular translational displacements are correlated (i.e. D_{xy}, D_{xz}, and D_{yz} are all non-zero). However, we can always find a frame of reference where these translational displacements appear to be uncorrelated (i.e. $D_{xy} = D_{xz} = D_{yz} = 0$). Such a frame is called the "principal", or "fiber" frame (i.e. the reference frame from the perspective of the fiber), and is denoted by the coordinates $\mathbf{p}' = [x' \;\; y' \;\; z']^T$.

Now recall from Sec. 3.3.1 that the diffusion tensor is diagonalizable:

$$\mathbf{D} = \mathbf{E}\mathbf{\Lambda}\mathbf{E}^T,$$

where $\mathbf{E} = [\vec{\epsilon}_1 \;\; \vec{\epsilon}_2 \;\; \vec{\epsilon}_3]$ and $\mathbf{\Lambda} = \text{diag}(\lambda_1, \lambda_2, \lambda_3)$. ϵ_i and λ_i are the eigenvectors and eigenvalues of $\mathbf{D}$, respectively. The lab frame coordinates can be transformed to the principal frame via the transformation

$$\mathbf{p}' = \mathbf{E}^T\mathbf{p} \tag{4.5}$$

Using this relationship, it can then be shown that

$$\mathbf{p}^T\mathbf{D}^{-1}\mathbf{p} = \mathbf{p}'^T\mathbf{\Lambda}^{-1}\mathbf{p}', \tag{4.6}$$

which indicates that the diffusion tensor in the principal frame is Λ. The diffusion ellipsoid in the principal frame is then

$$\frac{\mathbf{p}'^T \mathbf{\Lambda}^{-1} \mathbf{p}'}{4\tau_d} = k$$

$$\text{Suppose } k = 1/2$$

$$\mathbf{p}'^T \mathbf{\Lambda}^{-1} \mathbf{p}' = 2\tau_d$$

$$\left(\frac{x'}{\sqrt{2\lambda_1\tau_d}}\right)^2 + \left(\frac{y'}{\sqrt{2\lambda_2\tau_d}}\right)^2 + \left(\frac{z'}{\sqrt{2\lambda_3\tau_d}}\right)^2 = 1 \tag{4.7}$$

In the principal reference frame, then, the diffusion tensor's eigenvectors coincide with the semi-principal axes of the ellipsoid. The length of each of the ellipsoid's semi-principal axes is given by the root mean squared displacement at time τ_d along the corresponding eigenvector. Fig. 4.1 illustrates a diffusion ellipsoid in the principal frame.

Now recall from Sec. 3.3.1 that the diffusion tensor is a Hermitian matrix, which means that its eigenvalues obey

$$\lambda_1 \geq \lambda_2 \geq \lambda_3$$

In an isotropic medium (e.g. cerebrospinal fluid), all the eigenvalues are equal, and so the ellipsoid becomes a sphere. In a homogeneous anisotropic medium (e.g. white matter regions composed solely of single fibers such as genu and splenium of corpus callosum),

$$\lambda_1 > \lambda_2 \geq \lambda_3$$

In an (homogeneous) anisotropic medium then, λ_1 is the tensor's largest eigenvalue, and hence corresponds to the ellipsoid's longest semi-principal axis in the fiber frame. Its

corresponding eigenvector, $\vec{\epsilon}_1$, is often termed the prinical eigenvector because it indicates the principal direction of diffusion, i.e. the direction at which the diffusion is most biased in an anisotropic medium. In the fiber frame, $\vec{\epsilon}_1$ coincides with the fiber orientation (i.e. the direction at which the fiber is pointing), and so the diffusion is most prominent parallel to the fiber tract. The diffusion is less prominent in directions perpendicular to the fiber tract, which are denoted by the eigenvectors $\vec{\epsilon}_2$ and $\vec{\epsilon}_3$. Therefore, if we consider the example of a single white matter fiber, the diffusion ellipsoid depicts both the fiber orientation (and thereby the direction at which the water diffusion is most biased) via $\vec{\epsilon_1}$, and the mean squared displacement of a water molecule along directions parallel and perpendicular to the fiber tract via the eigenvalues.

4.1.3 Scalar Invariants

There are various rotationally invariant scalar features of the diffusion tensor (i.e. the eigenvalues[2] or some combination of them) that can be obtained, and which summarize the diffusion information at each voxel. Such measures are invariant with respect to rotation of the coordinate system, and so are independent of fiber direction (i.e. they have the same value whether measured in the lab or fiber frame of reference). Although many rotationally invariant DTI metrics have been prosed, we will review only those widely used clinically: tensor trace and fractional anisotropy (FA).

Trace

[2]To illustrate the rotational invariance of the eigenvalues, consider the diffusion tensor measured in the lab frame, $\mathbf{D}$, and in the principal frame, $\mathbf{\Lambda}$. The 3 eigenvalues of each tensor are the same: λ_1, λ_2, and λ_3

The trace I_1 of the diffusion tensor is defined as

$$I_1 = \mathrm{Tr}(\mathbf{D}) = \mathrm{Tr}(\mathbf{\Lambda}) = D_{xx} + D_{yy} + D_{zz} = \lambda_1 + \lambda_2 + \lambda_3, \tag{4.8}$$

and is a measure of diffusion isotropy in tissue [19]. We can see from Eq. (3.16) that the MSD is a scaled-up version of the tensor trace: $MSD = 2\tau_d \mathrm{Tr}(\mathbf{D})$. In a healthy, adult human brain the trace is observed to be uniform across the parenchyma. Specifically, its value is very similar in normal white and gray matter [62].

Fractional Anisotropy

A sphere is a geometric representation of diffusion isotropy. Hence, the deviation from a spherical shape, or eccentricity, can be used to characterize diffusion anisotropy. The fractional anisotropy (FA) [19] is the most widely used diffusion anisotorpy measure, and it is a measure of the diffusion ellipsoid eccentricity. Specifically, it is the ratio of the standard deviation (std) of the eigenvalues to the root mean square (rms) of the eigenvalues:

$$\begin{aligned} \mathrm{FA} &= \frac{\mathrm{std}[\lambda_1, \lambda_2, \lambda_3]}{\mathrm{rms}[\lambda_1, \lambda_2, \lambda_3]} \\ &= \frac{\sqrt{\frac{\sum_{i=1}^{3}(\lambda_i - \langle\lambda\rangle)^2}{2}}}{\sqrt{\frac{\sum_{i=1}^{3}\lambda_i^2}{3}}} \\ &= \sqrt{\frac{3}{2}}\sqrt{\frac{\sum_{i=1}^{3}(\lambda_i - \langle\lambda\rangle)^2}{\sum_{i=1}^{3}\lambda_i^2}}, \end{aligned} \tag{4.9}$$

where $\langle\lambda\rangle$ is the mean eigenvalue. The FA has the advantage of being automatically normalized to the interval $[0, 1]$ - FA=0 for an isotropic medium, and FA=1 for a cylindrically symmetric anisotropic medium (with $\lambda_1 \gg \lambda_2 = \lambda_3$).

4.1.4 Limitations of DTI

If an imaging voxel contains a single fiber bundle, DTI is able to sucessfully resolve the fiber orientation, which coincides with the principal eigenvector. However, what happens when the imaging voxel contains multiple fiber orientations (e.g. two or more fiber bundles crossing)? Multiple fiber orientations are endemic to dMRI due its coarse resolution ($\sim$ 2 to 3 mm) compared with the white matter structures of interest (e.g. the pyramidal tracts are only $\sim$ 3 mm thick in subcortical regions) [20]. It is estimated that multiple fiber orientations arise in more than 90% of the white matter voxels in a standard spatial resolution brain image [71]. In this situation, the inherent Gaussian assumption of DTI proves a liability. The Gaussian function has only a single directional maximum, as is the case for a single fiber orientation. Crossing fibers, however, have multiple maxima and so can not be described by a single Gaussian function. Consequently, voxels containing crossing fibers become partial volumed and have artifically reduced anisotropy [2, 42, 77].

Higher angular resolution, which can be obtained by increasing the b-value, can help delineate complex fiber architecture like crossing fibers. According to Eq. (3.22), if we plot $\ln(S)$ vs. b-value for neuronal tissue, the resulting signal decay will be linear with respect to b-value. However, many studies [7, 31, 56, 57] have reported that this linear decay is only observed at low levels of diffusion-weighting (e.g. $b < 1500$ s/mm^2), while

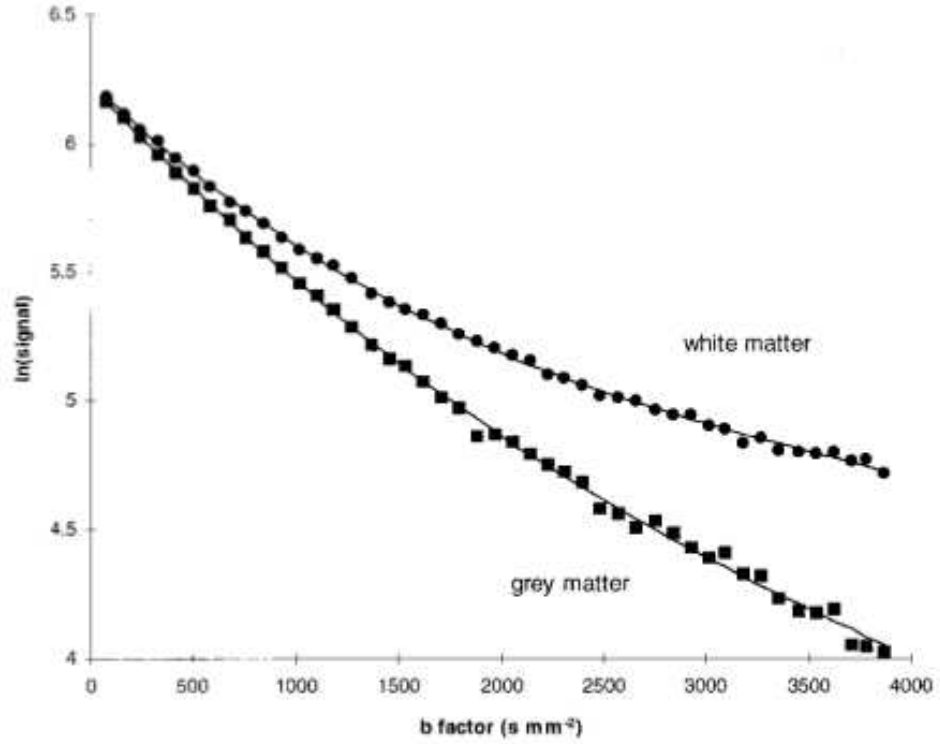

Figure 4.2: Typical signal decay curves in human brain white matter and gray matter. Initially, the decay curves are linear, but as b increases, the signal decays at a slower rate (more so for white matter than grey matter). Adapted from [31].

at higher levels the signal decay in neuronal tissue becomes non-linear, as illustrated in Fig. 4.2. Consequently, DTI is not a feasible model for high angular resolution, i.e. high b-value, experiments. The non-Gaussian behavior of the signal decay in white matter at higher b-values is consistent with the occurrence of restricted diffusion in white matter at longer diffusion times (refer to Fig. 3.3) because an increase in the diffusion time corresponds to an increase in the b-value (see Eq. 3.25), and so implying that restricted diffusion is a high b-value phenomenon.

4.1.5 Sophisticated DTI Modeling

One way to resolve crossing fibers within the DTI framework is to employ a Gaussian mixture model [73]. That is, we assume each imaging voxel consists of several diffusion compartments, which are non-exchanging, and where each compartment is described by Eq. (3.22). In the case of a voxel comprised of two crossing fibers, we have

$$E\mathbf{q} = fe^{-4\pi^2\tau_d\mathbf{q}^T\mathbf{D}_1\mathbf{q}} + (1-f)e^{-4\pi^2\tau_d\mathbf{q}^T\mathbf{D}_2\mathbf{q}}, \tag{4.10}$$

where $\mathbf{D}_1$ and $\mathbf{D}_2$ are the diffusion tensors for the first and second fiber, respectively, and f is the volume fraction of the first fiber's diffusion compartment. Now, there are 13 parameters to estimate in each voxel instead of the standard 6 (discarding the baseline signal). The above equation can not be solved using linear least squares. Rather, a non-linear optimization has to be carried out to estimate the parameters. The authors in [73] employed a gradient descent scheme to estimate the parameters in Eq. (4.10). In addition to the complexity of the numerical estimation, Eq. (4.10) is further limited by its inherent assumption (via the tensor model) that the diffusion in each compartment

is Gaussian. Thus, Eq. (4.10) is not a feasible model for $b > 2000$ s/mm^2.

4.2 Moving Beyond DTI: High b-value Imaging

DTI's inherent inability to resolve complex fiber architechture and the collapse of the Gaussian assumption at high b- (or q-) values has led to a plethora of high b-value[3] dMRI methods being proposed. These methods can be divided into two categories: parametric and non-parametric. Non-parametric methods focus on reconstructing mathematical descriptors of the diffusion profile without recourse to a specific assumption of diffusion behavior. Parametric methods assume an imaging voxel can be divided into several distinct, non-exchanging diffusion compartments, where each compartment is mathematically described by a distribution function[4]. DTI can be thought of as the simplest parametric model because it assumes an imaging voxel has a single diffusion compartment that is described by a Gaussian function.

As mentioned earlier, an attractive feature of high b-value imaging is the increased angular resolution. However, the biological mechanisms behind the consequential deviation from Gaussianity at high b-values are not well understood. Some studies [31, 56, 57] have assumed that a bi-exponential function can be used to characterize the non-monoexponential signal decay of water in neuronal tissue, where each diffusion compartment within a voxel is composed of a fast- and a slow-diffusing Gaussian component. Assaf and Cohen [9] have attributed the non-Gaussianity of the white matter signal decay to hindered extra-axonal and restricted intra-axonal contributions, terming their model

[3]By high b-value, we mean $b > 2000$ s/mm^2.

[4]In many cases, the distribution function is assumed to be Gaussian

composite hindered and restricted model of diffusion (CHARMED). CHARMED models the hindered diffusion by a Gaussian function and the restricted diffusion by diffusion inside a cylinder (non-Gaussian function).

A major disadvantage of the two aforementioned parametric methods (or any parametric method for that matter) is their assumption of a specific diffusion behavior (e.g. fast and slow Gaussians, hindered and restricted diffusion), which is especially problematic at high b-values since there is no consensus among researchers regarding the biological mechanisms underlying high b-value phenomena (e.g. restricted diffusion). Hence, if the biological assumptions turn out to be false, the model collapses in on itself. For this reason, non-parametric modeling may be better suited to high b-value imaging. In the following sections, we'll discuss a few well-established non-parametric high b-value methods.

4.2.1 Q-Ball Imaging

As mentioned earlier, a mathematical descriptor of the diffusion profile that does not a priori assume a specific diffusion behavior may be more appropriate for high b-value experiments. One such construct is the orientation distribution function (ODF), which is a spherical measure that maps the orientational architechture of tissue. Specifically, the maxima of the ODF are aligned with the fiber directions.

Q-ball imaging (QBI) [72] is a non-parametric dMRI technique proposed by David Tuch that estimates the ODF from the (raw) q-space data. It was the first method seeking to superscede the diffusion tensor framework with a natural mathematical descriptor of the diffusion, in this case the ODF. QBI samples the diffusion signal on a spherical shell

in q-space, and hence is a single b-value technique like DTI. Tuch defined the ODF is the zeroth order radial projection of the EAP:

$$\mathrm{ODF}(\mathbf{v}) = \int_0^\infty P(p, \mathbf{v}) dp, \tag{4.11}$$

where $\mathbf{p} = p\mathbf{v}$ and $\mathbf{v}$ is a 3D unit vector. Thus, the ODF is a function on the unit sphere describing the probability averaged over the voxel that a water molecule will diffusion into any given solid angle $\mathbf{v}$.

The mathematical transform employed in QBI is the Funk-Radon transform (FRT), also known as the spherical Radon transform or simply the Funk transform. The FRT is an extension of the planar Radon transform to the sphere. Consider a function existing on the sphere $f(\mathbf{u})$, where $\mathbf{u}$ is a 3D unit vector. The FRT of $f(\mathbf{u})$ for a direction $\mathbf{v}$ is defined as

$$\mathrm{FRT}[f(\mathbf{u})](\mathbf{v}) = \int \delta(\mathbf{u}^T\mathbf{v}) f(\mathbf{u}) d^2\mathbf{u} = \int_0^{2\pi} \int_0^{\pi} \delta(\mathbf{u}^T\mathbf{v}) f(\mathbf{u}) \sin\theta d\theta d\phi \tag{4.12}$$

Now, QBI doesn't sample all of q-space but rather confines the samples to a single sphere of radius q'. For such a case, Tuch was able to show that the ODF can be approximated as the FRT of the q-space diffusion signal existing on a sphere of radius q':

$$\mathrm{ODF}(\mathbf{v}) = \mathrm{FRT}_{q'}[E(\mathbf{q})] = \int \delta(\mathbf{u}^T\mathbf{v}) E(q', \mathbf{u}) d^2\mathbf{u} \tag{4.13}$$

QBI uses a larger number of encoding directions than DTI, ranging from as low as 60 up to several hundred. Although its scan time is not as short as DTI, the QBI framework doesn't invoke any prior assumptions on the diffusion and can resolve crossing fibers.

QBI, however, has several key disadvantages. According to Eq. (4.11), the exact ODF requires measurements of the diffusion signal across all of q-space, which entails multiple b-value imaging. By limiting the samples to lie on a single sphere, QBI can only compute an approximated ODF. Most importantly, the ODF is an angular feature of EAP, retrieving only the angular content of the diffusion process. The absence of the radial information means that the ODF gives an incomplete picture of the diffusion process. Lastly, many important high angular resolution analogues of DTI indices are scalar features of the EAP, itself, and not the ODF.

4.2.2 EAP Imaging

The EAP provides more information about tissue microstructure than the ODF because it captures both the radial and angular information contained in the diffusion profile. Significantly, the EAP profiles illustrate and recover crossing fibers. In q-space, the EAP is the Fourier transform of the q-space diffusion signal. Consequently, in order to reasonably estimate the EAP, a somewhat thorough exploration of q-space is necessary. Hence, the estimation of the EAP requires a combination of high angular sampling at multiple b-values.

A reasonable approach to estimating the EAP directly from the signal, i.e. evaluating Eq. (3.29), is using the Fast Fourier Transform (FFT). As it turns out, such a approach is the most common, and the two main FFT-based methods are diffusion spectrum imaging

(DSI) [75] and hybrid diffusion imaging (HYDI) [80]. These two methods employ different sampling schemes, which are illustrated in Fig. 4.3, in estimating the EAP via the FFT. DSI is based on direct sampling of the diffusion signal on a Cartesian q-space lattice. A major advantage of DSI is that the EAP is estimated without any prior assumptions regarding the diffusion behavior. However, two major issues impede clinical use of DSI:

1. DSI requires dense sampling of the Cartesian lattice ($\sim$ 500 samples is typical), resulting in very long scan times.

2. DSI requires very high magnetic field gradients to thoroughly explore q-space, with b_{max} going up to 17000 s/mm^2.

HYDI samples the diffusion signal along concentric spherical shells (each shell represents a b-value) in q-space. The number of gradient directions is increased with each shell to increase the angular resolution with the level of diffusion weighting. Data from inner shells (low b-values) can be used for DTI, while QBI can be applied to the outermost shell data. Combining all shells, the entire HYDI data may be used to estimate the EAP using DSI. Since the FFT scheme employed in DSI requires the data to lie on a Cartesian grid, the authors in [80] propose regridding the measurements onto a 9 x 9 x 9 Cartesian lattice via bilinear interpolation. A major advantage of HYDI is that it uses much fewer samples ($\sim$ 120) than DSI, making it more clinically feasible. However, the HYDI EAP reconstruction may suffer from the *ad hoc* signal interpolation and regridding.

The FFT is impractical for methods employing spherical q-space sampling schemes, such as HYDI, since the FFT requires data to lie on a Cartesian grid. Solving the Fourier transform in spherical coordinates (i.e. spherical Fourier transform) obviates the need

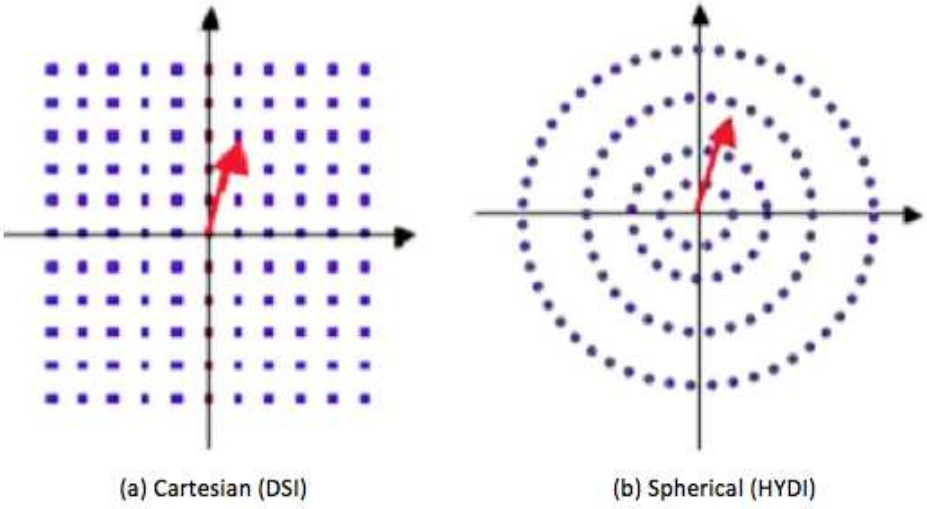

Figure 4.3: Different q-space sampling schemes used to reconstruct the EAP. The blue marks denote the gradient directions, i.e. samples. To the left is the Cartesian lattice used in DSI. Spherical sampling, the type employed in HYDI, is illustrated in the right, and consists of a series of concentric spherical shells. The q-radius of each spherical shell corresponds to the shell's b-value. Adapted from [37].

for the FFT and *ad hoc* processing. Analytic methods, seeking to obtain a closed-form solution of the EAP, pursue such a route.

4.3 Data Acquisition Technique for Diffusion MRI: Echo-Planar Imaging

Since dMRI is sensitized to the displacement of water molecules, which is on the order of $5-15$ μm assuming typical measurement times, it is highly sensitive to motion. A small amount of subject motion or physiological motion (e.g. breathing, swallowing, cardiac pulsation) can cause a significant amount of signal phase shift or signal loss, which can severely affect image quality [58, 67, 74]. Hence, an appropriate imaging sequence for dMRI is one that is very robust against motion artifacts and can sample k-space relatively quickly, and hence reducing the likelihood of additional motion artifacts arising. For this reason, the most common method for sampling k-space in dMRI is the diffusion-weighted single-shot echo-planar imaging (DW-SS-EPI) sequence. SS-EPI is the fastest acquisition method in MRI, where all of k-space is read out after a single radiofrequency excitation, and its diffusion-weighting is achieved via the PGSE approach.

The DW-SS-EPI sequence is illustrated in Fig. 4.4, where a 90° RF excitation pulse is applied to scan all of k-space and is followed by a 180° refocusing pulse. A large diffusion gradient, of duration δ, is placed on both sides of the 180° refocusing pulse. The first gradient pulse dephases the magnetization across the voxel, while the second pulse rephases the magnetization. For stationary (nondiffusing) molecules, the phases induced by both gradient pulses completely cancel out, and so there will be no signal attenuation arising from diffusion. In the case of diffusing molecules, there will be a

net phase difference between the two pulses, which is related to the diffusion signal attenuation.

To see how SS-EPI is robust against motion artifacts, lets consider the case of acquiring an image of dimension 128 x 128. In conventional MR imaging, the k-space data is recorded line-by-line, requiring 128 independent scans, with each scan corresponding to one line. Now what will happen when bulk motions are present during the acquisition? Since each scan is independent of the other, the amount of (nonreproducible) phase shift due to motion artifacts will vary from scan to scan, which leads to misregistration of proton signals after the Fourier transform. Such misregistration appears as ghosting in the image (i.e. Fourier transform of k-space data). In SS-EPI, however, the entire k-space is recorded within one scan, and so the entire k-space obtains the same amount of phase error arising from motion artifacts, which (in theory) means the Fourier transform will only be modulated by a fixed phase error term that can be ignored. For this reason, SS-EPI (unlike conventional MR imaging) is much less sensitive to motion artifacts like ghosting.

There are several key points worth emphasizing. First, the phase errors caused by subject and physiological motions always exist in conventional MRI. However, they are more pronounced in dMRI because of the application of strong diffusion-weighting gradients. Second, the rapidity of SS-EPI prevents additional motion-induced phased errors from arising. Lastly, SS-EPI is robust against motion artifacts not because it is very rapid, but because (as discussed in the previous paragraph) it is less sensitive to phase errors.

Although it offers enhanced robustness against motion artifacts and reduced scan

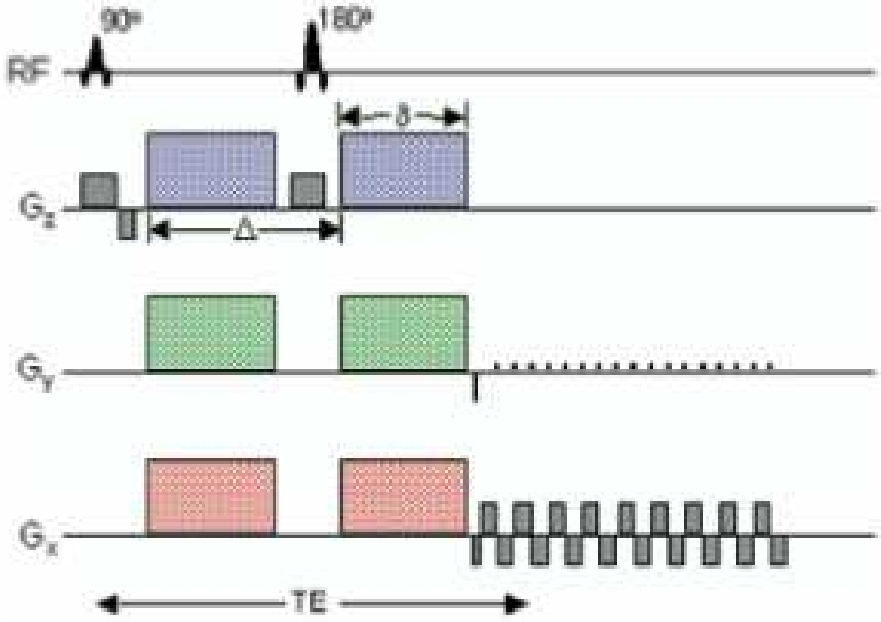

Figure 4.4: Schematic diagram of a diffusion-weighted single-shot echo-planar imaging (DW-SS-EPI) pulse sequence. Diffusion weighting is achieved via the PGSE approach. Adapted from [3].

time compared to conventional MR imaging sequences, SS-EPI has several key disadvantages. Specifically, SS-EPI acquisitions suffer from eddy current-induced distortions and B_o susceptibility effects.

Eddy Currents

In EPI, the diffusion gradients are rapidly switched on and off, which results in eddy current formation. Specifically, when the diffusion gradients are switched on and off, the time-varying magnetic field of the gradients generates eddy currents in the electrically conductive structures of the MRI scanner. These eddy currents, in turn, produce additional unwanted, rapidly and slowly decaying magnetic fields. Consequently, the sampled trajectory in k-space will be modified and, as a result, geometric distortions will be introduced in the diffusion-weighted images. These distortions affect each diffusion-weighted image differently, which can result in voxels in different diffusion-weighted images to be misaligned. Another deleterious effect of eddy currents is that a sample's actual gradient direction differs from the prescribed gradient direction $\mathbf{G}$, resulting in a difference between the actual and prescribed b-value for each gradient direction. Since high b-value imaging requires much stronger gradients than DTI, eddy distortion is more pronounced in high b-value images.

In low b-value methods like DTI, the eddy distortions are mostly linear and global, which can be corrected in post-processing. Registration-based methods form the most common approach, which model the eddy distortion in terms of translation, shear, and scaling operations. They use the $b = 0$ image as the nondistorted reference image to unwrap the distorted diffusion-weighted images. In doing so, the 12-mode affine transformation is highly effective [44]. However, registration-based methods are inadequate for high b-values because of the varying contrast in images acquired with different diffu-

sion gradients and the low SNR.

Magnetic Susceptibility Effects (i.e. EPI Distortion)

Large differences in bulk magnetic susceptibility (i.e. pronounced B_o inhomogeneity), such as those occurring at tissue-air interfaces, induce local magnetic field gradients that severely distort diffusion-weighted images along the phase-encode direction. These magnetic susceptibility-induced geometric distortions are particularly problematic during EPI, and are perhaps the most troubling type of artifact in dMRI-EPI. In the brain susceptibility effects are most acute in regions adjacent to the sinuses, such as the inferior regions of the frontal lobe, the anterior pole of the temporal lobe, and the pons. Unlike eddy current distortion, EPI distortion affects all $b = 0$ and diffusion-weighted images in the same way.

EPI distortion is intimately linked to resolution and field strength. As the resolution of an EPI-acquired image increases, the greater the geometric distortion. For this reason, the resolution is lowered as much as possible in a dMRI experiment. The amount of distortion also increases as the field strength increases - a 3 T scanner produces more EPI distortion than a 1.5 T scanner.

There are several (non-retrospective) ways to minimize EPI distortion, besides simply lowering the resolution. One of the most effective approaches is parallel imaging, which was introduced in the late 1990s [63]. Parallel imaging requires multiple receiver channels and a special head coil to simultaneously and independently acquire MR signals. It substantially reduces B_o susceptibility artifacts by reducing both the echo train length and echo spacing, while retaining the robustness to motion of SS-EPI. The degree of the distortion reduction is quantified by the parallel imaging factor (shortened to p-factor

in the literature), which satisfies $p \geq 2$. The higher the p-factor, the shorter the echo train length, and so resulting in a greater reduction of EPI distortion. However, the SNR degrades as the p-factor increases, and so there is a tradeoff in parallel imaging between SNR and distortion reduction. Currently, the p-factor is practically limited to 2-4 depending on the number of receiver channels and coil geometry.

Susceptibility-induced distortions can also be ameliorated by B_o field map correction. An effective way of computing the field map is to take advantage of the complementary information included in pairs of diffusion images acquired with reversed phase-encoding directions. Reversing the phase-encoding direction flips the sign of the susceptibility-induced distortions as well. A susceptibility-induced off-resonance field map can be estimated by combining pairs of reversed phase-encoding images. The acquired images can be then be corrected for EPI distortion by exploiting the field map [4]. Since EPI distortion affects all $b = 0$ and diffusion-weighted images in the same manner, only a single field map is needed to correct for EPI distortion[5]. Typically, the field map is estimated from the $b = 0$ images (i.e. acquiring pairs of reversed phase-encoding $b = 0$ images), and is subsequently applied to the diffusion-weighted images.

[5]Since eddy distortion affects each diffusion-weighted image differently, field map correction should be applied after correction for eddy distortion.

Chapter 5

Bessel Fourier Orientation Reconstruction (BFOR): An Analytical Diffusion Propagator Reconstruction for Hybrid Diffusion Imaging and Computation of q-Space Indices

5.1 Abstract

The ensemble average propagator (EAP) describes the 3D average diffusion process of water molecules, capturing both its radial and angular contents. The EAP can thus

provide richer information about complex tissue microstructure properties than the orientation distribution function (ODF), an angular feature of the EAP. Recently, several analytical EAP reconstruction schemes for multiple **q**-shell acquisitions have been proposed, such as diffusion propagator imaging (DPI) and spherical polar Fourier imaging (SPFI). In this study, a new analytical EAP reconstruction method is proposed, called Bessel Fourier orientation reconstruction (BFOR), whose solution is based on heat equation estimation of the diffusion signal for each shell acquisition, and is validated on both synthetic and real datasets. A significant portion of the paper is dedicated to comparing BFOR, SPFI, and DPI using hybrid, non-Cartesian sampling for multiple b-value acquisitions. Ways to mitigate the effects of Gibbs ringing on EAP reconstruction are also explored. In addition to analytical EAP reconstruction, the aforementioned modeling bases can be used to obtain rotationally invariant q-space indices of potential clinical value, an avenue which has not yet been thoroughly explored. Three such measures are computed: zero-displacement probability (Po), mean squared displacement (MSD), and generalized fractional anisotropy (GFA).

5.2 Introduction

The aim of diffusion-weighted imaging (DWI) is to non-invasively recover information about the diffusion of water molecules in biological tissues. The most common form of DWI is diffusion tensor imaging (DTI) [18], which is a good model of diffusion-weighted signal behavior at low levels of diffusion weighting. However, DTI is limited by the Gaussian assumption, which is invalid at higher levels of diffusion weighting ($b > 2000$ s/mm^2) and its inability to resolve multiple fiber orientations within a voxel [2,42,77]. In order to recover complex white matter (WM) geometry, high angular resolution diffusion

imaging (HARDI) [73], which reduces the diffusion signal sampling to a single sphere (i.e. single level of diffusion weighting) within q-space, was proposed. Many HARDI techniques [1,25,36,45,72] seek to extract the orientation distribution function (ODF), a probability density function describing the angular distribution of water molecules during diffusion. Unlike apparent diffusion coefficient (ADC) profiles, the maxima of the ODF are aligned with the fiber directions, making it useful in fiber tractography applications. However, the ODF only retrieves the angular content of the diffusion process.

The ensemble average propagator (EAP) provides more information about tissue microstructure than the ODF because it captures both the radial and angular information contained in the diffusion signal. The ODF, mathematically defined as the radial projection of the EAP, is simply an angular feature of the EAP. Unlike the diffusion tensor, the EAP profiles illustrate and recover crossing fibers. The authors in [32] have suggested that the radial part of the diffusion signal may be sensitive to WM disorders caused by demyelination and could be used to infer the axonal diameter.

The estimation of the EAP requires combination of high angular sampling at multiple levels of diffusion weighting. Under the narrow pulse assumption [68], the diffusion signal attenuation, $E(\mathbf{q})$ in q-space and the EAP, $P(\mathbf{p})$, are Fourier Transform (FT) pairs [23]:

$$P(\mathbf{p}) = \int E(\mathbf{q}) e^{-2\pi i \mathbf{q}\cdot\mathbf{p}} d^3\mathbf{q}, \tag{5.1}$$

where $E(\mathbf{q}) = S(\mathbf{q})/S_o$ is the normalized q-space diffusion signal, $S(\mathbf{q})$ is the diffusion signal measured at position $\mathbf{q}$ in q-space, and S_o is the baseline image acquired without any diffusion gradients ($q = 0$). We denote $\mathbf{q} = q\ \mathbf{u}(\theta, \phi)$ and $\mathbf{p} = p\ \mathbf{r}(\theta', \phi')$, where $\mathbf{u}$ and $\mathbf{r}$ are 3D unit vectors. The wave vector $\mathbf{q}$ is $\mathbf{q} = \gamma\delta\mathbf{G}/2\pi$, where γ is the nuclear

gyromagnetic ratio and $\mathbf{G} = g\mathbf{u}$ is the applied diffusion gradient direction. The norm of the wave vector, q, is related to the diffusion weighting level (b-value) via $b = 4\pi^2 q^2(\Delta - \delta/3)$ [17], where δ is the duration of the applied diffusion gradients and Δ the time between the two pulses. Eq. (5.1) is valid only if the narrow pulse condition is met, which is rarely the case for q-space diffusion MRI performed under experimental conditions. Several studies [15, 53, 75] however, have shown that even when these assumptions do not hold, the Fourier relationship in Eq. (3) is still a reasonable approximation of the microstructural features. The diffusion displacements, however, will be consistently underestimated [75].

Various methods already exist to reconstruct the EAP. Using the diffusion tensor framework, the EAP is simply described by a multivariate Gaussian function [18]. The authors in [43] presented a closed-form approximation of the EAP using higher order tensors, specifically the 4^{th} order diffusion tensor. The diffusion orientation transform (DOT) [61] is a HARDI technique that computes the iso-radius of the EAP. DOT assumes the radial diffusion follows a mono-exponential decay, which allows the radial integration in Eq. (5.1) to be solved analytically. The spherical integration is then solved numerically. The application of this technique, however, is limited by its mono-Gaussian assumption of the radial diffusion decay. In addition, the single shell approach of DOT gives an incomplete picture of the EAP, whose estimation requires signal measurements along all of q-space.

EAP reconstruction techniques using multiple diffusion weighting acquisitions can be divided into two strategies: Fast Fourier Transform (FFT) based and analytical. FFT based methods include diffusion spectrum imaging (DSI) [24, 75] and hybrid diffusion imaging (HYDI) [64, 80]. DSI is based on direct sampling of the diffusion signal on a

Cartesian q-space lattice. The FT in Eq. (5.1) is then numerically evaluated via FFT to obtain the EAP. A major advantage of DSI is that the EAP is estimated without any prior assumptions of behavior of the diffusion signal. However, DSI requires dense sampling of the Cartesian lattice, resulting in very long acquisition times. HYDI samples the diffusion signal along concentric spherical shells in q-space, with the measurements then being interpolated and regridded onto a $9 \times 9 \times 9$ Cartesian lattice so that the EAP can be similarly reconstructed as in DSI. HYDI uses much fewer samples than DSI, making it more clinically feasible. However, the HYDI propagator reconstruction may suffer from the *ad hoc* signal interpolation and regridding.

The FFT is impractical for methods employing spherical q-space sampling schemes, such as HYDI, since the FFT requires data to lie on a Cartesian grid. It is also quite computationally expensive. Solving the FT in spherical coordinates (i.e. spherical Fourier Transform) instead, obviates the need for FFT and *ad hoc* processing. Analytic methods, seeking to obtain a closed-form solution of the EAP, pursue such a route. Currently, the two main analytical EAP reconstruction schemes are diffusion propagator imaging (DPI) [37] and spherical polar Fourier imaging (SPFI) [12, 28, 29].

DPI assumes that $E(\mathbf{q})$ is a solution to the 3D Laplace's equation $\bigtriangledown^2 E = 0$, which results in the signal basis being composed of the regular and irregular solid harmonics. It is fast, and seems to work well with only a small number of samples. However, the DPI signal basis is an unrealistic model of $E(\mathbf{q})$ because Laplacian modeling of diffusion signal entails that (1) $E(0)$ does not exist, which arises from the irregular solid harmonic term, and (2) MSD of water molecules is zero, which will be proved in the **Theory** section. In addition, the DPI signal basis lacks orthonormality, and hence does not possess the robust numerical stability that would otherwise feature in an orthonormal basis.

SPFI models the diffusion signal in terms of an orthonormal basis comprising the spherical harmonics (SH) and Gaussian-Laguerre polynomials. The SPFI signal basis is, in fact, a modified solution of the 3D quantum mechanical simple harmonic oscillator problem. It is robust to noise and low anisotropy, and works well with just a few number of samples. However, SPFI has not been tested at $b > 3000$ s/mm^2. A slightly modified version of the SPFI signal basis was proposed just recently by the authors in [27]. This paper, however, will only be concerned with the original SPFI basis.

A closely related basis to SPFI was proposed in [59, 60], which use the Hermite polynomials to estimate the 1D q-space diffusion signal. In addition to forming a complete orthogonal basis, the Hermite polynomials are also eigenfuctions of the Fourier transform. However, the 3D EAP solution has yet to be derived using this basis.

With respect to analytical EAP reconstruction methods, one valuable though overlooked use is in extracting rotationally invariant quantitative measures from them. Recently, the authors in [11] used the SPFI signal basis to compute the novel fiber population dispersion (FPD), an index which assess the presence of crossing fibers within a voxel. The FPD, however, is a relatively new measure that has not yet been computed for an actual human brain. More well-established q-space metrics include generalized fractional anisotropy (GFA) [72], mean squared displacement (MSD) [10, 80], and zero-displacement probability (Po) [10]. All three are simply scalar features of the EAP, and the GFA & MSD can be viewed as high angular resolution analogues of the DTI indices fractional anisotropy (FA) and mean diffusivity (MD) [19], respectively. An analytical representation of the EAP (and hence diffusion signal) can facilitate either analytic computation of such features or numerical efficiency in estimating them.

In this paper, we present Bessel Fourier Orientation Reconstruction (BFOR) [46]. Rather than assuming the signal satisfies Laplace's equation, we reformulate the problem into a Cauchy problem and assume $E(\mathbf{q})$ satisfies the heat equation. The heat equation is a generalization of Laplace's equation, which the latter approaches at the steady state (i.e. $t \to \infty$). BFOR provides an analytical reconstruction of the EAP profile from diffusion signal and models the diffusion signal in terms of an orthonormal basis. In addition, it contains an intrinsic exponential smoothing term that allows one to control the amount of smoothing in the EAP estimation. The last point is significant because, although the Laplacian modeling intrinsically smoothes the diffusion signal, the amount of smoothing can not be controlled, and hence it may oversmooth the signal. In addition to heat diffusion smoothing, we also look at linear signal extrapolation as a potential means to mitigate the effects of common artifacts afflicting the reconstructed EAP profile, such as Gibbs ringing and signal truncation. Employing a hybrid, non-Cartesian encoding scheme in both synthetic and *in vivo* datasets, we reconstruct the EAP using BFOR, SFPI, and DPI and assess their performances. Lastly, we use BFOR to compute GFA, Po, and MSD, and compare BFOR's accuracy in estimating such indices to that of DPI and SPFI.

The paper is organized as follows: in **Theory Section**, we develop BFOR, first by describing how to estimate the diffusion signal, and then deriving the analytical solution for the EAP using Eq. (5.1). Scalar features of the EAP are also introduced in this section. The **Appendix** carefully details the derivations of the BFOR signal basis, EAP, and q-space indices. In **Material and Methods Section**, we describe the implementation details of BFOR and present the synthetic and *in vivo* human brain datasets that will be used to validate and illustate BFOR and compare it to SPFI and DPI in **Results Section**. Lastly, we discuss our results and future applications of

analytical EAP methods in **Discussion Section**.

5.3 Theory

The heat equation is ubiquitous in the natural sciences, arising in Fick's law of diffusion, Brownian motion, Fourier's law of thermal conduction, and the price variation over time of stocks. A nice feature of any solution to the heat equation is its temporal dependence, which can be viewed as an inherent smoothing control mechanism. DPI, by solving the heat equation at the steady state, has no smoothing control mechanism, and so can potentially oversmooth the signal. Smoothing can be useful in situations where reconstrutions greatly suffer from noise. Although our method is similar in spirit to DPI and SPFI, it significantly differs from them due to its inclusion of a smoothing term.

Consider the eigenvalue/boundary condition problem

$$\Im_{\mathbf{q}}\psi_i(\mathbf{q}) = -\lambda_i\psi_i(\mathbf{q}), \quad \psi_i(q=\tau,\mathbf{u}) = 0 \tag{5.2}$$

which we use to solve the Cauchy problem

$$\frac{\partial}{\partial t}g(\mathbf{q},t) - \Im_{\mathbf{q}}g(\mathbf{q},t) = 0, \quad g(\mathbf{q},t=0) = f(\mathbf{q}), \tag{5.3}$$

where $f(\mathbf{q})$ is simply the acquired signal and $\Im$ is some self-adjoint linear operator. We

require $\lambda > 0$. Chung et al. in [30] derived a unique solution for (5.3):

$$g(\mathbf{q}, t) = \sum_{i=0}^{\infty} a_i e^{-\lambda_i t} \psi_i(\mathbf{q}), \tag{5.4}$$

where $e^{-\lambda_i t}$ is a smoothing term controlled by parameter $t \geq 0$ and the coefficients are given by $a_i = \langle f, \psi_i \rangle$. The implication of Eq. (5.4) is that the solution decreases exponentially as t increases and smoothes out high spatial frequency noise much faster than low-frequency noise. In DPI, however, the steady state assumption permanently removes any temporal term, which governs the extent of smoothing, so there is no smoothing control mechanism. Note that $t = 0$ corresponds to no smoothing being applied.

Assuming that $\Im = \bigtriangledown^2$, where $\bigtriangledown^2$ is the 3D Laplacian operator in spherical coordinates, Eq. (5.2) becomes

$$\left[\frac{1}{q^2} \frac{\partial}{\partial q} (q^2 \frac{\partial}{\partial q}) + \frac{1}{q^2 \sin\theta} \frac{\partial}{\partial \theta} (\sin\theta \frac{\partial}{\partial \theta}) + \frac{1}{q^2 \sin^2\theta} \frac{\partial^2}{\partial \phi^2} \right] \psi_i(\mathbf{q}) = -\lambda_i \psi_i(\mathbf{q}) \tag{5.5}$$

Eq. (5.5) can be solved via separation of variables to obtain an orthonormal basis, which we show in **Appendix A**:

$$\psi_{nj}(\mathbf{q}) = j_{l(j)}(\frac{\alpha_{nl(j)} q}{\tau}) Y_j(\mathbf{u}), \tag{5.6}$$

where $\alpha_{nl(j)}$ is n^{th} root of l^{th} order spherical Bessel function of first kind j_l and τ is the radial distance in q-space at which the Bessel function goes to zero. Y_j are a modified real and symmetric SH basis proposed in [37] to reflect the symmetry and realness of the

diffusion signal. The index $j := j(l,m) = (l^2+l+2)/2+m$ is defined for $l = 0, 2, 4, ...$ and $m = -l, ..., 0, ..., l$. Hence, for $j = \{1, 2, 3, 4, 5, 6, 7, ...\}$, $l(j) = \{0, 2, 2, 2, 2, 2, 4, ...\}$. The eigenvalues are $-\lambda_{nl(j)} = -\frac{\alpha^2_{nl(j)}}{\tau^2}$. The SH are also used to model the angular profile of the diffusion signal in DPI and SPFI.

Within the context of our problem, $g(\mathbf{q}, t)$ is the diffusion signal.The assumption of a Laplacian operator results in Eq. (5.3) becoming the heat equation: $\bigtriangledown^2 E(\mathbf{q}, t) = \frac{\partial E(\mathbf{q},t)}{\partial t}$. From Eq. (5.4) then, the diffusion signal can be expanded in terms of the spherical orthonormal basis ψ_{nj} given in Eq. (5.6):

$$E(\mathbf{q}, t) = \sum_{n=1}^{N}\sum_{j=1}^{R} C_{nj} e^{\frac{-\alpha^2_{nl(j)}t}{\tau^2}} j_{l(j)}(\frac{\alpha_{nl(j)}q}{\tau}) Y_j(\mathbf{u}), \tag{5.7}$$

where C_{nj} are the expansion coefficients, $R = \frac{(L+1)(L+2)}{2}$ is the number of terms in the modified SH basis of truncation order L, and N is the number of roots for any spherical Bessel function of order l. The total number of coefficients in the expansion is $W = \frac{N(L+1)(L+2)}{2}$. Note that the actual acquired signal from scanner is given at $t = 0$. In DWI, $E(0) = 1$, and so for our basis, we obtain the following identity (derived in **Appendix B**):

$$E(q = 0, \mathbf{u}, t = 0) = \frac{1}{\sqrt{4\pi}} \sum_{n} C_{n1} = 1, \tag{5.8}$$

which holds for any $\mathbf{u}$ within the unit sphere S^2 (i.e. $\mathbf{u} \in S^2$).

An important property of the diffusion signal is that it asymptotically approaches zero as $q \to \infty$. However, the spherical Bessel function infinitely oscillate about zero, as

shown in Fig. 5.1, so a finite upper bound τ is needed at which the BFOR signal model becomes zero. Mathematically, τ ensures that the spherical Bessel function is orthogonal in the domain $[0, \tau]$. The fact that the radial basis in BFOR does not radially decay to zero but becomes zero at some point in q-space is the main limitation of the BFOR algorithm.

In deriving the EAP, the spherical integration of Eq. (5.1) is made easier by expressing the Fourier kernel as a plane wave expansion:

$$e^{-2\pi i \mathbf{q}\cdot\mathbf{p}} = 4\pi \sum_{j=1}^{\infty} (-i)^{l(j)} j_{l(j)}(2\pi qp) Y_j(\mathbf{u}) Y_j(\mathbf{r}) \tag{5.9}$$

Substituting Eq. (5.7) and (5.9) into Eq. (5.1), we obtain

$$\begin{aligned} P(\mathbf{p}, t) &= 4\pi \int \sum_{n=1}^{N} \sum_{j=1}^{R} C_{nj} e^{\frac{-\alpha_{nl(j)}^2 t}{\tau^2}} j_{l(j)}(\frac{\alpha_{nl(j)} q}{\tau}) Y_j(\mathbf{u}) \sum_{j'=1}^{\infty} (-i)^{l(j')} j_{l(j')}(2\pi qp) Y_{j'}(\mathbf{u}) Y_{j'}(\mathbf{r})\, d^3\mathbf{q} \\ &= 4\pi \sum_{n=1}^{N} \sum_{j=1}^{R} (-1)^{l(j)/2} C_{nj} e^{\frac{-\alpha_{nl(j)}^2 t}{\tau^2}} Y_j(\mathbf{r}) I_{nl(j)}(p), \end{aligned}$$

where we use the orthonormal property of SH, i.e. $\int Y_j(\mathbf{u}) Y_{j'}(\mathbf{u}) d^2\mathbf{u} = \delta_{jj'}$ and define

$$I_{nl(j)}(p) = \int_0^{\infty} q^2 j_{l(j)}(\frac{\alpha_{nl(j)} q}{\tau}) j_{l(j)}(2\pi qp) dq \approx \int_0^{\tau} q^2 j_{l(j)}(\frac{\alpha_{nl(j)} q}{\tau}) j_{l(j)}(2\pi qp) dq \tag{5.10}$$

The integral in (5.10) is solved in **Appendix C**, and we can write the EAP as

$$P(\mathbf{p},t) = 2\tau\sqrt{2\pi^3}\sum_{n=1}^{N}\sum_{j=1}^{R}(-1)^{\frac{l(j)}{2}}C_{nj}e^{\frac{-\alpha_{nl(j)}^2 t}{\tau^2}}Y_j(\mathbf{r})\frac{\sqrt{\alpha_{nl(j)}}J_{l(j)-1/2}(\alpha_{nl(j)})j_{l(j)}(2\pi\tau p)}{\left(4\pi^2p^2-\frac{\alpha_{nl(j)}^2}{\tau^2}\right)} \tag{5.11}$$

The BFOR theoretical solution can be summarized in five steps:

1. $\bigtriangledown^2\psi_i(\mathbf{q}) = -\lambda_i\psi_i(\mathbf{q}), \quad \psi_i(q=\tau,\mathbf{u}) = 0$

2. $E(\mathbf{q},t) = \sum_{i=0}^{\infty} a_i h_i(t)\psi_i(\mathbf{q})$

3. $\bigtriangledown^2 E(\mathbf{q},t) = \frac{\partial E(\mathbf{q},t)}{\partial t}, \quad E(\mathbf{q},t=0) = f(\mathbf{q})$

4. $h_i(t) = e^{-\lambda_i t}; \quad a_i = \langle f(\mathbf{q}), \psi_i(\mathbf{q})\rangle$

5. $P(\mathbf{p},t) = \int E(\mathbf{q},t)e^{-2\pi i\mathbf{q}\cdot\mathbf{p}}d^3\mathbf{q} = 4\pi\sum_{j=1}^{\infty}(-i)^{l(j)}Y_j(\mathbf{r})\left\{\int E(q,\mathbf{u},t)j_{l(j)}(2\pi qp)Y_j(\mathbf{u})d^3\mathbf{q}\right\}$

5.3.1 Rotationally Invariant q-Space Indices

In addition to analytical EAP reconstruction, the DPI, BFOR, and SPFI modeling bases can be used to obtain rotationally invariant q-space indices. Here, we look at three such measures: Po, MSD, and GFA.

$Po = P(\mathbf{p}=0)$ is the probability density that a water molecule remains or returns back to its initial position within the diffusion time [10, 80]. In other words, it indicates the likelihood of a water molecule minimally diffusing during the diffusion time. In a healthy adult brain, Po is greater in white matter (WM) than gray matter (GM) because WM has more restricting barriers including multi-layer myelin sheaths, axonal

membranes, and microtubules. Such restrictivity increases the likelihood of a water molecule returning to or remaining in its initial position, whereas it has a very low probability of returning to its initial position in areas of unrestricted isotropic diffusion (CSF). Hence, Po can be viewed as a measure of restricted diffusion, and for this reason, a reasonable estimation of Po entails using high b-values (i.e. longer diffusion times). Several studies have shown Po to be sensitive to brain pathology, and suggesting that changes in myelin are the primary mechanism for differences in Po[1] [6, 16, 82].

Po can be evaluated either numerically or analytically. The authors in [81] computed Po by numerically summing the normalized diffusion signal $E(\mathbf{q})$ over all diffusion measurements in q-space, and then correcting the sum by the sampling density. Analytical formulations of Po were derived for the SPFI and DPI signal bases [29, 37]. Similarly, an analytical Po expression can be obtained using the BFOR basis, which is derived in **Appendix D**:

$$Po_{BFOR} = 2\sqrt{\pi}\tau^3 \sum_{n=1}^{N} C_{n1} \frac{(-1)^{n+1}}{\alpha_{n0}^2} \tag{5.12}$$

The MSD, which we will denote as $\langle p^2 \rangle$, is simply the second moment of the EAP [80]: $\langle p^2 \rangle = \int p^2 P(\mathbf{p}) d^3\mathbf{p}$. It is related to the MD, which in the case of Gaussian diffusion is given by the well-known Einstein relation $\langle p^2 \rangle = 6(\Delta - \delta/3)\text{MD}$. Thus far, an

[1] Alternatively, if Po is indeed a measure of restricted diffusion, which recall is an intra-axonal phenomenon, then a pathology-induced decrease in the white matter Po could be explained by axonal damage (e.g. "leaky" axons) and/or axonal loss. Given the dearth of clinical studies utilizing Po, it is difficult to say for sure whether myelin loss, axonal loss, or both drive Po reductions.

analytical formulation of the MSD exists only within the DTI framework. It is calculated numerically in q-space imaging, either by extracting the full width at half maximum of the EAP [10] or taking the geometric mean of the diffusion signal over all directions on a HDYI shell [81]. In **Appendix E**, we will show, for the first time, that the general relationship between the MSD and q-space signal is given by

$$\langle p^2 \rangle = \frac{-1}{4\pi^2} \bigtriangledown^2 E(\mathbf{q})|_{\mathbf{q}=0} \tag{5.13}$$

Since DPI assumes $\bigtriangledown^2 E = 0$, it predicts the MSD to be zero: $\langle p^2 \rangle_{DPI} = 0$. The BFOR MSD is (derived in **Appendix E**)

$$\langle p^2 \rangle_{BFOR} = \frac{1}{8\pi^{\frac{5}{2}}\tau^2} \sum_{n=1}^{N} C_{n1}\alpha_{n0}^2 \tag{5.14}$$

Tuch in [72] introduced the concept of GFA and defined it as std(ODF)/rms(ODF). Since ODF is only a feature of the EAP, the subsequent GFA map is derived solely from the angular content of the diffusion profile. Incorporating both the angular and radial contents of the diffusion profile into the definition of GFA will result in a radial dial of GFA maps, illustrating how anisotropy varies with diffusion displacement p. Therefore, we define a new GFA:

$$GFA(p = p_o) = \frac{\text{std}\left[P(p = p_o, \mathbf{r})\right]}{\text{rms}\left[P(p = p_o, \mathbf{r})\right]} \tag{5.15}$$

Another advantage of Eq. (5.15) is that it is better suited for multiple diffusion weighted MR experiments, unlike Tuch's definition, which is single-shell HARDI-based. In order

to capture the 3D anisotropy of the EAP-defined GFA maps, 1000 uniformly distributed vertices on a unit sphere in propagator space (i.e. 1000 values of θ' and ϕ') were acquired using the approach described in [78].

5.4 Materials and Methods

In general, we are given k HARDI shell datasets. The number of encoding directions in each shell does not have to be the same. Each HARDI dataset corresponds to a different b-value. Across all k shells, we have total of M diffusion measurements (including the $b = 0$ measurement). Hence, from these multiple shell datasets, we want to reconstruct the EAP, $P(\mathbf{p})$.

5.4.1 Numerical Implementation of BFOR

The task is to estimate coefficients C_{nj} in Eq. (5.7) from the observed signal $E(q, \mathbf{u}, t = 0)$. We achieve this by carrying out a linear least square (LLS) fitting with regularization in the radial and angular parts. We let $\mathbf{S} = [E(\mathbf{q}_1, t = 0) \dots E(\mathbf{q}_M, t = 0)]^T$ be the M x 1 vector representing the M diffusion signal measurements across all k shells. We also let $\mathbf{C}$ represent the W x 1 vector of unknown expansion coefficients C_{nj}, where $W = \frac{N(L+1)(L+2)}{2}$. Defining $Z_{nj}(q, \mathbf{u}) = j_{l(j)}(\alpha_{nl(j)} q/\tau) Y_j(\mathbf{u})$, we let $\mathbf{Z}$ denote our M x W design matrix:

$$\mathbf{Z} = \begin{pmatrix} Z_{1,1}(q_1, \mathbf{u}_1) & Z_{2,1}(q_1, \mathbf{u}_1) & \cdots & Z_{N,1}(q_1, \mathbf{u}_1) & \cdots & Z_{1,R}(q_1, \mathbf{u}_1) & Z_{2,R}(q_1, \mathbf{u}_1) & \cdots & Z_{N,R}(q_1, \mathbf{u}_1) \\ \vdots & \vdots & \ddots & \vdots & \ddots & \vdots & \vdots & \ddots & \vdots \\ Z_{1,1}(q_M, \mathbf{u}_M) & Z_{2,1}(q_M, \mathbf{u}_M) & \cdots & Z_{N,1}(q_M, \mathbf{u}_M) & \cdots & Z_{1,R}(q_M, \mathbf{u}_M) & Z_{2,R}(q_M, \mathbf{u}_M) & \cdots & Z_{N,R}(q_M, \mathbf{u}_M) \end{pmatrix}$$

Thus, we have a simple linear model of the form $\mathbf{S} = \mathbf{ZC}$. This system of over-determined equations is solved with a regularized LLS solution yielding vector $\widehat{\mathbf{C}}$ given by

$$\widehat{\mathbf{C}} = (\mathbf{Z}^T\mathbf{Z} + \lambda_l\mathbf{L}_{reg} + \lambda_n\mathbf{N}_{reg})^{-1}\mathbf{Z}^T\mathbf{S}, \tag{5.16}$$

where L_{reg} is the Laplace-Beltrami regularization diagonal matrix with $l^2(l+1)^2$ entries on the diagonal and N_{reg} is the regularization diagonal matrix for the radial basis, with entries $n^2(n+1)^2$ on the diagonal. The angular and radial regularization matrices penalize, respectively, high degrees of the angular and radial parts of Eq. (5.7) in the estimation under the assumption that they are likely to capture noise [12]. They also serve to reinforce the positivity contraint of the EAP. λ_l and λ_n are the regularization terms for angular and radial bases, respectively.

5.4.2 Visualization of EAP

Lastly, from the estimated vector $\widehat{\mathbf{C}}$, we can extract the C_{nj} coefficients needed to compute the EAP, Po, MSD, and GFA. The spherical function $P(p, \mathbf{r}, t)$ is the iso-probability profile at some instant of smoothening t for a given p - that is, the probability density that a water molecule, initially at the origin, diffuses a distance p along the direction $\mathbf{r}$. It is computed by generating 800 equidistant points along the equator of a sphere of radius p i.e. the polar angle θ is fixed at $\pi/2$ and the azimuthal angle ϕ is uniformly varied from 0 to 2π. The EAP profile $P(p, \mathbf{r}, t)$ is then interpolated along these 800 points. Thus, the resulting profiles are 2D with the equator perpendicular to the z-axis. It is important to note that in this paper smoothening was applied only to the EAP, itself, and not on the diffusion signal.

5.4.3 Value of τ Parameter

An important point to consider in the implementation is how to determine the parameter τ in the signal basis. In practice, the diffusion signal is bounded by the maximal q-value q_{max} achievable by the imaging system. The authors in [7] have shown that, depending on the length of diffusion time, the amount of signal present at b-values near 30,000 s/mm^2 varies from about half a percent to about five percent, which means that the signal does not approach zero at q_{max} unless the diffusion weighting/diffusion time are very high/long. Thus, we conclude $\tau \geq q_{max}$. Based on numerical simulations, we find the value of τ that best reconstructs the EAP to be $\tau_{optimal} = q_{max} + \Delta q$, where Δq is the (uniform) q-space sampling interval.

5.4.4 Diffusion MRI Data Acquisitions for Synthetic and *In Vivo* Data

The synthetic and *in vivo* datasets use a hybrid, non-Cartesian sampling scheme [80], shown in Table 1. Since EAP reconstruction is sensitive to angular resolution, the number of encoding directions is increased with each shell to increase the angular resolution with the level of diffusion weighting. The number of directions in the outer shells were increased to better characterize complex tissue organization. Diffusion tensor elements for measurements in the second shell were calculated using non-linear least squares estimation with the *Camino* software package [33], which were then used to obtain the FA and principal eigenvector.

Table 5.1: HYDI Encoding Scheme for Synthetic and Human Datasets

Shell	Ne	q (mm^{-1})	Δq (mm^{-1})	b ($\mathrm{s/mm}^2$)
	1	0		0
1st	6	15.2	15.2	375
2nd	21	30.4	15.2	1500
3rd	24	45.6	15.2	3375
4th	24	60.8	15.2	6000
5th	50	76	15.2	9375
	Total=126	q_{max}=76	Mean=15.2	b_{max}=9375

Synthetic Data

The mono-exponential (also referred to as mono-Gaussian) mixture model [73] is frequently used to generate synthetic data to validate a given EAP reconstruction, such as in [12, 29], where the maximum b-value used was 3000 $\mathrm{s/mm}^2$. However, diffusion MR imaging experiments using high b-values (> 2000 $\mathrm{s/mm}^2$) have shown that the diffusion signal decay is no longer mono-exponential. Studies in normal human brain, with b-values over an extended range of up to 6000 $\mathrm{s/mm}^2$, have shown that the signal decay is better described with a bi-exponential i.e. bi-Gaussian curve [31, 56]. Similar findings were made for rat brain, using multiple b-values of up to 10000 $\mathrm{s/mm}^2$ [57]. According to [7], a bi-exponential fit gives very good agreement with the observed water signal attenuation in excised brain tissue from rats for b-values of up to $2 - 3 \times 10^4$ $\mathrm{s/mm}^2$. Thus, BFOR, SPFI, and DPI were applied to simulations of crossing fiber configurations generated by a bi-Gaussian mixture model. Fig. 5.2 illustrates mono-exponential and bi-exponential

decay curves, where the latter has a pronounced tail at high q values, indicating that it takes longer for the signal to decay to zero than under the mono-exponential assumption. The head and tail of the bi-exponential decay curve can be viewed as the fast and slow diffusion components, respectively [31, 52].

In bi-Gaussian mixture,

$$E(q, \mathbf{u}) = \sum_{k=1}^{N_b} [f_{kf} e^{-b\mathbf{u}^T \mathbf{D}_{kf} \mathbf{u}} + f_{ks} e^{-b\mathbf{u}^T \mathbf{D}_{ks} \mathbf{u}}], \tag{5.17}$$

where N_b is the total number of simulated fibers, f_{kf} the volume fraction of the fast component of the k^{th} fiber, and f_{ks} the volume fraction of the slow component. The summation of all volume fractions is 1, i.e., $\sum_{k=1}^{N_b} [f_{kf} + f_{ks}] = 1$. D_{kf} and D_{ks} describe the diffusion tensor for the fast and slow components, respectively, of the k^{th} fiber assuming no exchange between the fast- and slow-diffusion compartments. It should be noted that there is controversy over the assignment of these components and whether the bi-Gaussian model should take into account exchange between compartments [56]. The ground truth of EAP is then

$$P(p, \mathbf{r}) = \sum_{k=1}^{N_b} [\frac{f_{kf}}{\sqrt{(4\pi\epsilon)^3 |\mathbf{D}_{kf}|}} e^{-p^2 \mathbf{r}^T \mathbf{D}_{kf}^{-1} \mathbf{r}/4\epsilon} + \frac{f_{ks}}{\sqrt{(4\pi\epsilon)^3 |\mathbf{D}_{ks}|}} e^{-p^2 \mathbf{r}^T \mathbf{D}_{ks}^{-1} \mathbf{r}/4\epsilon}], \tag{5.18}$$

where $\epsilon = \Delta - \delta/3$. For the synthetic data, the diffusion gradient duration is $\delta = 45$ ms and diffusion gradient separation $\Delta = 56$ ms.

In reconstructing the EAP, we look at two equally weighed fibers crossing at 60°, and set eigenvalues of each diffusion tensor to be [1.6,0.4,0.4]e-3, which gives an FA

value of 0.7071. The values of the fast and slow Gaussian diffusion functions were taken from [52] and are shown in Table 2. Monte Carlo noise simulations were then performed to investiage the effect of SNR on the estimation of Po, MSD, and GFA for a single voxel for each EAP method. Seven SNR levels ([10 20 30 40 50 60 100]) for the $b = 0$ image were simulated, 1000 times each, by adding Rician noise in a similar manner as in [36] for four different scenerios: a fast isotropic component ($D = 0.00115$ mm^2/s); a slow isotropic component ($D = 0.00045$ mm^2/s); fast anisotropic components of a corpus callosum fiber and internal capsule fiber crossing at 60°; and the slow anisotropic components for the previous scenario. The BFOR parameters are $\{L = 4, N = 6, \tau = 91.2$ mm^{-1}, $\lambda_l = 10^{-6}, \lambda_n = 10^{-6}\}$, DPI parameters $\{L = 4, \lambda_l = 0$ (no noise) $/\lambda_l = 0.006$ (with noise)$\}$, and SPFI parameters $\{L = 4, N = 3, \zeta = 500, \lambda_l = 10^{-8}, \lambda_n = 10^{-8}\}$. For each method, model parameters were chosen based on giving the optimal EAP reconstruction when no noise was present.

Human Brain Data

HYDI was performed on a healthy, adult human using a 3.0 T GE-SIGNA scanner with an 8-channel head coil and ASSET parallel imaging. The DW pulse sequence was a single-shot, spin-echo, echo-planar imaging (SS-SE-EPI) with pulse-oximeter gating. The MR parameters were as follows: TE = 122 ms, TR 12 s, FOV = 256 mm, matrix = 128 x 128, voxel size = 2 x 2 mm^2, 30 slices with slice thickness = 3 mm, and a total scan time of about 30 min. Diffusion parameters were maximum b-value $b_{max} = 9375$ s/mm^2, diffusion gradient duration $\delta = 45$ ms, diffusion gradient separation $\Delta = 56$ ms, q-space sampling interval $\Delta q = 15.2$ mm^{-1}, maximum length of the q-space wave vector $q_{max} = 76$ mm^{-1}, field of view of the diffusion displacement space $FOV_p = (1/\Delta q) = 65$

μm, and resolution of the diffusion displacement space $\Delta p = (1/2q_{max}) = 6.6$ μm [23]. The same BFOR, DPI, and SPFI modeling parameters utilized for synthetic data were also used for *in vivo* data.

5.5 Results

BFOR, DPI, and SPFI are first applied to the numerical phantom and then on the real dataset. The numerical phantom is used to validate BFOR, compare its performance to those of DPI and SPFI, assess all three methods' robustness in estimating the scalar measures Po, MSD, and GFA, and answer the following questions: (1) Can these methods properly reconstruct a diffusion signal acquired via hybrid sampling? (2) How does the slow diffusion component affect the EAP reconstruction and the estimations of the scalar quantities? (3) What can be done to reduce the effects of Gibbs ringing on the EAP reconstructions? It is also important to note that the EAP and quantitative scalar measures were reconstructed using only 125 diffusion measurements, while those presented in [37] used 256.

5.5.1 Results of Synthetic Data

Can these methods be used for diffusion signal estimation? Fig. 5.3 displays the BFOR, DPI, and SPFI signal fit for each shell and the corresponding ground truth. The BFOR signal basis fits the diffusion signal nearly perfectly for all shells. Both SPFI and DPI reasonably fit the diffusion signal for $b \geq 1500$ s/mm^2, but poorly reconstruct the inner most shell ($b = 375$ s/mm^2). As expected, DPI also tends to oversmooth the

diffusion signal, especially so at $b = 3375$, 6000 s/mm^2. Results of DPI signal fitting were also reported in [37], where unform sampling along four spherical shells ($b = 2000$, 4000, 6000, and 8000 s/mm^2) was done. Although a hybrid sampling scheme is used here, our results are consistent with those of [37] for $b \geq 1500$ s/mm^2. SPFI's and DPI's poor signal fit of the diffusion signal in inner most shell may be due to the fact that only six measurements were acquired in this shell (see Table 1), which may be inadequate for their respective radial bases.

Performances of BFOR, DPI, and SPFI in reconstructing EAP. Fig. 5.4 shows the EAP reconstruction for the fast diffusion component across propagator space using each method. Modeling the fast component (i.e. head of the bi-exponential in Fig. 5.2) is tantamount to fitting a mono-exponential curve, and so the EAP reconstruction for the fast diffusion component can be viewed as if the diffusion signal decay was mono-exponential. Both BFOR and SPFI model the fast component EAP very well, accurately capturing the geometry and orientation of the EAP profile, and the BFOR reconstruction is nearly identical to that of SPFI. DPI performs reasonably well, but tends to overestimate the EAP.

Fig. 5.5 shows the EAP reconstruction for the slow diffusion component, which can be viewed as modeling the tail of the bi-exponential curve in Fig. 5.2. Note that the BFOR and SPFI reconstructions are quite alike. At $p = 1$ μm, all three methods capture the correct geometry of the ground truth EAP profile, but underestimate it, DPI more so. At $p = 5$ μm, all three methods are unsuccessful in capturing the correct geometry, in particular failing to capture the peaks of the ground truth EAP profile. However, they do capture the correct orientation. At $p = 10$ and especially $p = 15$ μm, the BFOR and SPFI EAP reconstructions of the slow diffusion component begin to suffer from

Gibbs ringing, which arise from the truncation of the signal bases at high q. The DPI reconstruction at $p = 15$ μm benefits from the inherent smoothening of Laplacian signal modeling, with no spurious peaks present. Although oversmoothened and overestimated, it does a much better job than BFOR and SPFI in resolving the correct fiber orientation at $p = 15$ μm. The difficulty in reconstructing the EAP for the slow diffusion component is due to the slow diffusion component being sensitive to truncation effects. The reality of finite sampling makes it challenging to capture the tail of the bi-exponential curve. How then should one combat the effects of truncation artifacts?

Signal Extrapolation. Extrapolating the diffusion signal to higher q-values so that q-space is more thoroughly explored could mitigate the truncation effects. Signal extrapolation can increase the spatial resolution of the EAP [32], and in the case of DSI, significantly reduce the cumbersome q-space sampling [84]. By linearly damping the signal measurments in the outermost shell ($b = 9375$ shell), we were able to (linearly) extrapolate samples onto three new 'pseudo-shells.' Specifically, the outermost signal measurements were attenuated by a factor of 0.7, 0.4, and 0.1 to form the three 'pseudo-shells.' The BFOR and SPFI scaling factors, τ and ζ, respectively, were changed for the extrapolation to $\tau = 136.8$ mm^{-1} and $\zeta = 1100$. Note that the q-space sampling interval Δq was not changed for the extrapolation.

Fig. 5.6 shows that signal extrapolation improves the reconstruction of the slow EAP component for both BFOR and SPFI. At $p = 10$ μm, the BFOR and SPFI slow EAP reconstructions with signal extrapolation, although not perfectly capturing the ground truth geometry, better capture the angular features of the ground truth than those without signal extrapolation. The biggest improvement, however, is seen at $p = 15$ μm, where the pronounced Gibbs ringing is greatly reduced by the signal extrapolation. In

particular, the BFOR and SPFI slow EAP reconstructions with signal extrapolation at $p = 15$ μm are not spiky and much closer to the ground truth, although their orientations are slightly off, than those without extrapolation (Fig. 5.5). Note that both the BFOR and SPFI slow EAP reconstructions with extrapolation are quite alike. The BFOR fast EAP reconstruction was not affected by extrapolation, being nearly idential to its counterpart without extrapolation. However, the SPFI fast EAP reconstruction with extrapolation was moderately less acurate than that without extrapolation. In general, signal extrapolation can significantly improve EAP reconstructions at larger diffusion displacements (i.e. $p = 15$ μm).

Estimation of q-space indices. Fig. 5.7 shows the results for the Po measurements. Without signal extrapolation, BFOR and SPFI asymptotically approach the ground truth fast anisotropic Po, whereas DPI overestimates it. All three methods, without signal extrapolation, severely underestimate slow anisotropic Po, which is due to the truncation of the signal bases at high q. Both BFOR and SPFI asymptotically approach the ground truth fast/slow isotropic Po, while DPI overestimates both. At low levels of SNR (e.g. 10 & 20), which is quite common in diffusion MRI, all three methods (without signal extrap.) have biased estimates of Po, though the variance is fairly small.

When signal extrapolation is applied, the estimation of the slow anisotropic Po by BFOR and SPFI significantly improves, as shown in Fig. 5.7b. According to Fig. 5.7a, signal extrapolation does not asymptotically affect SPFI's estimation of fast anisotropic Po, but slightly worsens that of BFOR's. At low levels of SNR, however, signal extrapolation results in more severe overestimation of fast anisotropic Po than without signal extrapolation for both BFOR and SPFI.

Fig. 5.8 shows the results for the MSD measurements. BFOR estimates both the fast and slow anisotropic/isotropic MSD very well across SNR levels. However, at low levels of SNR, the variability (given by the standard deviation) of the BFOR estimation of MSD is quite large, indicating strong sensitivity to noise. SPFI without signal extrapolation severely underestimates anisotropic MSD, giving negative values for slow anisotropic MSD, which indicates that it will give inaccurate measurements of the MSD of WM. SPFI also underestimates fast isotropic MSD, but asymptotically approaches ground truth slow isotropic MSD. Interestingly, there is less variability in SPFI's estimation of MSD than BFOR.

When signal extrapolation is applied to the MSD measurements, SPFI's estimations of slow anisotropic and slow isotropic MSD significantly improve, well-estimating them across SNR levels, as shown in Figs. 5.8b and 5.8d, respectively. Specifically, the SPFI slow anisotropic MSD estimation is no longer negative with signal extrapolation. BFOR's estimations of slow anisotropic and slow isotropic MSD with extrapolation are nearly identical to those without it. However, the variability of the BFOR and SPFI MSD measurements is much less than those without extrapolation. A negative consequence of signal extrapolation is that it increases the inaccuracy (i.e. asymptotically worsening) of the BFOR/SPFI fast anisotropic and fast isotropic MSD estimations, all of which are greatly underestimated. The simulations indicate signal extrapolation may be more beneficial to SPFI's estimation of MSD than that of BFOR's.

Fig. 5.9 shows the results for the GFA measurements. Asymptotically, BFOR and SPFI without signal extrapolation approach the ground truth fast anisotropic GFA, while DPI underestimates it. Across SNR levels, DPI severely underestimates slow anisotropic GFA, while both BFOR and SPFI greatly overestimate it. For the case of isotropic

diffusion, where GFA=0, the GFA estimated by each method approaches zero at high SNR. However, at SNR=10, both SPFI and BFOR severely overestimate the isotropic GFA, giving values comparable to the GFA of WM. DPI's estimation of the isotropic component is more robust to noise than BFOR and SPFI.

SPFI with signal extrapolation still overestimates slow anisotropic GFA, though slightly less so than without it, but the extrapolation increases the estimation's variability at the same time. Signal extrapolation has negligible effects on BFOR's estimation of slow anisotropic GFA. Both BFOR's and SPFI's estimation of fast anisotropic GFA are not asymptotically affected by signal extrapolation, having similar convergences as those without signal extrapolation, but the extrapolation causes both methods to overestimate fast anisotropic GFA to a larger degree at SNR=10, 20, & 30 than without it. Based on Fig. 5.9c, both SPFI and BFOR with signal extrapolation overestimate isotropic GFA, across SNR levels, to a larger extent than without extrapolation, implying that extrapolation is quite sensitive to noise in CSF regions.

5.5.2 Results of Human Brain Data

Resolving single fibers. In Fig. 5.10, a 4×4 ROI was drawn on the splenium of corpus callosum. The EAP profiles reconstructed at $p = 10$ μm by each method have the fundamental peanut shape of a single fiber. Note that the BFOR and SPFI reconstructions in both cases are very similar. We see that application of smoothing $t = 550$ removes the center peaks of the BFOR EAP profiles. Whether these center peaks in the EAP profiles are the result of Gibbs ringing (i.e. artifical peaks) or describe some underlying biological process is an open question.

Resolving crossing fibers. In Fig. 5.11, a 4×9 ROI was drawn in a region of fiber crossing, where the EAP profiles were reconstructed at $p = 10$ μm. Although not identical, the BFOR and SPFI reconstructions are quite similar, and they recover and well discriminate crossing fiber configurations in the EAP. DPI, however, tends to oversmooth the EAP profiles of crossing WM fibers, resulting in spherical/oblate shapes that give the impression of isotropic diffusion. Based on Fig. 5.11d, the application of smoothing $t = 60$ to BFOR removes the center peaks from several voxels, but at the expense of slight angular smoothening of EAP profiles themselves.

Fig. 5.12 shows the reconstructed EAP profiles for the same crossing fiber region, but at $p = 15$ μm. Fiber crossing configurations are recovered and well discriminated in the EAP for each method. Unlike at $p = 10$ μm, the DPI EAP reconstruction at $p = 15$ μm is sharper and does not suffer from oversmoothening. In fact, as the propagator radius p increases, the angular resolution improves, at the enpense of the EAP profiles becoming spiky, as is evident in Figs. 5.12a, 5.12e, and 5.12g. When a smoothing of $t = 60$ is applied to the BFOR EAP reconstruction (without signal extrapolation), the subsequent EAP profiles are still spiky. At $t = 350$, the spikiness is smoothed out, but many of the WM voxels have EAP reconstructions significantly differing, with respect to orientation and geometry, from those at $t = 0$. Figs. 5.12d and 5.12f show the BFOR and SPFI EAP profiles reconstructed at $p = 15$ μm with signal extrapolation, respectively, which are much less spiky than the corresponding ones without signal extrapolation, which is consistent with the synthetic results shown in Fig. 5.6. The signal extrapolation also smoothes the reconstructed EAP profiles, but unlike BFOR at $t = 350$, none of the WM voxels are oversmoothed to such a degree that their EAP profiles have oblate shapes. Unlike BFOR at $t = 350$, the underlying EAP geometry and orientation of the BFOR/SPFI reconstructions with signal extrapolation are fairly consistent to those

without extrapolation (at $t = 0$). As observed at $p = 10$ μm, the BFOR and SPFI EAP reconstructions at $p = 15$ μm are quite similar, which is consistent with the synthetic data results.

Q-space Indices. Table 5.3 shows the mean index value and corresponding standard deviation for genu and splenium of corpus callosum (WM) and putamen (GM). Three 4×4 ROIs were drawn on both the genu and splenium and one such ROI on both the left and right putamen, across several slices. The table shows that the SPFI MSD (without signal extrapolation) erroneously gives negative values for the MSD of genu and splenium. With extrapolation, the SPFI MSD of genu and splenium are positive.

Based on the numerical simulations, signal extrapolation was applied to both BFOR's and SPFI's estimation of Po. Fig. 5.13 displays an axial slice of Po generated by each method. In the first row, we show Po computed from BFOR, SPFI, DPI, and numerically [81]. The BFOR, SPFI, and numerical Po maps are quite similar, exhibiting rich GM/WM and tissue/CSF contrasts while the DPI Po map has less GM/WM contrast. In particular, based on Table 5.3, the Po ratio of WM to GM is slightly above 2 for BFOR and SPFI, while less than 2 for DPI.

The MSD maps computed from BFOR, SPFI, DPI, and numerically [81] are shown in Fig. 5.14. Both the BFOR and numerical MSD maps exhibit rich tissue/CSF contrast, but have little WM/GM contrast, which is similar to the DTI MD. Table 5.3 shows that the BFOR MSD values for WM and GM are quite similar. In the SPFI (without signal extrapolation) MSD map, WM regions are completely dark, having negative MSD values. This is consistent with the results of the noise simulations, which showed that SPFI severely underestimates the MSD of WM. Signal extrapolation has the effect of

enforcing the positivity constraint on the MSD for SPFI. However, both the BFOR and SPFI MSD maps with signal extrapolation have poor tissue/CSF contrast because of the noise induced by the signal extrapolation. With regards to BFOR, both the synthetic and *in vivo* data suggest that it's best not to use signal extrapolation in estimating MSD. SPFI, however, does not generate reliable MSD maps either with or without signal extrapolation. Although DPI predicts the MSD to be zero, an MSD map was computed for it by numerically estimating the second moment of the diffusion propagator. The constrast of the MSD DPI map is completely inverted, with WM appearing bright and CSF dark.

Fig. 5.16 displays axial slices of the GFA computed at $p = 5$, 10, and 15 μm for each method, illustrating how the anisotropy of different WM regions, such as the corpus callosum and capsules, varies with diffusion displacement p. According to Table 5.3, at $p = 5$ μm, the anisotropy of corpus callosum is lower with respect to levels seen in DTI. At $p = 10$ μm, the corpus callosum is very anisotropic, as can be seen from Table 5.3, indicating that $p = 10$ μm is a diffusion displacement worth reconstructing the EAP at. The GFA at $p = 15$ μm is more noisy, which is due to truncation of signal basis at high q-values and 15 μm being well beyond the resolvable resolution (of diffusion displacement) limit. The BFOR and SPFI GFA maps without signal extrapolation are very similar, while WM regions in the DPI computed GFA maps at $p = 5$ and 10 μm have lower intensity than those of BFOR and SPFI, which is consistent with the underestimation of GFA(10) by DPI observed in the Monte Carlo noise simulations (Fig. 5.9). CSF regions in the BFOR GFA(10) map with signal extrapolation are more noisy than without it, which is consistent with the simulation results shown in Fig. 5.9c. In the case of SPFI, however, the noise level is very severe in CSF regions in the GFA(5) & GFA(10) maps with signal extrapolation than those without it.

5.6 Discussion

The three analytical EAP reconstruction schemes examined in this paper possess both certain advantages and disadvantages. Among the three, the DPI reconstruction uses the least number of expansion coefficients. According to both synthetic and *in vivo* data, DPI tends to greatly oversmoothen the EAP, especially at $p = 10$ μm, but performs well at $p = 15$ μm where it did not make use of signal extrapolation. DPI's assumption of Laplacian signal modeling, however, entails that the MSD is zero (refer to Eq. (5.13)). Fig. 5.9 indicates that DPI greatly underestimates GFA(10), which is reflected in Fig. 5.16 and Table 5.3. In addition, the DPI signal basis is only applicable at $q > 0$, which is unrealistic since the diffusion signal is defined at $q = 0$.

The SPFI signal basis possesses several advantages in that it radially decays to zero and has no singularity at $q = 0$. In addition, the EAP is derived via integration over the entire q-space, unlike BFOR and DPI, where the q-space integration is up to a certain bound that is related to q_{max}. Interestingly, however, the SPFI EAP reconstructions for both synthetic and real datasets are quite similar to those of BFOR, suggesting the two methods may be inherently related. According to the synthetic data, signal extrapolation greatly improves the SPFI EAP reconstruction at $p = 15$ μm. Although not shown in this paper, heat diffusion smoothening can be applied to SPFI. SPFI's estimation of Po and GFA, either with or without signal extrapolation, is quite comparable to those of BFOR's. However, it poorly estimates the MSD, which recalling Eq. (5.13), may be due to, from a computational standpoint, SPFI's signal basis not being an eigenfucntion of the Laplacian operator.

The main limitation of the BFOR signal model, as mentioned in the **Theory** sec-

tion, is that it infinitely oscillates about zero, which entails a finite integration of the signal over q-space (τ being the upperbound) to retrieve the EAP. However, based on Fig. 5.3, BFOR outperforms DPI and SPFI in modeling the diffusion signal. Heat diffusion smoothening helps in removing potentially spurious peaks, and signal extrapolation significantly improves the EAP reconstruction at $p = 15$ μm. According to both the synthetic and real data, BFOR gives reasonable estimates of all three q-space indices.

The slow component of diffusion is the most sensitive to truncation artificats, which can induce severe Gibbs ringing and adversely affect the orientation of reconstructed EAP. In this paper, signal extrapolation was proposed as a means to mitigate the effects of such artifacts, and was oberseved to be most effective at higher radii (i.e. $p = 15$ μm), where the effects of signal truncation artifacts are most pronounced. The significant improvement in the BFOR/SPFI EAP reconstruction at $p = 15$ μm via linear signal extrapolation hence suggests that extrapolation may be a useful preprocessing step for EAP reconstruction at large diffusion diplacements. Signal extrapolation also greatly improves the accuracy of the BFOR/SPFI Po estimation, according to the synthetic data. However, signal extrapolation increases the severity of noise in CSF regions in the GFA and MSD maps for both BFOR & SPFI, as evidenced by the synthetic and real datasets, reducing tissue/CSF contrast. Hence, extrapolation may not be desirable for GFA and MSD estimation. Future work includes optimizing the signal extrapolation for a given signal basis.

The degree of heat diffusion smoothing desired depends on the propagator radius and whether the fibers are single or crossing. Based on Fig. 5.10, a smoothing of $t = 550$ was applied to splenium at $p = 10$ μm to remove the center peaks. However, for a crossing fiber region at $p = 10$ μm, a smoothing of $t = 60$ was only applied because

the EAP profiles of crossing fibers can easily become oversmoothed, resulting in oblate shapes. The fact that the smoothing factor is different for different brain regions poises a problem for whole brain EAP processing. One way to address this issue is to use an optimal bandwidth selection framework from statistics to estimate the optimal t. Specifically, the bandwidth t is selected to minimize a certain cost function. In a spline setting, the cost function will be a generalized cross-validation (GCV) criterion [48]. In a more simple setting like ours, we can choose the t that minimizes the sum of the squared residuals, where the residual is simply the difference between the actual data and model fit.

Although the encoding scheme in this study consisted of equally spaced concentric spherical shells, the BFOR framework does not require such a scheme. BFOR only requires a minimum of two diffusion weightings and use of a spherical coordinate system. Random sampling along q-space or even the use of unequally spaced concentric shells is perfectly valid. This, however, leads to the important question of what is the best way to sample N diffusion measurements in q-space, which have started to be addressed [13, 26, 54]. Future work includes optimizing the q-space sampling and applying compressed sensing to BFOR.

Both the ODF and EAP profiles are not sharp enough to extract the true fiber orientation. Rather, the fiber orientation is given by the fiber orientation distribution function (fODF), which can be computed via spherical deconvolution of some assumed kernel (i.e. response function) from q-space diffusion signal [70]. Mathematically, the

angular convolution is given by

$$E(q, \mathbf{u}) = \int_{S^2} F(\mathbf{r}) K(q, \mathbf{u}, \mathbf{r}) d^2\mathbf{r}, \tag{5.19}$$

where $F(\mathbf{r})$ is the fODF and K the kernel. The derivation of the fODF using the BFOR, SPFI, and DPI signal bases is worth exploring in the future.

In any future clinical study employing HYDI to examine brain pathology, where rotationally invariant indices like GFA and Po can be used to assess changes between diseased and normal subjects, voxel-wise analysis is desired. However, spatial normalization of multiple b-value datasets is no easy task. Recently, the authors in [39] proposed a registration algorithm to align HARDI datasets using the ODFs. Specifically, the algorithm seeks an optimal diffeomorphism of large deformation between two ODF fields across a spatial volume domain and at the same time, locally reorients an ODF in a manner consistent with the underlying anatomical structure. HYDI images could be aligned using the same algorithm, except replacing the ODF with the EAP.

The MSD measure is quite sensitive to noise [8, 80]. The authors in [81] proposed an alternative measure to MSD called the q-space inverse variance (QIV), which is a pseudo-diffusivity measure. Mathematically, the QIV is defined as

$$QIV = \left[\int q^2 E(\mathbf{q}) d^3\mathbf{q} \right]^{-1} \tag{5.20}$$

The QIV can thus be interpreted as the inverse of the "variance" of q (i.e. $QIV = 1/\langle q^2 \rangle$). It is not a real variance in the statistical sense because $E(\mathbf{q})$ does not constitute a

probability density function. The QIV is not an arbitrary meausre, but related to the EAP in a manner analogous to which the MSD is related to the diffusion signal - in **Appendix F**, we will show that

$$QIV^{-1} = \frac{-\bigtriangledown^2 P(\mathbf{p})|_{\mathbf{p}=0}}{4\pi^2} \tag{5.21}$$

Comparing Eq. (5.21) to (5.13), we can see that the QIV and MSD are Fourier complements of each other (i.e. inverse pairs), which is a consequence of the Fourier relationship between the EAP and q-space signal. The QIV within the BFOR framework is (see **Appendix F** for derivation)

$$QIV_{BFOR} = \frac{1}{2\sqrt{\pi}\tau^5 \sum_{n=1}^{N}(-1)^n C_{n1} \frac{(6-\alpha_{n0}^2)}{\alpha_{n0}^4}} \tag{5.22}$$

Fig. 5.15 displays an axial slice of the BFOR QIV, illusrating rich tissue/CSF contrast. The tissue/CSF contrast in the QIV is more enhanced than that of the MSD, and unlike the MSD, the QIV map also exhibits WM/GM contrast (the right and left putamen are visible in Fig. 5.15 but not in the MSD maps). According to Table 5.3, the QIV of the corpus callosum is about a third of that of the putamen.

5.7 Conclusion

We have introduced a new orthonormal basis to model the q-space diffusion signal and from which the EAP can be analytically reconstructed using hybrid, non-Cartesian

Table 5.2: Fast/Slow Diffusion ADCs & Component Size Fractions (from [52])

Region of Interest	Corpus Callosum	Internal Capsule
ADC_f ($\mu m^2/ms$)	1.176	1.201
ADC_s ($\mu m^2/ms$)	0.195	0.176
f_f	0.699	0.643
f_s	0.301	0.357

sampling with multiple q-shell measurements. BFOR is a linear and efficient reconstruction based on heat equation estimation of the diffusion signal. Compared to DSI, BFOR employs much fewer diffusion measurements. Rotationally invariant q-space indices such as GFA, Po, and MSD can then be obtained using the derived EAP.

5.8 Acknowledgments

The authors are thankful to Cheng Guan Koay and Steve Kecskemeti of the University of Wisconsin-Madison for insightful discussions on the estimation of the diffusion propagator.

Table 5.3: Values of Indices for Various WM & GM Structures

Index	Splenium	Genu	Putamen
BFOR GFA(5)	0.212±0.0162	0.188±0.0153	0.0353±0.0130
BFOR GFA(5) Extrap	0.416±0.0310	0.370±0.0325	0.0879±0.0296
SPFI GFA(5)	0.234±0.0178	0.209±0.0179	0.0424±0.0152
SPFI GFA(5) Extrap	0.461±0.0342	0.402±0.0387	0.103±0.0342
DPI GFA(5)	0.129±0.00849	0.111±0.0103	0.0166±0.00642
BFOR GFA(10)	0.998±0.00310	0.991±0.0184	0.254±0.0686
BFOR GFA(10) Extrap	0.999±0.00270	0.991±0.0187	0.360±0.0759
SPFI GFA(10)	0.999±0.00246	0.994±0.0156	0.263±0.0735
SPFI GFA(10) Extrap	0.996±0.00535	0.988±0.0243	0.339±0.0722
DPI GFA(10)	0.831±0.0280	0.766±0.0533	0.123±0.0380
BFOR GFA(15)	0.927±0.0424	0.857±0.0736	0.397±0.0830
BFOR GFA(15) Extrap	0.859±0.0782	0.753±0.104	0.349±0.0737
SPFI GFA(15)	0.957±0.0346	0.875±0.0849	0.380±0.0797
SPFI GFA(15) Extrap	0.858±0.0838	0.730±0.104	0.318±0.0722
DPI GFA(15)	0.952±0.0253	0.906±0.0566	0.286±0.0682
BFOR MSD (10^{-3} mm^2)	0.207±0.0860	0.219±0.0980	0.211±0.0820
BFOR MSD Extrap (10^{-3} mm^2)	0.137±0.0300	0.162±0.0330	0.158±0.0160
SPFI MSD (10^{-3} mm^2)	-0.0670±0.0770	-0.0220±0.0950	0.0700±0.0510
SPFI MSD Extrap (10^{-3} mm^2)	0.0830±0.0210	0.103±0.0210	0.137±0.0150
DPI MSD (10^{-3} mm^2)	4.60±0.430	4.27±0.460	4.28±0.361
BFOR *Po* (10^5 mm^{-3})	6.63±0.729	5.65±0.630	2.95±0.263
BFOR *Po* Extrap (10^5 mm^{-3})	10.8±1.17	9.24±1.07	4.41±0.396
SPFI *Po* (10^5 mm^{-3})	7.00±0.757	6.06±0.649	3.12±0.258
SPFI *Po* Extrap (10^5 mm^{-3})	11.2±1.33	9.37±1.22	4.33±0.449
DPI *Po* (10^5 mm^{-3})	5.00±0.514	4.38±0.435	2.99±0.231
BFOR QIV (10^{-10} mm^5)	4.04±0.447	4.78±0.563	11.1±1.28

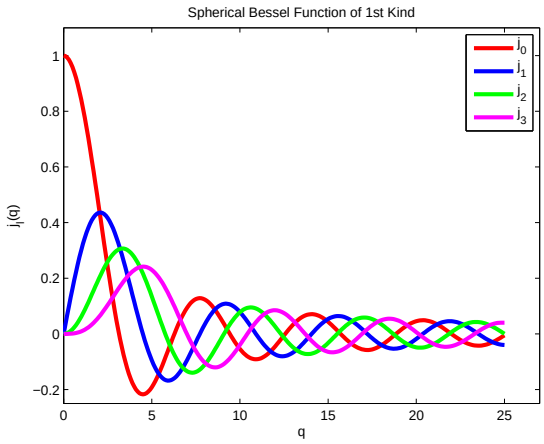

Figure 5.1: Plots of spherical Bessel functions of first kind, which form the radial basis of the BFOR signal solution, for different orders l. As q approaches infinity, they infinitely oscillate about zero.

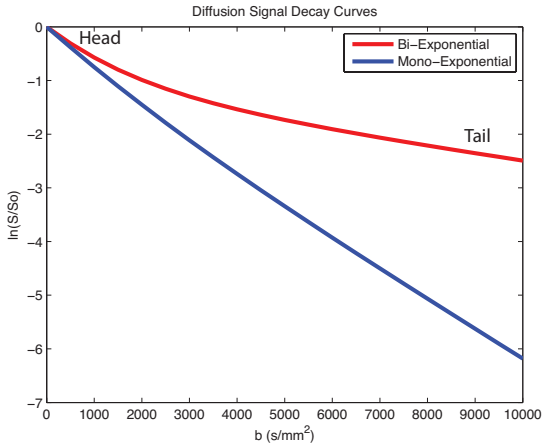

Figure 5.2: Plots of diffuison signal attenuation as a function of b-value illustrating mono-exponential and bi-exponential decays. The tail of the bi-exponential can be interpreted as the slow diffusion component, while the head the fast diffusion component.

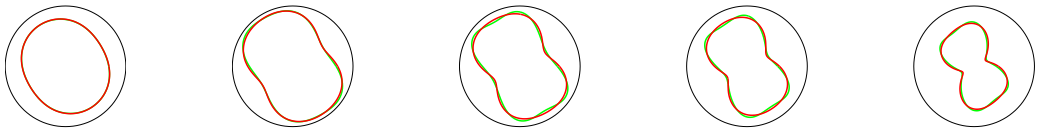

(a) b=375 (b) b=1500 (c) b=3375 (d) b=6000 (e) b=9375

BFOR Signal Fit

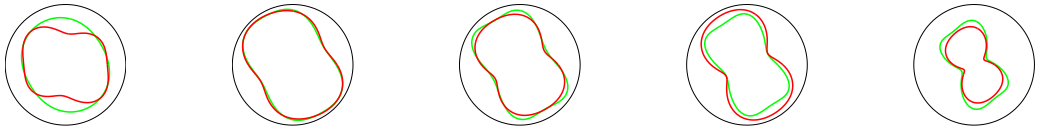

(f) b=375 (g) b=1500 (h) b=3375 (i) b=6000 (j) b=9375

SPFI Signal Fit

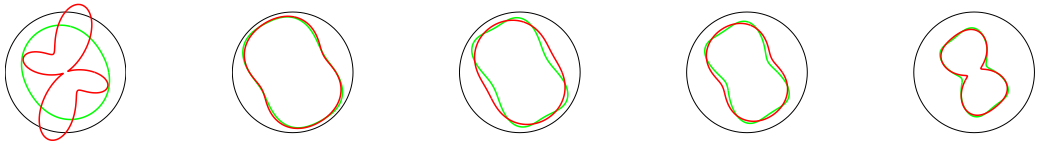

(k) b=375 (l) b=1500 (m) b=3375 (n) b=6000 (o) b=9375

DPI Signal Fit

Figure 5.3: The ground truth diffusion signal (green) and estimated signal (red) using BFOR, SPFI, and DPI when noise was absent. Two equally weighted WM fibers were simulated crossing at 60°. Measurements from all 5 shells were used.

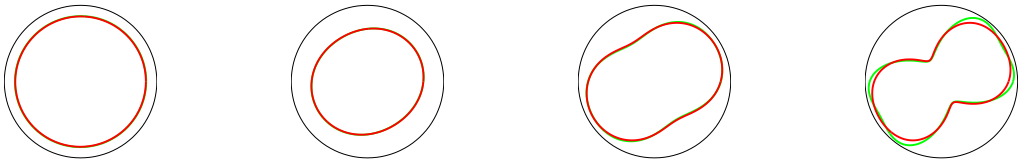

(a) p=1 μm (b) p=5 μm (c) p=10 μm (d) p=15 μm

BFOR Fast EAP reconstruction at $t = 0$

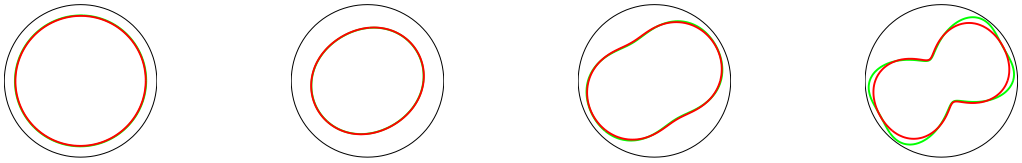

(e) p=1 μm (f) p=5 μm (g) p=10 μm (h) p=15 μm

SPFI Fast EAP Reconstruction

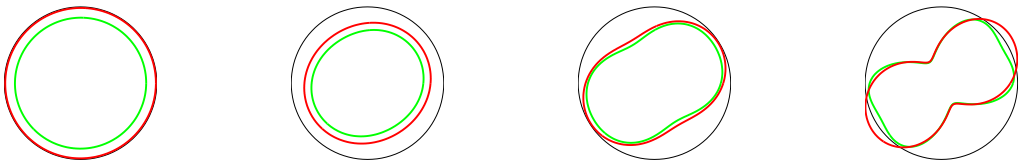

(i) p=1 μm (j) p=5 μm (k) p=10 μm (l) p=15 μm

DPI Fast EAP Reconstruction

Figure 5.4: Reconstruction of the fast component EAP (red) using BFOR, SPFI, and DPI compared with the ground truth (green). Two equally weighted WM fibers were simulated crossing at 60°.

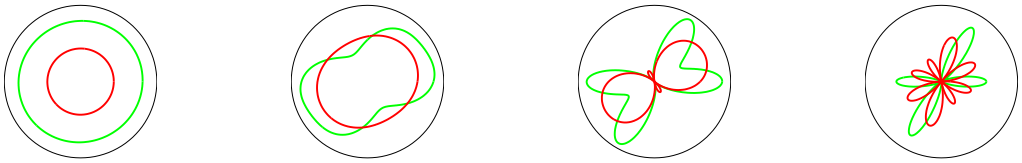

(a) p=1 μm (b) p=5 μm (c) p=10 μm (d) p=15 μm

BFOR Slow EAP Reconstruction at $t = 0$

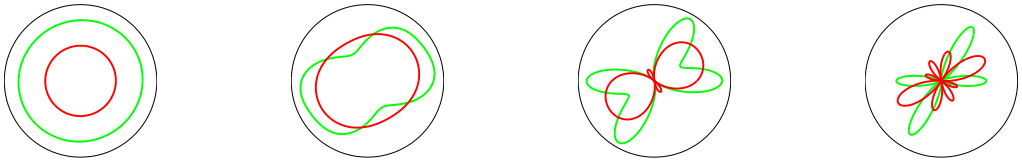

(e) p=1 μm (f) p=5 μm (g) p=10 μm (h) p=15 μm

SPFI Slow EAP Reconstruction

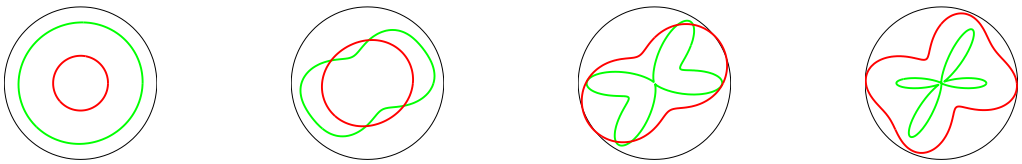

(i) p=1 μm (j) p=5 μm (k) p=10 μm (l) p=15 μm

DPI Slow EAP Reconstruction

Figure 5.5: Reconstruction of the slow component EAP (red) using BFOR, SPFI, and DPI compared with the ground truth (green). Two equally weighted WM fibers were simulated crossing at 60°.

(a) p=1 μm (b) p=5 μm (c) p=10 μm (d) p=15 μm

BFOR Fast EAP Reconstruction at $t = 0$ with Linear Extrapolation

(e) p=1 μm (f) p=5 μm (g) p=10 μm (h) p=15 μm

SPFI Fast EAP Reconstruction with Linear Extrapolation

Figure 5.6: Continues to next page.

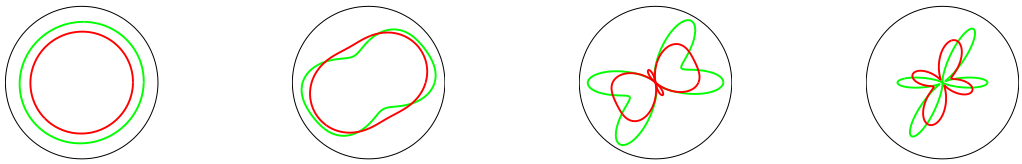

(i) p=1 μm (j) p=5 μm (k) p=10 μm (l) p=15 μm

BFOR Slow EAP Reconstruction at $t = 0$ with Linear Extrapolation

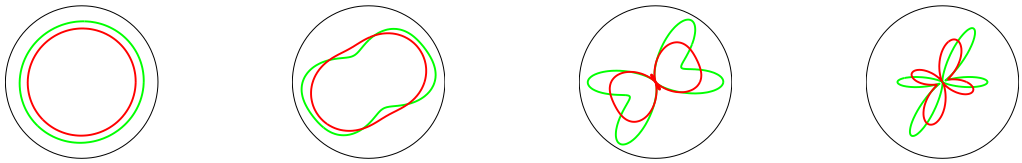

(m) p=1 μm (n) p=5 μm (o) p=10 μm (p) p=15 μm

SPFI Slow EAP Reconstruction with Linear Extrapolation

Figure 5.6: Extrapolated samples were acquired by linearly damping the signal measurements in the outermost shell. Reconstruction of the EAP (red) using BFOR and SPFI compared with the ground truth (green). Two equally weighted WM fibers were simulated crossing at 60°.

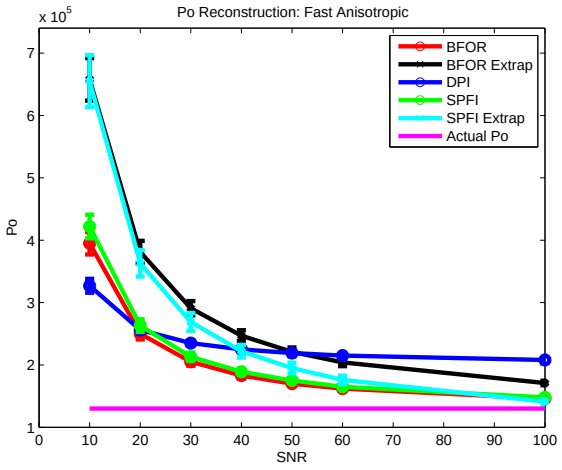

(a) Fast Anisotropic *Po*

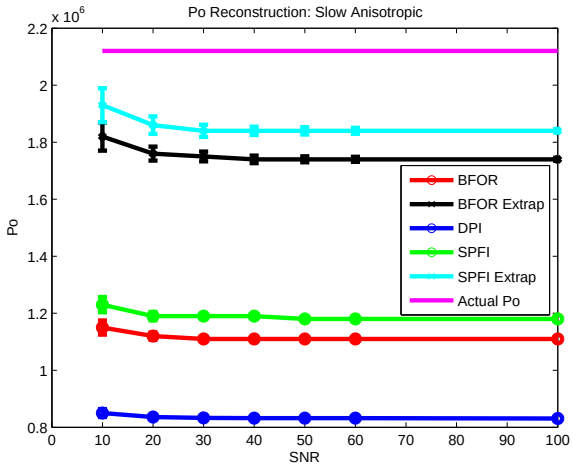

(b) Slow Anisotropic *Po*

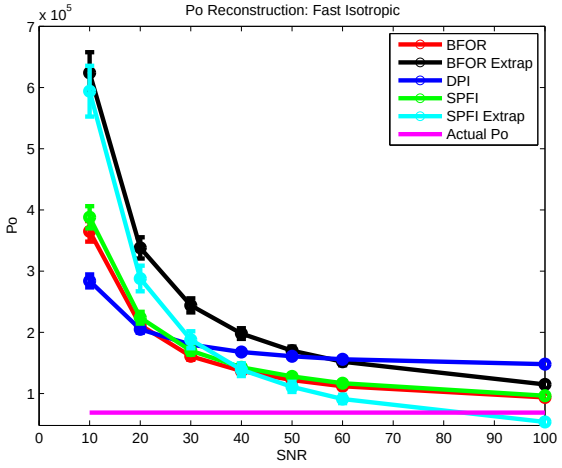

(c) Fast Isotropic *Po*

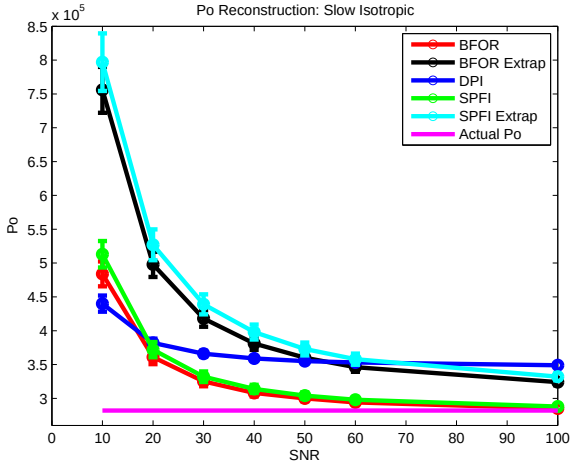

(d) Slow Isotropic *Po*

Figure 5.7: Monte Carlo simulation investigating the effect of noise on estimation of *Po* using fast/slow anisotropic components and fast/slow isotropic components. Error bars denote one standard deviation across 1000 trials.

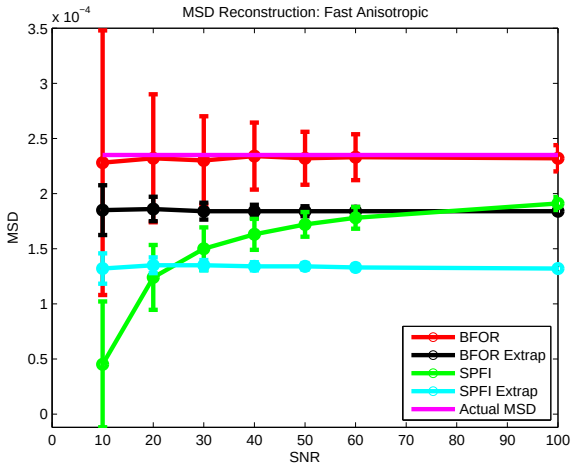

(a) Fast Anisotropic MSD

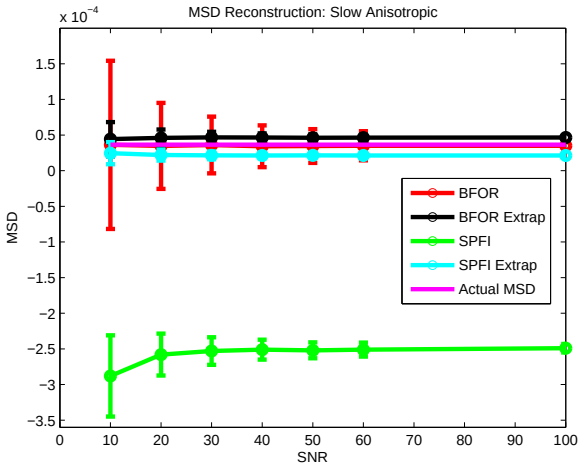

(b) Slow Anisotropic MSD

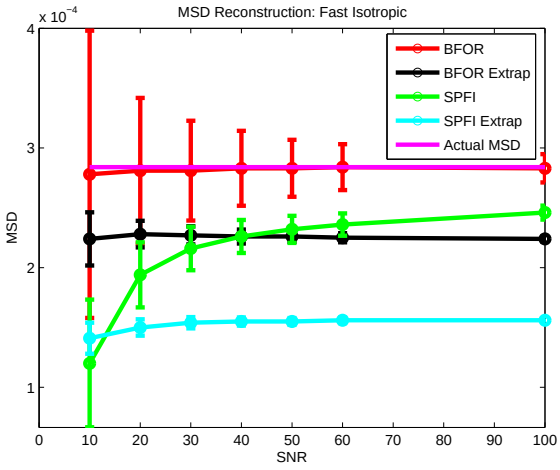

(c) Fast Isotropic MSD

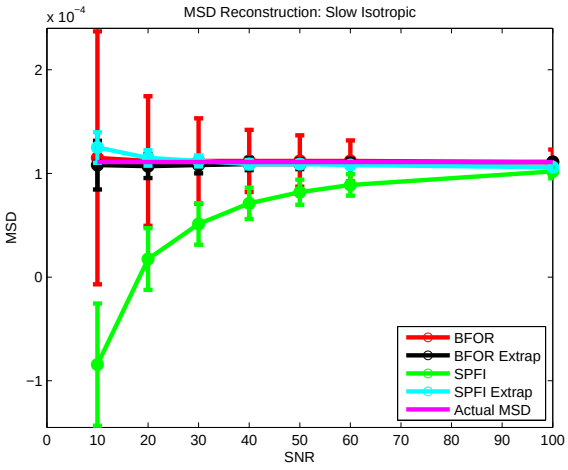

(d) Slow Isotropic MSD

Figure 5.8: Monte Carlo simulation investigating the effect of noise on estimation of MSD using fast/slow anisotropic components and fast/slow isotropic components. Error bars denote one standard deviation across 1000 trials.

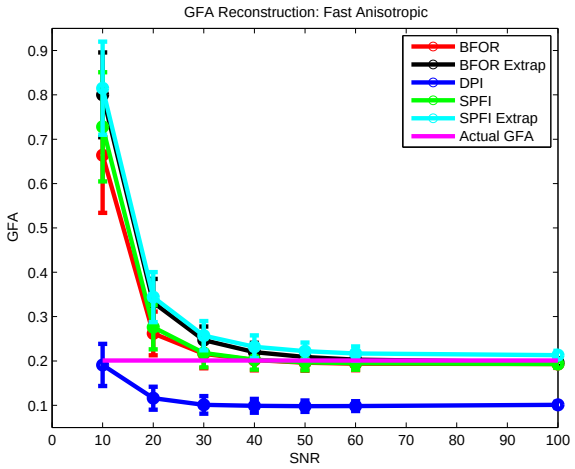

(a) Fast Anisotropic GFA

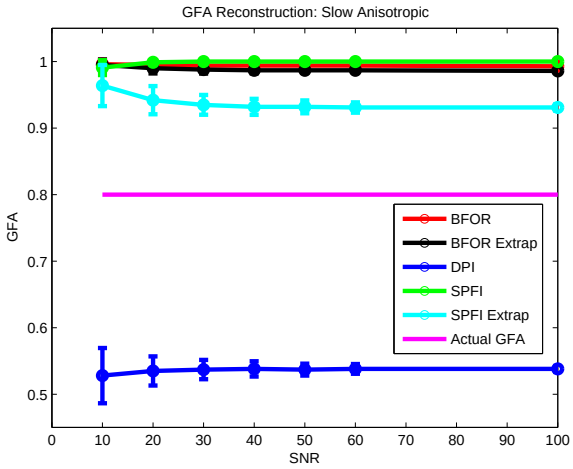

(b) Slow Anisotropic GFA

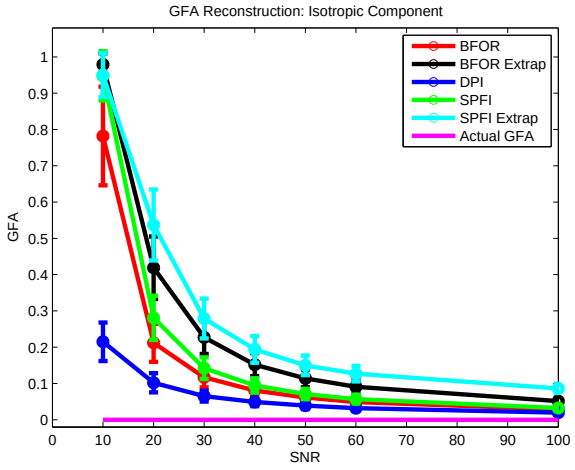

(c) Isotropic GFA

Figure 5.9: Monte Carlo simulation investigating the effect of noise on estimation of GFA using fast/slow anisotropic components and an isotropic component. GFA was computed at $p = 10$ μm. Error bars denote one standard deviation across 1000 trials.

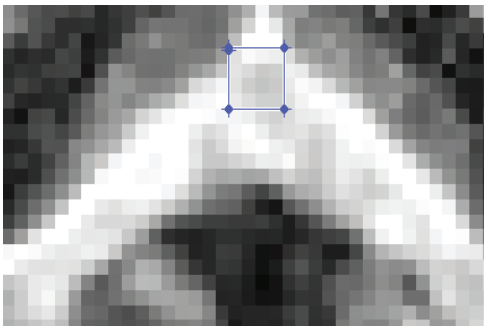

(a) FA

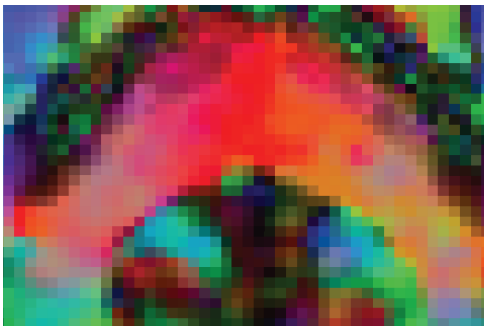

(b) FA modulated by principal eigenvector

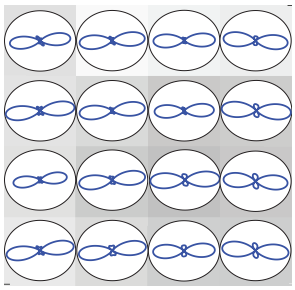

(c) BFOR at $t = 0$

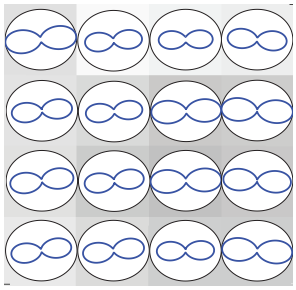

(d) BFOR at $t = 550$

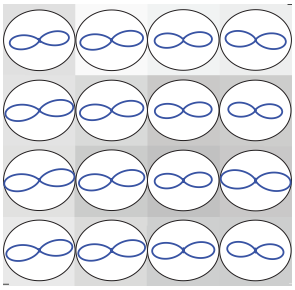

(e) DPI

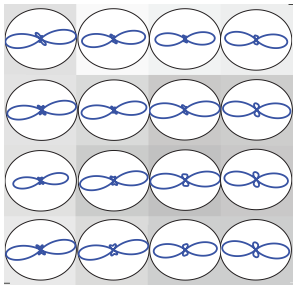

(f) SPFI

Figure 5.10: Axial slice of FA map of adult human brain at b=1500 s/mm^2 (second shell), where 4 × 4 ROI is drawn on splenium of corpus callosum. Plotted is the EAP profile at $p = 10$ μm overlaid on FA map in 4 × 4 ROI using BFOR at (c) $t = 0$, (d) $t = 550$, and (e) DPI and (f) SPFI.

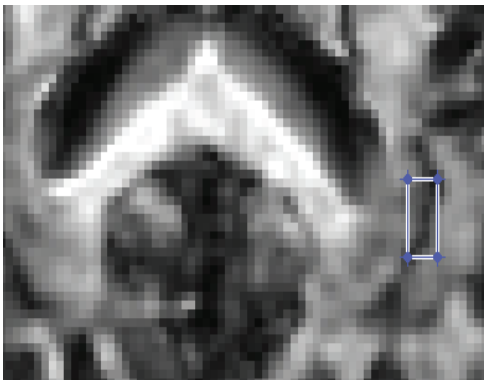

(a) FA

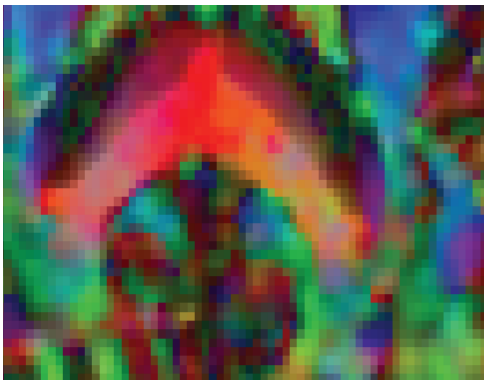

(b) FA modulated by principal eigenvector

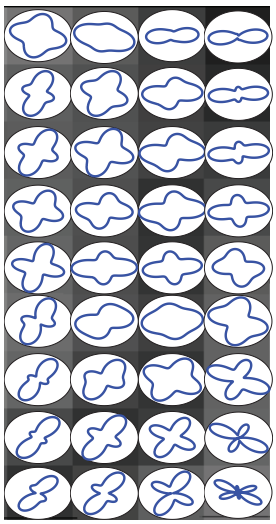

(c) BFOR at $t = 0$

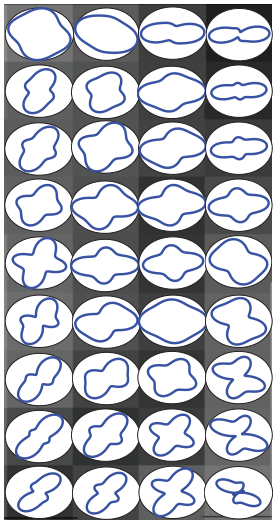

(d) BFOR at $t = 60$

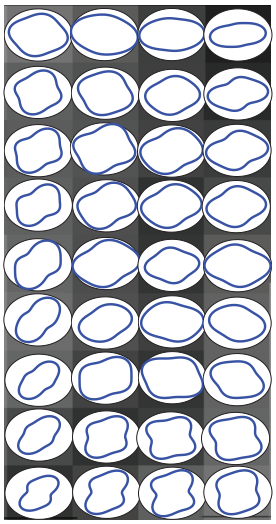

(e) DPI

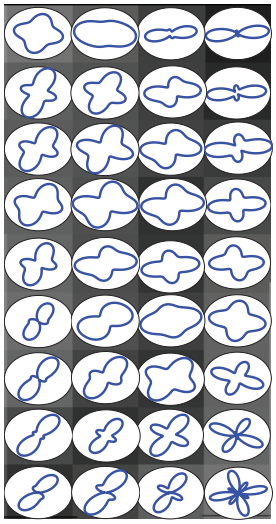

(f) SPFI

Figure 5.11: Axial slice of FA map of adult human brain at b=1500 s/mm^2 (second shell), where a 4 × 9 ROI is drawn on a region of crossing fibers. Plotted is the EAP profile at $p = 10$ μm overlaid on FA map in 4 × 9 ROI using (c) BFOR at $t = 0$, (d) $t = 60$, and (e) DPI and (f) SPFI. The splenium is to the left of the ROI.

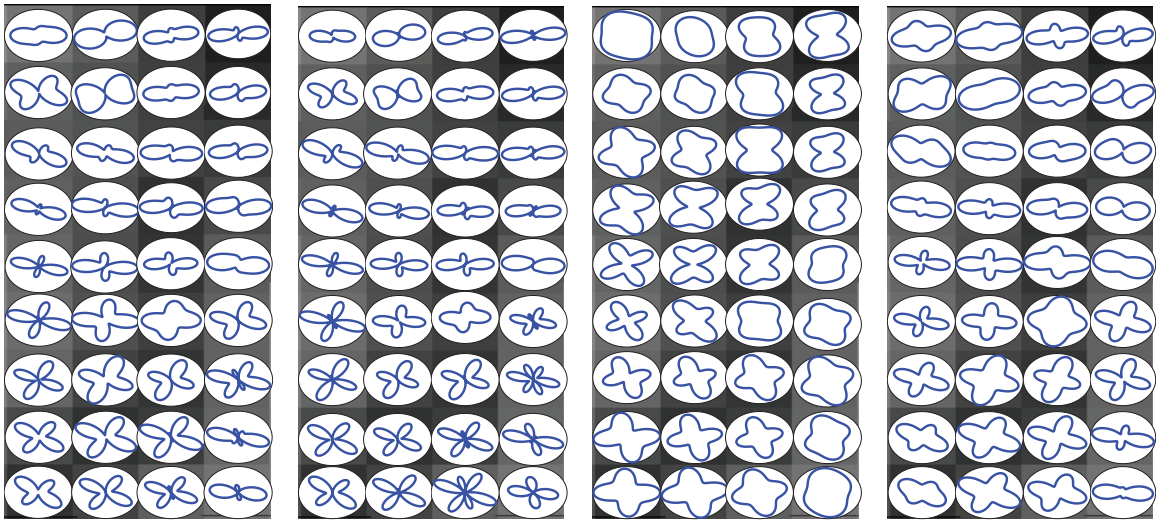

(a) BFOR at $t = 0$ (b) BFOR at $t = 60$ (c) BFOR at $t = 350$ (d) BFOR with Signal Extrap.

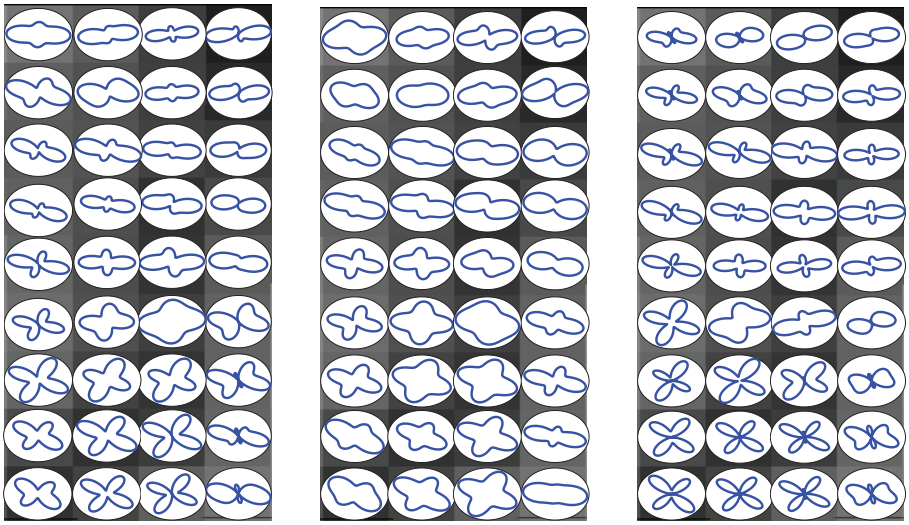

(e) SPFI (f) SPFI with Signal Extrap. (g) DPI

Figure 5.12: EAP profiles reconstructed at $p = 15$ μm for same crossing fiber region shown in Fig. 5.11.

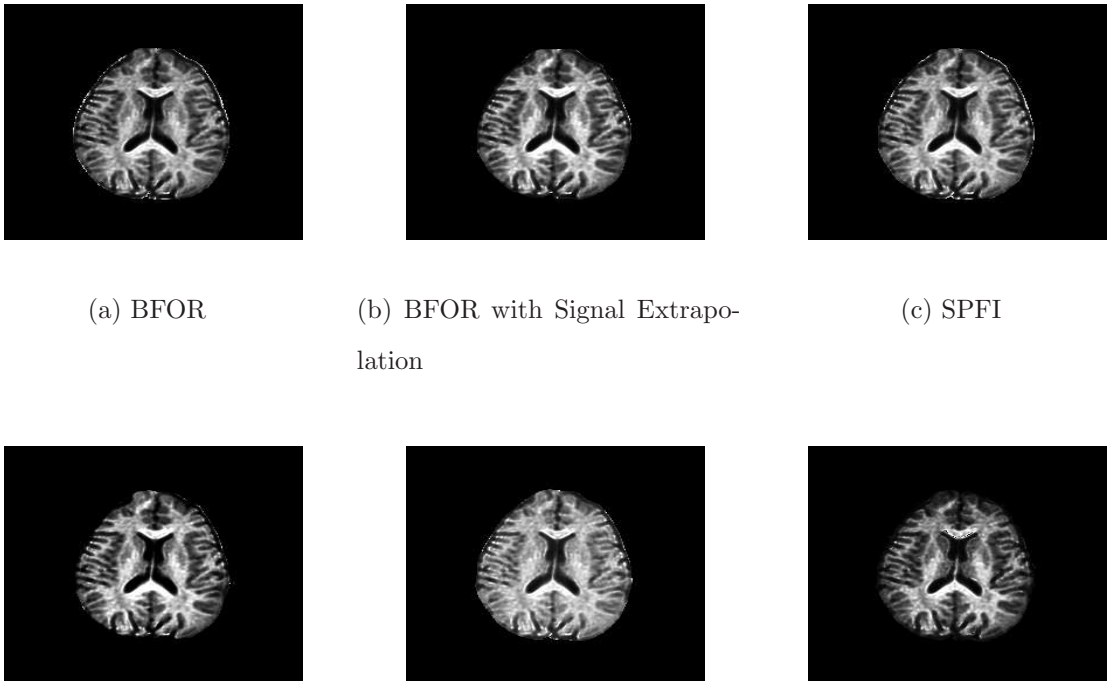

(a) BFOR

(b) BFOR with Signal Extrapolation

(c) SPFI

(d) SPFI with Signal Extrapolation

(e) DPI

(f) Numerical

Figure 5.13: Axial slice of *Po* generated by each method.

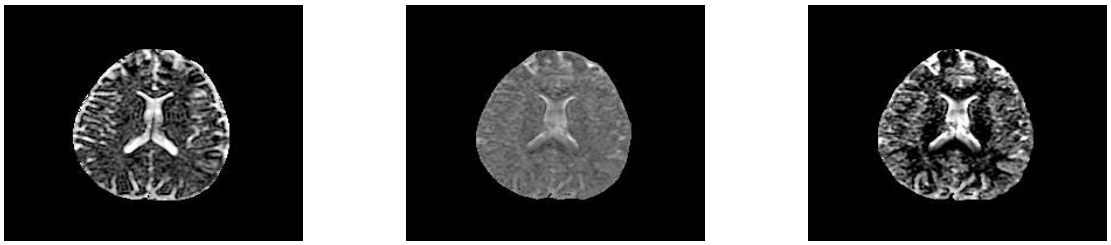

(a) BFOR

(b) BFOR with Signal Extrapolation

(c) SPFI

(d) SPFI with Signal Extrapolation

(e) DPI

(f) Numerical

Figure 5.14: Axial slice of MSD generated by each method.

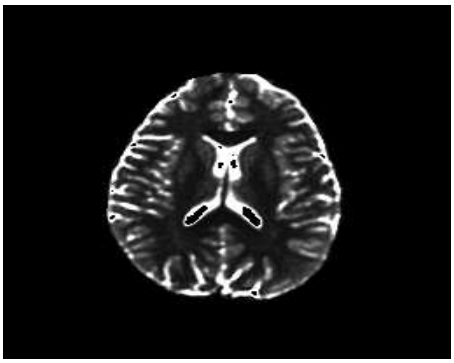

Figure 5.15: Axial slice of BFOR QIV. Within the CSF regions, some voxels were zeroed out because they blew up upon the division operation in computing QIV.

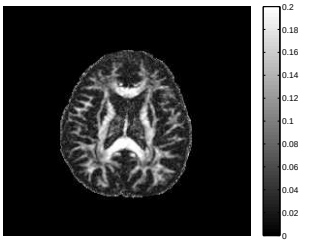

(a) $p = 5$ μm

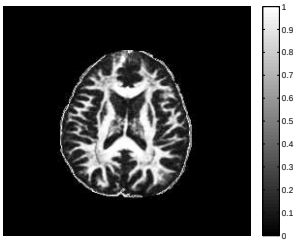

(b) $p = 10$ μm

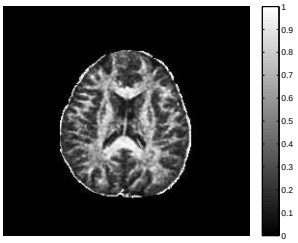

(c) $p = 15$ μm

BFOR

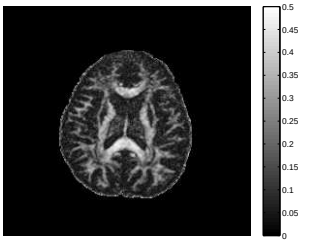

(d) $p = 5$ μm

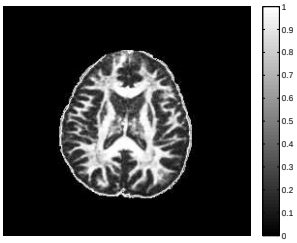

(e) $p = 10$ μm

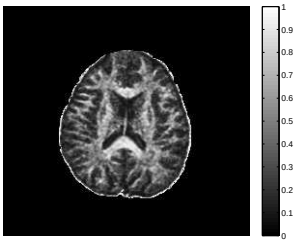

(f) $p = 15$ μm

BFOR with Signal Extrapolation

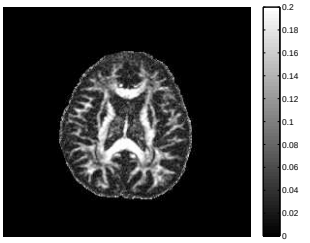

(g) $p = 5$ μm

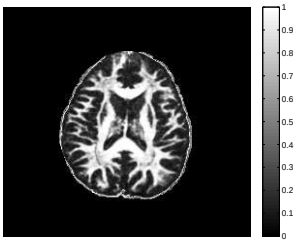

(h) $p = 10$ μm

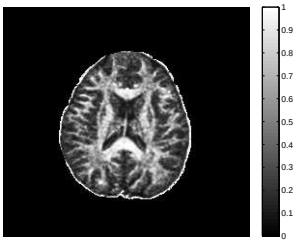

(i) $p = 15$ μm

SPFI

Figure 5.16: GFA maps computed at $p = 5$, 10, and 15 μm. Continues to next page.

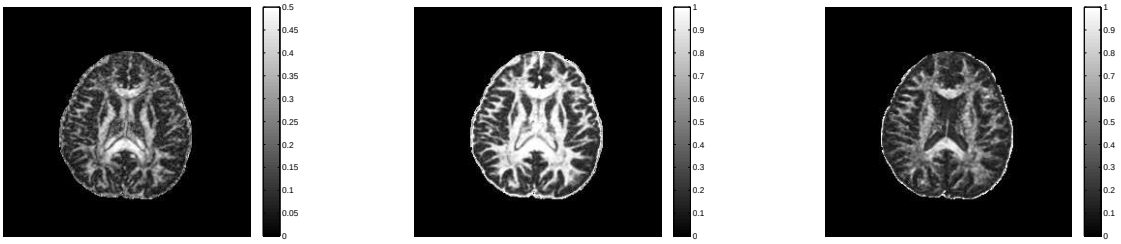

(j) $p = 5$ μm (k) $p = 10$ μm (l) $p = 15$ μm

SPFI with Signal Extrapolation

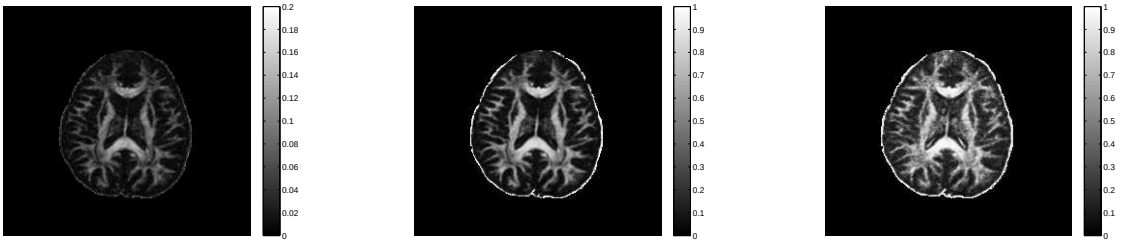

(m) $p = 5$ μm (n) $p = 10$ μm (o) $p = 15$ μm

DPI

Figure 5.16: GFA maps computed at $p = 5$, 10, and 15 μm.

5.A Derivation of BFOR Signal Basis

We want to solve the following boundary value partial differential equation:

$$\left[\frac{1}{q^2}\frac{\partial}{\partial q}(q^2\frac{\partial}{\partial q}) + \frac{1}{q^2\sin\theta}\frac{\partial}{\partial\theta}(\sin\theta\frac{\partial}{\partial\theta}) + \frac{1}{q^2\sin^2\theta}\frac{\partial^2}{\partial\phi^2}\right]\psi_i(\mathbf{q}) = -\lambda_i\psi_i(\mathbf{q}), \quad \psi(q=\tau,\theta,\phi) = 0 \tag{5.A.1}$$

where we require $\lambda > 0$. Substituting the separable solution of the form

$$\psi(q,\theta,\phi) = f(q)h(\theta,\phi) \tag{5.A.2}$$

into Eq. (5.A.1), we obtain

$$\frac{q^2}{f}\frac{d^2}{dq^2}f + \frac{2q}{f}\frac{d}{dq}f + q^2\lambda = -\frac{\Delta_{LB}h}{h} = l(l+1), \tag{5.A.3}$$

where $\Delta_{LB} = \frac{1}{\sin\theta}\frac{\partial}{\partial\theta}(\sin\theta\frac{\partial}{\partial\theta}) + \frac{1}{\sin^2\theta}\frac{\partial^2}{\partial\phi^2}$ is the Laplace-Bertrami operator and l is some real-valued constant.

We first solve for the second equation in (5.A.3):

$$\Delta_{LB}h + l(l+1)h = 0 \tag{5.A.4}$$

The solutions to Eq. (5.A.4) are the spherical harmonics (SH) $Y_l^m(\theta,\phi)$.

The first equation in (5.A.3) can be written as

$$q^2\frac{d^2}{dq^2}f + 2q\frac{d}{dq}f + [q^2\lambda - l(l+1)]f = 0 \tag{5.A.5}$$

Defining a new variable $f(q) = \sqrt{\frac{\pi}{2\sqrt{\lambda}q}}F(q)$, we can transform Eq. (5.A.5) to

$$q^2\frac{d^2}{dq^2}F + q\frac{d}{dq}F + [q^2\lambda - (l+1/2)^2]F = 0, \tag{5.A.6}$$

which is simply a sclaed version of the Bessel differential equation. The only bounded solution at the origin is given in terms of the Bessel funciton of the first kind as $F(q) = J_{l+1/2}(\sqrt{\lambda}q)$. The solution to Eq. (5.A.5) is then $f(q) = \sqrt{\frac{\pi}{2\sqrt{\lambda}q}}J_{l+1/2}(\sqrt{\lambda}q) = j_l(\sqrt{\lambda}q)$, where j_l is the spherical Bessel function of the first kind and we invoke the relation $j_l(x) = \sqrt{\frac{\pi}{2x}}J_{l+1/2}(x)$.

Imposing the boundary condition from Eq. (5.A.1), we have $j_l(\sqrt{\lambda}\tau) = 0$. Defining α_{nl} as the n^{th} root of the l^{th} order spherical Bessel function of first kind, then the eigenvalues are found to be $-\lambda_{nl} = -\frac{\alpha_{nl}^2}{\tau^2}$. Note that for $l = 0$, the roots are simply $\alpha_{n0} = n\pi$.

Multiplying the spherical Bessel functions and the spherical harmonics together, we obtain the eigenfuctions (i.e. our orthonormal basis) to (5.A.1): $Z_{nlm}(q,\theta,\phi) = j_l(\sqrt{\lambda_{nl}}q)Y_l^m(\theta,\phi)$.Thus, the complete set of solutions to Eq. (5.A.1) is

$$\psi(q,\theta,\phi) \approx \sum_{n=1}^{N}\sum_{l=0}^{L}\sum_{m=-l}^{l} C_{nlm}j_l(\frac{\alpha_{nl}q}{\tau})Y_l^m(\theta,\phi), \tag{5.A.7}$$

where N is the truncation order of the number of roots of spherical Bessel function and L the truncation order of the SH.

Now, to derive the diffusion signal, we make two important assumptions. First, we

assume the diffusion signal $E(\mathbf{q})$ is a solution to the heat equation:

$$\bigtriangledown^2 E(\mathbf{q},t) = \frac{\partial E}{\partial t}, \qquad E(\mathbf{q},t=0) = H(\mathbf{q}), \tag{5.A.8}$$

where $H(\mathbf{q})$ is simply the acquired signal. Second, we assume that the diffusion signal can be expressed as a linear combination of the orthonormal basis derived in Eq. (5.A.7):

$$E(q,\mathbf{u},t) = \sum_{n=1}^{N}\sum_{l=0}^{L}\sum_{m=-l}^{l} C_{nlm} g_{nlm}(t) j_l(\frac{\alpha_{nl} q}{\tau}) Y_l^m(\mathbf{u}) \tag{5.A.9}$$

Substituting (5.A.9) back into (5.A.8), we obtain

$$\sum_{n=1}^{N}\sum_{l=0}^{L}\sum_{m=-l}^{l} C_{nlm} j_l(\frac{\alpha_{nl} q}{\tau}) Y_l^m(\mathbf{u})[-\frac{\alpha_{nl}^2}{\tau^2} g_{nlm}(t) - \frac{d}{dt} g_{nlm}(t)] = 0 \tag{5.A.10}$$

A unique solution exists if and only if $g_{nl}(t) = b_{nl} e^{-\frac{\alpha_{nl}^2 t}{\tau^2}}$ [30], and so

$$E(q,\mathbf{u},t) = \sum_{n=1}^{N}\sum_{l=0}^{L}\sum_{m=-l}^{l} C_{nlm} e^{-\frac{\alpha_{nl}^2 t}{\tau^2}} j_l(\frac{\alpha_{nl} q}{\tau}) Y_l^m(\mathbf{u}) \tag{5.A.11}$$

Note that all constants are absorbed into C_{nlm}. In the following sections, we will use the SH basis Y_j proposed in [37].

5.B Diffusion Signal at Origin

In diffusion weighted imaging (DWI), $E(0) = 1$. Thus, for our basis, we obtain the following identity:

$$E(0, t = 0) = \sum_n \sum_j C_{nj} j_{l(j)}(0) Y_j(\mathbf{u}) = \frac{1}{\sqrt{4\pi}} \sum_n C_{n1} = 1, \tag{5.B.1}$$

which holds for any $\mathbf{u}$ within the unit sphere S^2 (i.e. $\mathbf{u} \in S^2$). In deriving Eq. (5.B.1), we invoked a basic property of the spherical Bessel function that

$$j_l(0) = \begin{cases} 1, & \text{if } l = 0 \\ 0, & \text{if } l \neq 0 \end{cases}$$

and the identity $Y_0^0 = \frac{1}{\sqrt{4\pi}}$.

5.C Derivation of Analytical BFOR EAP Solution

In the **Theory** section, we showed that

$$P(p, \mathbf{r}, t) = 4\pi \sum_{n=1}^{N} \sum_{j=1}^{R} (-1)^{l(j)/2} C_{nj} e^{\frac{-\alpha_{nl(j)}^2 t}{\tau^2}} Y_j(\mathbf{r}) I_{nl(j)}(p), \tag{5.C.1}$$

where $I_{nl(j)}(p) = \int_0^\tau q^2 j_{l(j)}(\frac{\alpha_{nl(j)}q}{\tau}) j_{l(j)}(2\pi qp)dq$. We rewrite $I_{n(l(j)}(p)$ in terms of the Bessel function of the first kind:

$$I_{nl(j)}(p) = \frac{1}{2}\sqrt{\frac{\pi\tau}{2\alpha_{nl(j)}p}} \int_0^\tau q J_{l(j)+1/2}(\frac{\alpha_{nl(j)}q}{\tau}) J_{l(j)+1/2}(2\pi qp)dq \tag{5.C.2}$$

Recall the Bessel function of first kind $J_k(ax)$, where k is some real-valued constant, satisfies

$$\left(x^2\frac{d^2}{dx^2} + x\frac{d}{dx} + [a^2x^2 - k^2]\right) J_k(ax) = 0 \tag{5.C.3}$$

Thus, by definition of the Bessel function, $J_{l(j)+1/2}(\frac{\alpha_{nl(j)}q}{\tau})$ and $J_{l(j)+1/2}(2\pi qp)$ satisfy

$$\left(q\frac{d^2}{dq^2} + \frac{d}{dq} + [\frac{\alpha^2_{nl(j)}q}{\tau^2} - \frac{(l(j)+1/2)^2}{q}]\right) J_{l(j)+1/2}(\frac{\alpha_{nl(j)}q}{\tau}) = 0 \tag{5.C.4}$$

$$\left(q\frac{d^2}{dq^2} + \frac{d}{dq} + [4\pi^2p^2q - \frac{(l(j)+1/2)^2}{q}]\right) J_{l(j)+1/2}(2\pi qp) = 0, \tag{5.C.5}$$

respectively. Multiplying Eq. (5.C.4) by $J_{l(j)+1/2}(2\pi qp)$ and Eq. (5.C.5) by $J_{l(j)+1/2}(\frac{\alpha_{nl(j)}q}{\tau})$ and then subtracting, we obtain

$$\begin{aligned} &J_{l(j)+1/2}(2\pi qp)\frac{d}{dq}\left[q\frac{d}{dq}J_{l(j)+1/2}(\frac{\alpha_{nl(j)}q}{\tau})\right] - J_{l(j)+1/2}(\frac{\alpha_{nl(j)}q}{\tau})\frac{d}{dq}\left[q\frac{d}{dq}J_{l(j)+1/2}(2\pi qp)\right] \\ &= q\left(4\pi^2p^2 - \frac{\alpha^2_{nl(j)}}{\tau^2}\right) J_{l(j)+1/2}(\frac{\alpha_{nl(j)}q}{\tau}) J_{nl(j)+1/2}(2\pi qp) \end{aligned}$$

Integrating the above from $q = 0$ to $q = \tau$ via integration by parts and noting that $J_{l(j)+1/2}(\alpha_{nl(j)}) = 0$, we have

$$\int_0^\tau qJ_{l(j)+1/2}(\frac{\alpha_{nl(j)}q}{\tau})J_{l(j)+1/2}(2\pi qp)dq = \frac{\tau J_{l(j)+1/2}(2\pi\tau p)\left[\frac{d}{dq}J_{l(j)+1/2}(\frac{\alpha_{nl(j)}q}{\tau})|_{q=\tau}\right]}{4\pi^2p^2 - \frac{\alpha^2_{nl(j)}}{\tau^2}} \tag{5.C.6}$$

The right side of Eq. (5.C.6) can be simplified via the Bessel recurrence relations $\frac{d}{dx}J_k(x) = \frac{1}{2}(J_{k-1}(x) - J_{k+1}(x))$:

$$\int_0^\tau qJ_{l(j)+1/2}(\frac{\alpha_{nl(j)}q}{\tau})J_{l(j)+1/2}(2\pi qp)dq = \frac{\alpha_{nl(j)}J_{l(j)+1/2}(2\pi\tau p)}{2\left(4\pi^2p^2 - \frac{\alpha^2_{nl(j)}}{\tau^2}\right)}(J_{l(j)-1/2}(\alpha_{nl(j)}) - J_{l(j)+3/2}(\alpha_{nl(j)})) \tag{5.C.7}$$

Using the Bessel recurrence relation $J_{k+1}(x) = \frac{2k}{x}J_k(x) - J_{k-1}(x)$, we obtain $J_{l(j)+3/2}(\alpha_{nl(j)}) = -J_{l(j)-1/2}(\alpha_{nl(j)})$, and so we can rewrite Eq. (5.C.7) as

$$\int_0^\tau qJ_{l(j)+1/2}(\frac{\alpha_{nl(j)}q}{\tau})J_{l(j)+1/2}(2\pi qp)dq = \frac{\alpha_{nl(j)}J_{l(j)-1/2}(\alpha_{nl(j)})J_{l(j)+1/2}(2\pi\tau p)}{4\pi^2p^2 - \frac{\alpha^2_{nl(j)}}{\tau^2}} \tag{5.C.8}$$

Substituting Eq. (5.C.8) back into (5.C.2), we obtain

$$I_{nl(j)}(p) = \frac{1}{2}\sqrt{\frac{\pi\tau}{2p}}\frac{\sqrt{\alpha_{nl(j)}}J_{l(j)-1/2}(\alpha_{nl(j)})J_{l(j)+1/2}(2\pi\tau p)}{\left(4\pi^2p^2 - \frac{\alpha^2_{nl(j)}}{\tau^2}\right)},$$

and so the EAP is then

$$P(p,\mathbf{r},t) = 2\tau\sqrt{2\pi^3}\sum_{n=1}^{N}\sum_{j=1}^{R}(-1)^{l(j)/2}C_{nj}e^{\frac{-\alpha^2_{nl(j)}t}{\tau^2}}Y_j(\mathbf{r})\frac{\sqrt{\alpha_{nl(j)}}J_{l(j)-1/2}(\alpha_{nl(j)})j_{l(j)}(2\pi\tau p)}{\left(4\pi^2p^2-\frac{\alpha^2_{nl(j)}}{\tau^2}\right)} \tag{5.C.9}$$

5.D Derivation of BFOR Zero-Displacement Probability

We can derive Po by evaluating Eq. (5.C.9) at $p = 0$:

$$Po = P(p=0,\mathbf{r}) = 2\tau\sqrt{2\pi^3}\sum_{n=1}^{N}C_{n1}Y_1(\mathbf{r})\frac{\sqrt{\alpha_{n0}}J_{-1/2}(\alpha_{n0})}{\frac{-\alpha^2_{n0}}{\tau^2}}$$

$$= \frac{2\tau\sqrt{2\pi^3}}{\sqrt{4\pi}}\sum_{n=1}^{N}C_{n1}\frac{\sqrt{\alpha_{n0}}\sqrt{\frac{2}{\pi\alpha_{n0}}}\cos(\alpha_{n0})}{\frac{-\alpha^2_{n0}}{\tau^2}} = 2\sqrt{\pi}\tau^3\sum_{n=1}^{N}C_{n1}\frac{(-1)^{n+1}}{\alpha^2_{n0}}, \tag{5.D.1}$$

where we used the relation $J_{-1/2}(x) = \sqrt{\frac{2}{\pi x}}\cos(x)$.

5.E Relationship between MSD and Diffusion Signal in q-Space

We define the wave vector $\mathbf{q}$ as $\mathbf{q} = q_x\widehat{i}+q_y\widehat{j}+q_z\widehat{k}$ and the radius vector in propagator space $\mathbf{p}$ as $\mathbf{p} = p_x\widehat{i}+p_y\widehat{j}+p_z\widehat{k}$. The norm of $\mathbf{p}$ is $p = \sqrt{p_x^2+p_y^2+p_z^2}$.

Since the diffusion signal and EAP are FT pairs, then the inversion of Eq. (5.1) gives

$$E(\mathbf{q}) = \int P(\mathbf{p}) e^{2\pi i \mathbf{q}\cdot\mathbf{p}} d^3\mathbf{p} = \int P(\mathbf{p}) e^{2\pi i (q_x p_x + q_y p_y + q_z p_z)} d^3\mathbf{p} \tag{5.E.1}$$

Taking the second derivative of $E(\mathbf{q})$ with respect to q_x, q_y, and q_z gives

$$\begin{aligned}
\frac{\partial^2 E(\mathbf{q})}{\partial q_x^2} &= (2\pi i)^2 \int p_x^2 P(\mathbf{p}) e^{2\pi i \mathbf{q}\cdot\mathbf{p}} d^3\mathbf{p} \\
\frac{\partial^2 E(\mathbf{q})}{\partial q_y^2} &= (2\pi i)^2 \int p_y^2 P(\mathbf{p}) e^{2\pi i \mathbf{q}\cdot\mathbf{p}} d^3\mathbf{p} \\
\frac{\partial^2 E(\mathbf{q})}{\partial q_z^2} &= (2\pi i)^2 \int p_z^2 P(\mathbf{p}) e^{2\pi i \mathbf{q}\cdot\mathbf{p}} d^3\mathbf{p}
\end{aligned}$$

The sum of the derivatives is simply the Laplacian operator acting on $E(\mathbf{q})$:

$$\bigtriangledown^2 E(\mathbf{q}) = \frac{\partial^2 E(\mathbf{q})}{\partial q_x^2} + \frac{\partial^2 E(\mathbf{q})}{\partial q_y^2} + \frac{\partial^2 E(\mathbf{q})}{\partial q_z^2} = (2\pi i)^2 \int p^2 P(\mathbf{p}) e^{2\pi i \mathbf{q}\cdot\mathbf{p}} d^3\mathbf{p} \tag{5.E.2}$$

Note that the Laplacian of $E(\mathbf{q})$ evaluated at $\mathbf{q} = 0$ is related to the second moment of the EAP. Thus, the MSD is

$$\langle p^2 \rangle = \frac{-1}{4\pi^2} \bigtriangledown^2 E(\mathbf{q})|_{\mathbf{q}=0} \tag{5.E.3}$$

For the case of DTI, where $E(q, \mathbf{u}) = e^{-4\pi^2 q^2 (\Delta - \delta/3)\mathbf{u}^T \mathbf{D}\mathbf{u}}$, Eq. (5.E.3) simplifies to the Einstein relation

$$\langle p^2 \rangle = 6(\Delta - \delta/3)MD \tag{5.E.4}$$

5.E.1 Derivation of BFOR MSD

The BFOR signal basis is an eigenfunction of the Laplacian operator, with eigenvalues $-\frac{\alpha_{nl(j)}^2}{\tau^2}$. Hence

$$\bigtriangledown^2 E(\mathbf{q}) = -\sum_{n=1}^{N}\sum_{j=1}^{R} C_{nj} \left(\frac{\alpha_{nl(j)}}{\tau}\right)^2 e^{-\alpha_{nl(j)}^2 t/\tau^2} j_{l(j)}(\frac{\alpha_{nl(j)} q}{\tau}) Y_j(\mathbf{u}) \tag{5.E.5}$$

Evaluating the Laplacian of $E(\mathbf{q})$ at $q = 0$ gives

$$\bigtriangledown^2 E(\mathbf{q})|_{\mathbf{q}=0} = \frac{-1}{2\sqrt{\pi}\tau^2} \sum_{n=1}^{N} C_{n1} \alpha_{n0}^2 e^{-\alpha_{n0}^2 t/\tau^2} \tag{5.E.6}$$

Substituting Eq. (5.E.6) into (5.E.3), we obtain

$$\langle p^2 \rangle_{BFOR} = \frac{1}{8\pi^{\frac{5}{2}}\tau^2} \sum_{n=1}^{N} C_{n1} \alpha_{n0}^2, \tag{5.E.7}$$

where we dropped the smoothing term.

5.F Relationship between QIV and EAP in q-Space

Using the definition of QIV, we have

$$\begin{aligned} QIV^{-1} = \int q^2 E(\mathbf{q}) d^3\mathbf{q} &= \int q^2 \left[\int P(\mathbf{p}) e^{2\pi i \mathbf{q}\cdot\mathbf{p}} d^3\mathbf{p} \right] d^3\mathbf{q} \\ &= \int P(\mathbf{p}) \left[\int q^2 e^{2\pi i \mathbf{q}\cdot\mathbf{p}} d^3\mathbf{q} \right] d^3\mathbf{p} \end{aligned} \tag{5.F.1}$$

The Dirac delta function is defined as

$$\delta(\mathbf{p}) = \int e^{2\pi i \mathbf{q}\cdot\mathbf{p}} d^3\mathbf{q} \tag{5.F.2}$$

Taking the second derivative of $\delta(\mathbf{p})$ with respect to p_x, p_y, and p_z gives

$$\begin{aligned} \frac{\partial^2 \delta(\mathbf{p})}{\partial p_x^2} &= (2\pi i)^2 \int q_x^2 e^{2\pi i \mathbf{q}\cdot\mathbf{p}} d^3\mathbf{q} \\ \frac{\partial^2 \delta(\mathbf{p})}{\partial p_y^2} &= (2\pi i)^2 \int q_y^2 e^{2\pi i \mathbf{q}\cdot\mathbf{p}} d^3\mathbf{q} \\ \frac{\partial^2 \delta(\mathbf{p})}{\partial p_z^2} &= (2\pi i)^2 \int q_z^2 e^{2\pi i \mathbf{q}\cdot\mathbf{p}} d^3\mathbf{q} \end{aligned}$$

The sum of the derivatives is simply the Laplacian operator acting on $\delta(\mathbf{p})$:

$$\bigtriangledown^2 \delta(\mathbf{p}) = \frac{\partial^2 \delta(\mathbf{p})}{\partial p_x^2} + \frac{\partial^2 \delta(\mathbf{p})}{\partial p_y^2} + \frac{\partial^2 \delta(\mathbf{p})}{\partial p_z^2} = (2\pi i)^2 \int q^2 e^{2\pi i \mathbf{q}\cdot\mathbf{p}} d^3\mathbf{q} \tag{5.F.3}$$

Thus, Eq. (5.F.1) becomes

$$QIV^{-1} = \frac{-1}{4\pi^2} \int P(\mathbf{p}) \left[\bigtriangledown^2 \delta(\mathbf{p}) \right] d^3\mathbf{p} \tag{5.F.4}$$

Since the Laplacian operator $\bigtriangledown^2$ is Hermitian and the EAP & $\delta(\mathbf{p})$ are real-valued, Eq. (5.F.4) can be equivalently stated as

$$QIV^{-1} = \frac{-1}{4\pi^2} \int P(\mathbf{p}) \left[\bigtriangledown^2 \delta(\mathbf{p}) \right] d^3\mathbf{p} = \frac{-1}{4\pi^2} \int \delta(\mathbf{p}) \left[\bigtriangledown^2 P(\mathbf{p}) \right] d^3\mathbf{p}$$

Exploiting the property of the Dirac delta function that $\int_{-\infty}^{\infty} f(x)\delta(x)dx = f(0)$, we have

$$QIV^{-1} = \frac{- \bigtriangledown^2 P(\mathbf{p})|_{\mathbf{p}=0}}{4\pi^2}, \tag{5.F.5}$$

which is very similar in form to Eq. 5.E.3. Thus, whereas the MSD directly varies with the Laplacian of the diffusion signal evaulated at the origin, the QIV inversely varies with the Laplacian of the EAP evaluated at the origin.

5.F.1 Derivation of BFOR QIV

$$\begin{aligned} QIV^{-1} &= \int q^2 E(\mathbf{q}) d^3\mathbf{q} \approx \sum_n \sum_j C_{nj} \int Y_j(\mathbf{u}) d^2\mathbf{u} \int_0^\tau q^4 j_{l(j)}(\frac{\alpha_{nl(j)} q}{\tau}) dq \\ &= \sqrt{4\pi} \sum_n C_{n1} \int_0^\tau q^4 j_0(\frac{\alpha_{n0} q}{\tau}) dq = \sqrt{4\pi}\tau \sum_n \frac{C_{n1}}{\alpha_{n0}} \int_0^\tau q^3 \sin(\frac{\alpha_{n0} q}{\tau}) dq \end{aligned} \tag{5.F.6}$$

The last integral can easily be solved via integration by parts, and so the QIV is

$$QIV_{BFOR} = \frac{1}{2\sqrt{\pi}\tau^5 \sum_{n=1}^{N} (-1)^n C_{n1} \frac{(6-\alpha_{n0}^2)}{\alpha_{n0}^4}} \tag{5.F.7}$$

5.G Energy (L2 Norm) of q-Space Signal

The total energy content, or L2 norm, of the q-space signal, is defined as

$$H = \int [E(\mathbf{q})]^2 d^3\mathbf{q} \tag{5.G.1}$$

Substituting the BFOR signal basis into Eq. (5.G.1) gives

$$\begin{aligned} H &= \sum_n \sum_j \sum_{n'} \sum_{j'} C_{nj} C_{n'j'} \left[\int Y_j(\mathbf{u}) Y_{j'}(\mathbf{u}) d^2\mathbf{u} \right] \left[\int_0^\tau q^2 j_{l(j)}(\frac{\alpha_{nl(j)} q}{\tau}) j_{l'(j')}(\frac{\alpha_{n'l'(j')} q}{\tau}) dq \right] \\ &= \sum_n \sum_{n'} \sum_j C_{nj} C_{n'j} \left[\int_0^\tau q^2 j_{l(j)}(\frac{\alpha_{nl(j)} q}{\tau}) j_{l(j)}(\frac{\alpha_{n'l(j)} q}{\tau}) dq \right], \end{aligned}$$

where we used $\int Y_j(\mathbf{u})Y_{j'}(\mathbf{u})d^2\mathbf{u} = \delta_{jj'}$. Since

$$\int_0^\tau q^2 j_{l(j)}(\frac{\alpha_{nl(j)}q}{\tau})j_{l(j)}(\frac{\alpha_{n'l(j)}q}{\tau})dq = \frac{\pi\tau^3}{4\alpha_{nl(j)}}[J_{l(j)+3/2}(\alpha_{nl(j)})]^2\delta_{nn'},$$

the total energy of the BFOR basis is

$$H_{BFOR} = \frac{\pi\tau^3}{4}\sum_{n=1}^{N}\sum_{j=1}^{R}\frac{C_{nj}^2}{\alpha_{nl(j)}}[J_{l(j)+3/2}(\alpha_{nl(j)})]^2 \tag{5.G.2}$$

Chapter 6

A Small Clinical Study using BFOR

6.1 Abstract

The ensemble average propagator (EAP) describes the 3D average diffusion process of water molecules, capturing both its radial and angular contents, and hence providing rich information about complex tissue microstructure properties. Bessel Fourier orientation reconstruction (BFOR) is one of several analytical, non-Cartesian EAP reconstruction schemes employing multiple shell acquisitions that have recently been proposed. Such modeling bases have not yet been fully exploited in the extraction of rotationally invariant q-space indices that describe the degree of diffusion anisotropy/restrictivity. Such quantitative measures include the zero-displacement probability (Po), mean squared displacement (MSD), q-space inverse variance (QIV), and generalized fractional anisotropy (GFA), and all are simply scalar features of the EAP. In this study, a general relationship between MSD and q-space diffusion signal is derived and an EAP-based definition

of GFA is introduced. A significant part of the paper is dedicated to utilizing BFOR in a clinical dataset, comprised of 5 multiple sclerosis (MS) patients and 4 healthy controls, to estimate Po, MSD, QIV, and GFA of corpus callosum, and specifically, to see if such indices can detect changes between normal appearing white matter (NAWM) and healthy white matter (WM). Although the sample size is small, this study is the first clinical application of an analytical EAP reconstruction technique and serves as a proof of concept that can be extended to larger sample sizes in the future.

6.2 Introduction

The aim of diffusion-weighted imaging (DWI) is to non-invasively estimate information about the diffusion of water molecules in biological tissues. The most common form of DWI is diffusion tensor imaging (DTI) [18], which is a good model of diffusion-weighted signal behavior at low levels of diffusion weighting. Rotationally invariant measures can be derived from the eigenvalues of the diffusion tensor, including fractional anisotropy (FA) and mean diffusivity (MD) [19], that have proven clinical value. However, DTI is limited by the Gaussian assumption, which is invalid at higher levels of diffusion weighting ($b > 2000$ s/mm^2) and its inability to resolve multiple fiber orientations within a voxel [73].

In order to recover complex white matter (WM) geometry, high angular resolution diffusion imaging (HARDI) [73], which reduces the diffusion signal sampling to a single sphere (i.e. single level of diffusion weighting) within q-space, was proposed. Many HARDI techniques [25,72] seek to extract the orientation distribution function (ODF), a probability density function describing the angular distribution of water molecules during

diffusion. However, the ODF only retrieves the angular content of the diffusion process.

The ensemble average propagator (EAP) provides the full information about the diffusion process in the tissue because it captures both the radial and angular information contained in the diffusion signal. The ODF is simply an angular feature of the EAP. Unlike the diffusion tensor, the EAP profiles illustrate and recover crossing fibers. The significance of the EAP in diffusion MRI has led to many reconstruction algorithms being proposed, some numerically based such as diffusion specturm imaging (DSI) [75] and hybrid diffusion imaging (HYDI) [80], and some analytically based such as diffusion propagator imaging (DPI) [37], spherical polar Fourier imaging (SPFI) [12,29], and Bessel Fourier orientation reconstruction (BFOR) [46].

With respect to analytical EAP reconstruction methods, one valuable though overlooked use is in extracting rotationally invariant quantitative measures from them. High angular resolution analogues of quantitative DTI indices such as generalized fractional anisotropy (GFA) [72] & mean squared displacement (MSD) [10, 80] and other q-space metrics like zero-displacement probablity (Po) [10] & q-space inverse variance (QIV) [81] are all scalar features of the EAP. Analytical representations of the EAP (and hence diffusion signal) facillitate either analytic computation of such features or numerical efficiency in estimating them. HYDI has already been used to numerically estimate Po, MSD, and QIV [81].

Multiple sclerosis (MS) is an inflammatory disease of the central nervous system in which the myelin sheaths surrounding the axons are damaged, leading to demyelination and scarring (i.e. lesions). T_2-weighted MRI and fluid-attenuated inversion recovery (FLAIR) are the conventional MR techniques used to identify hyperintense MS lesions

and measure the disease load, while gadolinium enhanced T_1-weighted images detect hypointense lesions. Although lesions reflect the acute response in MS, MR spectroscopy studies [35, 51] of MS brains have shown that normal-appearing white matter (NAWM[1]) areas on the T_2 and FLAIR images diplay abnormal metabolite distributions on many occasions, suggesting that NAWM may in fact be affected by MS. DTI and high b-value imaging studies [6, 76] on MS have obtained similar results, finding differences in fractional anisotropy, mean diffusivity, and Po between the NAWM of MS patients and the white matter (WM) of healthy controls.

In this paper, we present the first clinical application of an analytical EAP reconstruction method by using the BFOR framework to investigate MS. Specifically, we first derive analytical expressions for Po, MSD, & QIV using BFOR, and introduce an EAP-based definition of GFA. These quantitative measures are then utilized in a HYDI-acquired clinical dataset, comprising a healthy control group and MS patients, to see if they detect any differences in the corpus callosum between the NAWM of MS patients and healthy WM.

6.3 Theory

Let $P(\mathbf{p})$ and $E(\mathbf{q})$ be the EAP and normalized q-space diffusion signal, respectively. We denote $\mathbf{q} = q\ \mathbf{u}(\theta, \phi)$ and $\mathbf{p} = p\ \mathbf{r}(\theta', \phi')$, where $\mathbf{u}$ and $\mathbf{r}$ are 3D unit vectors. Under

[1]NAWM refers to white matter that appears normal on conventional T_1- and T_2-weighted images, but may in fact be affected by MS.

the narrow pulse assumption, $E(\mathbf{q})$ and $P(\mathbf{p})$ are Fourier Transform (FT) pairs [23]:

$$P(\mathbf{p}) = \int E(\mathbf{q}) e^{-2\pi i \mathbf{q}\cdot\mathbf{p}} d^3\mathbf{q} \tag{6.3.1}$$

The BFOR signal basis and EAP are, respectively,

$$E(\mathbf{q},t) = \sum_{n=1}^{N}\sum_{j=1}^{R} C_{nj} e^{\frac{-\alpha_{nl(j)}^2 t}{\tau^2}} j_{l(j)}\left(\frac{\alpha_{nl(j)} q}{\tau}\right) Y_j(\mathbf{u}) \tag{6.3.2}$$

and

$$P(\mathbf{p},t) = 2\tau\sqrt{2\pi^3}\sum_{n=1}^{N}\sum_{j=1}^{R}(-1)^{\frac{l(j)}{2}} C_{nj} e^{\frac{-\alpha_{nl(j)}^2 t}{\tau^2}} Y_j(\mathbf{r}) \frac{\sqrt{\alpha_{nl(j)}} J_{l(j)-1/2}(\alpha_{nl(j)}) j_{l(j)}(2\pi\tau p)}{\left(4\pi^2 p^2 - \frac{\alpha_{nl(j)}^2}{\tau^2}\right)}, \tag{6.3.3}$$

where $e^{\frac{-\alpha_{nl(j)}^2 t}{\tau^2}}$ is the smoothening term, C_{nj} are the expansion coefficients, and $\alpha_{nl(j)}$ is n^{th} root of l^{th} order spherical Bessel function of first kind j_l [46].

6.3.1 Rotationally Invariant Quantitative q-Space Indices

$Po = P(\mathbf{p} = 0)$ is the probability density of water molecules that minimally diffuse within the diffusion time [10,80], and hence a measure of restricted diffusion. In a healthy adult brain, Po is greater in white matter (WM) than gray matter (GM) because WM

has more restricting barriers including multi-layer myelin sheaths, axonal membranes, and microtubules. Several studies have shown Po to be sensitive to brain pathology, and suggesting that changes in myelin are the primary mechanism for differences in Po [6,82].

Po can be evaluated either numerically or analytically. The authors in [81] computed Po by numerically summing the normalized diffusion signal $E(\mathbf{q})$ over all diffusion measurements in q-space, and then correcting the sum by the sampling density. Analytical formulations of Po were derived for the SPFI and DPI signal bases [29, 37]. The BFOR Po can be computed analytically by evaluating Eq. (6.3.3) at $p = 0$:

$$Po = 2\sqrt{\pi}\tau^3 \sum_{n=1}^{N} C_{n1} \frac{(-1)^{n+1}}{\alpha_{n0}^2} \tag{6.3.4}$$

The MSD, which we will denote as $\langle p^2 \rangle$, is simply the second moment of the EAP [80]: $\langle p^2 \rangle = \int p^2 P(\mathbf{p}) d^3\mathbf{p}$. It is related to the MD, which in the case of Gaussian diffusion is given by the well-known Einstein relation $\langle p^2 \rangle = 6(\Delta - \delta/3)\mathrm{MD}$. Thus far, an analytical formulation of MSD exists only within the DTI framework. It is calculated numerically in q-space imaging, either by extracting the full width at half maximum of the EAP [10] or taking the geometrical mean of the diffusion signal over all directions on a HYDI shell [81].

A general relationship between the MSD and q-space diffusion signal has not yet been formulated. We have derived such a relationship:

$$\langle p^2 \rangle = \frac{-1}{4\pi^2} \bigtriangledown^2 E(\mathbf{q})|_{\mathbf{q}=0} \tag{6.3.5}$$

Using Eq. (6.3.5), an analytic MSD expression can be computed for BFOR because the BFOR signal basis, Eq. (6.3.2), is an eigenfunction of the Laplacian operator. Hence, it can be shown that

$$\langle p^2 \rangle_{BFOR} = \frac{1}{8\pi^{\frac{5}{2}}\tau^2} \sum_{n=1}^{N} C_{n1}\alpha_{n0}^2 \tag{6.3.6}$$

The MSD measure is quite sensitive to noise [80]. The authors in [81] proposed an alternative measure to MSD called the QIV, which is a pseudo-diffusivity measure. Mathematically, the QIV is defined as $QIV = \left[\int q^2 E(\mathbf{q}) d^3\mathbf{q}\right]^{-1}$. The QIV is not an arbitrary meausre, but related to the EAP in a manner analogous to which the MSD is related to the diffusion signal. In fact, we have derived a general relationship between the QIV and EAP:

$$QIV^{-1} = \frac{-1}{4\pi^2} \bigtriangledown^2 P(\mathbf{p})|_{\mathbf{p}=0} \tag{6.3.7}$$

The QIV within the BFOR framework is

$$QIV_{BFOR} = \frac{1}{2\sqrt{\pi}\tau^5 \sum_{n=1}^{N} (-1)^n C_{n1} \frac{(6-\alpha_{n0}^2)}{\alpha_{n0}^4}} \tag{6.3.8}$$

Tuch in [72] introduced the concept of GFA and defined it as std(ODF)/rms(ODF). Since ODF is only a feature of the EAP, the subsequent GFA map is derived soley from the angular content of the diffusion profile. Incorporating both the angular and radial

contents of the diffusion profile into the definition of GFA will result in a radial dial of GFA maps, illustrating how anisotropy varies with diffusion displacement p. Therefore, we define a new GFA:

$$GFA(p = p_o) = \frac{\text{std}\left[P(p = p_o, \mathbf{r})\right]}{\text{rms}\left[P(p = p_o, \mathbf{r})\right]} \tag{6.3.9}$$

Another advantage of Eq. (6.3.9) is that it is better suited for multiple diffusion weighted MR experiments, unlike Tuch's definition, which is HARDI-based.

6.4 Materials and Methods

The *in vivo* dataset uses a hybrid, non-Cartesian sampling scheme [80], shown in Table 6.1. Since EAP reconstruction is sensitive to angular resolution, the number of encoding directions is increased with each shell to increase the angular resolution with the level of diffusion weighting. The number of directions in the outer shells were increased to better characterize complex tissue organization.

HYDI was performed on five MS patients and four healthy volunteers using a 3.0 T GE-SIGNA whole body scanner. MR parameters were TE = 99 ms, TR 2300 ms, FOV = 24 cm, matrix = 96 x 96, voxel size = 2.5 x 2.5 mm^2, 15 slices with slice thickness = 5 mm, and scan time = 10 min. Diffusion parameters were $\Delta = 45$ ms, $\delta = 34$ ms, field of view of the diffusion displacement space $FOV_p = (1/\Delta q) = 71.4$ μm, and resolution of the diffusion displacement space $\Delta p = (1/2q_{max}) = 7.1$ μm [23].

DTI analysis was performed using the data in the second HYDI shell, in order to

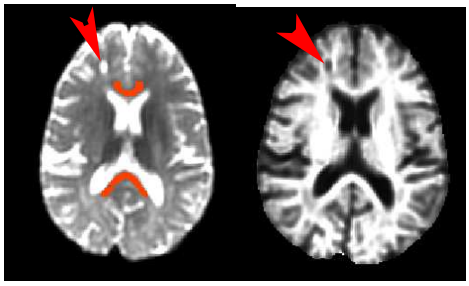

(a) T_2W (b) Po

Figure 6.1: Axial slice of T_2W and corresponding BFOR Po map illustrating corpus callosum ROI (red) and MS lesion (red arrow).

Table 6.1: HYDI Encoding Scheme for MS Study

Shell	Ne	q (mm^{-1})	Δq (mm^{-1})	b (s/mm^2)
	2	0		0
1st	6	14	14	260
2nd	21	28	14	1040
3rd	24	42	14	2340
4th	24	56	14	4160
5th	50	70	14	6500

obtain the FA and MD, with the FSL software package [79]. BFOR was then used to compute Po, MSD, QIV, and GFA, with model parameters set to $\{L = 4, N = 6, \tau = 84$ mm^{-1}, $\lambda_l = 10^{-6}, \lambda_n = 10^{-6}, t = 0\}$. Using the T_2W ($b = 0$ volume) and BFOR Po maps as references, ROIs of the genu and splenium of corpus callosum were then manually drawn for each subject, as shown in Fig. 6.1, which were also applied to the other quantitative maps. An unpaired two-sample t-test (one-tailed), assuming unequal variances, was then used to test whether the mean value of each index in the corpus callosum for the NAWM group was lower (FA, GFA & Po) or higher (DTI/BFOR MSD & QIV) than those from control group at 0.05 level.

6.5 Results

Fig. 6.2 displays axial slices of the BFOR computed Po, QIV, & MSD indices. Note that the QIV exhibits GM/WM contrast, unlike MSD. Within the CSF regions in QIV map, some voxels were zeroed out because they blew up upon the division operation in computing QIV. Fig. 6.3 shows axial slices of the GFA estimated at $p = 5$, 10, and 15 μm, illustrating how the anisotropy of different WM regions, such as the corpus callosum and capsules, varies with diffusion displacement p. CSF regions in the GFA map at $p = 15$ μm are more noisy than at 5 & 10 μm.

Fig. 6.4 displays the mean and standard deviation of GFA, MSD, QIV, Po, FA, and DTI MSD for each subject. The t-test yielded a statistically significant p-value between the mean value of each index in NAWM and healthy WM at 0.05 level for GFA(5) & GFA(10) and Po, implying a reduction in GFA and Po of NAWM in corpus callosum with respect to controls. Such findings are consistent with previous DTI [76] and q-space [6] MS studies that showed significant reductions in FA and Po of NAWM with respect to controls, respectively. Although the DTI FA was also statistically significant, the p-values for GFA(5) & GFA(10) are much smaller than for FA, suggesting that GFA may be more sensitive to pathologically induced changes in WM than normal FA. The BFOR MSD was not a statistically significant indicator of pathological changes in WM, which goes against the results of [6, 76] that showed MD/MSD to be significantly higher in NAWM with respect to controls. The DTI MSD, however, was found to be statistically significant, and the disparity in results between the DTI and BFOR MSD may be due to the high b-value (BFOR) MSD being very sensitive to noise [80]. The QIV, however, was found to be significantly higher in NAWM with respect to controls, and both it and GFA(10) had the highest statistical significances among all metrics. In general, the

BFOR computed measures validate the main finding of [6], being that q-space indices suggest abnormalities in the MS brain are not only confined to hyerintense lesions visible in T_2 images, but may also affect the surrounding NAWM.

6.6 Conclusion

This study is first clinical application of an analytical EAP reconstruction scheme. Although the study was limited by the small sample size, it demonstrates the potential that EAP-derived q-space indices have in assessing brain pathology. In the future, the same study should be repeated using a larger sample size, with measurements being made in other WM regions in addition to the corpus callosum. Future work also includes estimating the axial and radial diffusivities using an analytical EAP framework.

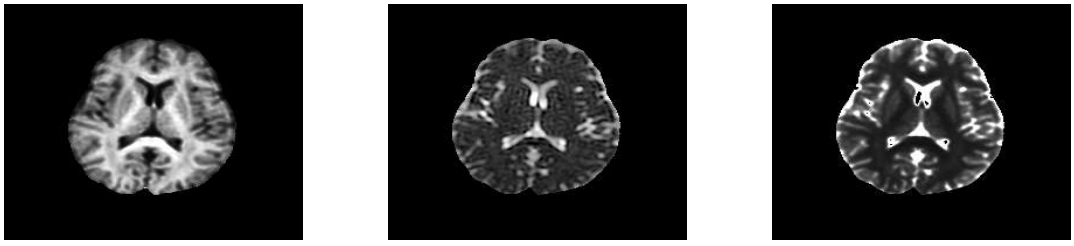

(a) Po (b) MSD (c) QIV

Figure 6.2: Axial slices of BFOR estimated Po, MSD, and QIV maps for a control.

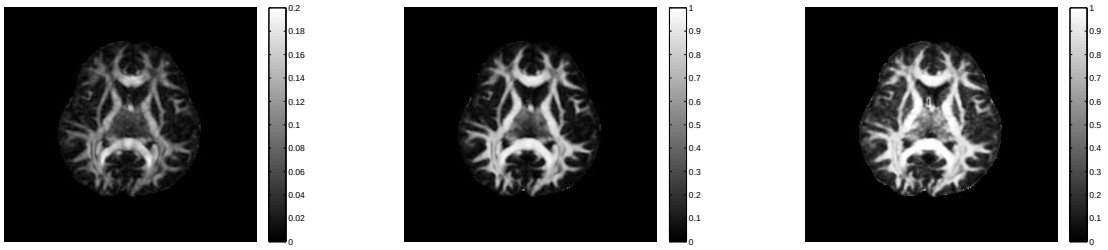

(a) $p = 5$ μm (b) $p = 10$ μm (c) $p = 15$ μm

Figure 6.3: Axial slices of BFOR GFA maps at $p = 5$, 10, and 15 μm for a control.

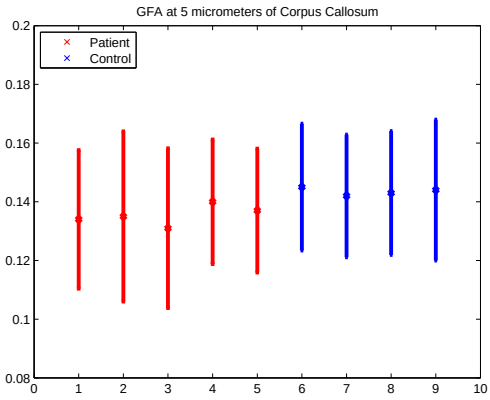

(a) GFA(5); p-value=0.0018

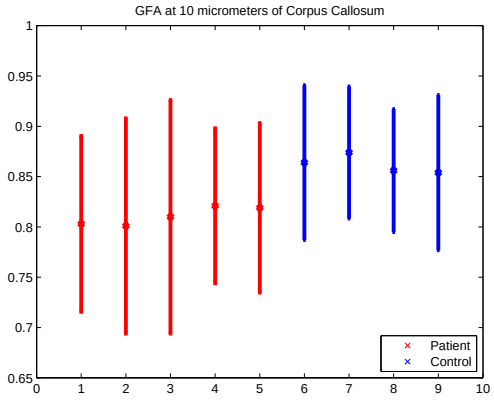

(b) GFA(10); p-value=4.8e-5

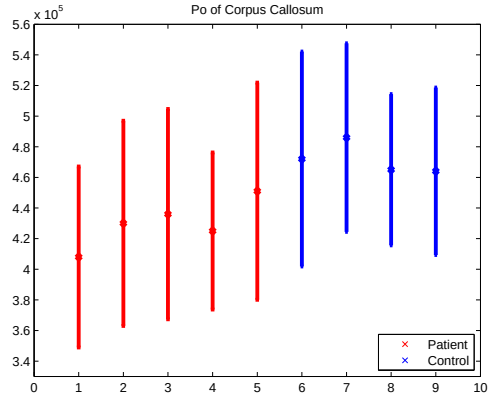

(c) *Po*; p-value=0.0011

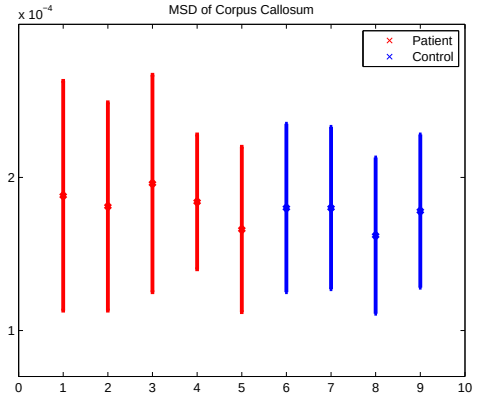

(d) BFOR MSD; p-value=0.13

Figure 6.4: Continues to next page.

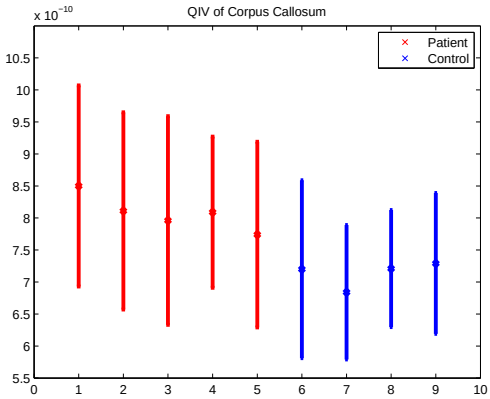

(e) QIV; p-value=3.0e-4

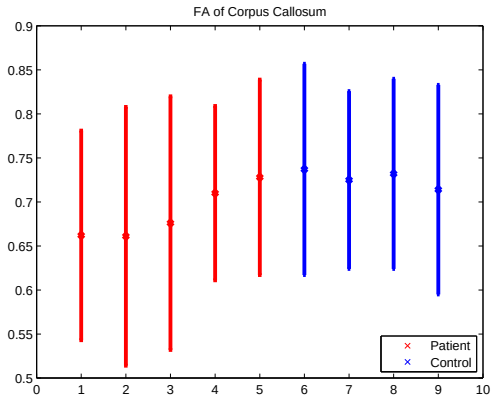

(f) DTI FA; p-value=0.020

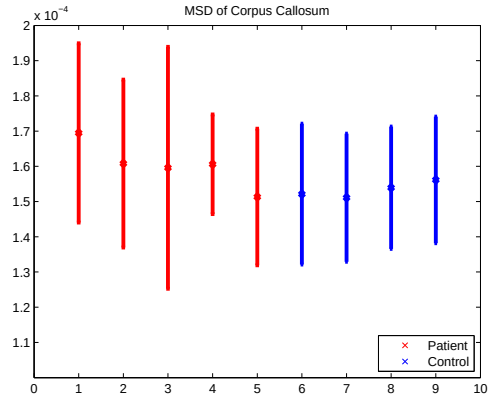

(g) DTI MSD; p-value=0.035

Figure 6.4: Plots of the mean and standard deviation of measures in corpus callosum for each subject, with the resulting p-value of the unpaired two-sample t-test (one-tailed).

Chapter 7

A 4D Hyperspherical Interpretation of q-Space

7.1 Abstract

3D q-space can be viewed as the surface of a 4D hypersphere. In this paper, we seek to develop a 4D hyperspherical interpretation of q-space by projecting it onto a hypersphere and subsequently modeling the q-space signal via 4D hyperspherical harmonics (HSH). Using this orthonormal basis, we analytically derive several quantitative indices and numerically estimate the diffusion ODF. Importantly, we derive the integral transform describing the relationship between the diffusion signal and propagator on a hypersphere. We also show that the HSH basis expends less fitting parameters than other well-established methods to achieve comparable signal and better ODF reconstructions. All in all, this work provides a new way of looking at q-space.

7.2 Introduction

One of the first physical applications of quantum mechanics was in solving the Schrödinger equation for the hydrogen atom. It had been solved in position-space by Schrödinger, himself [66], but not in momentum-space, which is related to position-space via the Fourier transform. The momentum-space solution was of interest to quantum chemists because it could potentially reveal additional quantum mechanical insights about the hydrogen atom not found in the position space solution. Nearly a decade after Schrödinger's landmark publication, V. Fock solved the Schrödinger equation for the hydrogen atom directly in momentum-space. In his classic paper [41], Fock stereographically projected 3D momentum-space onto the surface of a 4D unit hypersphere, and after this mapping was made, he was able to show that the momentum-space hydrogen orbitals could be simply expressed in terms of 4D hyperspherical harmonics (HSH), which are the multidimensional analogues of the 3D spherical harmonics.

In diffusion MRI, analogous to momentum- and position-space in quantum mechanics, the signal decay and ensemble average propagator (EAP) are Fourier transform (FT) pairs within the q-space framework:

$$P(\mathbf{k}) = \int E(\mathbf{q}) e^{-2\pi i \mathbf{q}\cdot\mathbf{k}} d^3\mathbf{q}, \tag{7.2.1}$$

where $\mathbf{k}$ is the displacement vector in EAP-space and $\mathbf{q}$ is the diffusion wave-vector in signal-space. We denote $\mathbf{q} = q\mathbf{u}(\theta, \phi)$ and $\mathbf{k} = k\mathbf{r}(\theta', \phi')$, where $\mathbf{u}$ and $\mathbf{r}$ are 3D unit vectors. An interesting problem, similar to that of the hydrogen atom, is whether a new interpretation of q-space can be obtained by stereographically projecting q-space and EAP-space onto a hypersphere.

In this paper, following the work of Fock, we seek to develop a 4D hyperspherical interpretation of q-space by focusing on four things: 1) Modeling the 3D q-space signal in terms of the 4D HSH, which is achieved by stereographically projecting 3D q-space onto the surface of a 4D hypersphere; 2) Using this single, orthonormal basis to reconstruct the diffusion orientation distribution function (ODF); 3) Computing the familiar q-space metric zero-displacement probability (Po) and introducing a novel hyperspherical diffusivity index; and 4) Deriving the integral transform that maps from the signal-hypersphere to the EAP-hypersphere. The last point is especially significant because the integral transform describing the relationship between any two functions individually existing on some n-dimensional sphere S^n, given that the two functions are FT pairs on the $(n-1)$-plane, has never been derived. Lastly, we compare the HSH basis to Bessel Fourier Orientation Reconstruction (BFOR) [47], and show that HSH expansion requires less fitting parameters than BFOR to achieve comparable signal and better ODF reconstructions.

7.3 Methods

7.3.1 4D Hyperspherical Harmonics

Consider the 4D unit hypersphere S^3 existing in $\mathbb{R}^4$. The Laplace-Beltrami operator on S^3 is defined as,

$$\Delta_{S^3} = \frac{1}{\sin^2\beta}\frac{\partial}{\partial\beta}\sin^2\beta\frac{\partial}{\partial\beta} + \frac{1}{\sin^2\beta}\Delta_{S^2}$$

where Δ_{S^2} is the Laplace-Beltrami operator on the unit sphere S^2. The eigenfuctions of Δ_{S^3} are the 4D HSH $Z_{nl}^m(\beta,\theta,\phi)$:

$$\Delta_{S^3} Z_{nl}^m = -l(l+2) Z_{nl}^m$$

The 4D HSH are defined as [38]

$$Z_{nl}^m(\beta,\theta,\phi) = 2^{l+1/2}\sqrt{\frac{(n+1)\Gamma(n-l+1)}{\pi\Gamma(n+l+2)}}\Gamma(l+1)\sin^l\beta\, C_{n-l}^{l+1}(\cos\beta)\, Y_l^m(\theta,\phi), \tag{7.3.1}$$

where (β,θ,ϕ) obey $(\beta \in [0,\pi], \theta \in [0,\pi], \phi \in [0,2\pi])$, C_{n-1}^{l+1} are the Gegenbauer (ultraspherical) polynomials, and Y_l^m are the 3D spherical harmonics. The Gegenbauer polynomials can be expressed in terms of the Gaussian (ordinary) hypergeometric function:

$$C_\alpha^\lambda(x) = \frac{\Gamma(\alpha+2\lambda)}{n!\Gamma(2\lambda)}\, {}_2F_1(-\alpha,\alpha+2\lambda;\lambda+\frac{1}{2};\frac{1}{2}(1-x))$$

The integers l and m denote the degree and order of the HSH, respectively, and $n = 0,1,2,....$ These three integers obey the conditions $0 \le l \le n$ and $-l \le m \le l$. The number of HSH corresponding to a given value of n is $(n+1)^2$. The first few 4D HSH are shown in Table 7.1. The HSH form an orthonormal basis on the hypersphere, and the normalization condition reads

$$\int_0^{2\pi}\int_0^{\pi}\int_0^{\pi} Z_{nl}^m(\beta,\theta,\phi) Z_{n'l'}^{m'*}(\beta,\theta,\phi)\sin^2\beta\sin\theta d\beta d\theta d\phi = \delta_{nn'}\delta_{ll'}\delta_{mm'} \tag{7.3.2}$$

Table 7.1: List of a Few HSH

$Z_{00}^{0}(\beta,\theta,\phi) = \frac{1}{\pi\sqrt{2}}$	$Z_{10}^{0}(\beta,\theta,\phi) = \frac{\sqrt{2}}{\pi}\cos\beta$
$Z_{11}^{-1}(\beta,\theta,\phi) = \frac{-\sqrt{2}}{\pi}\sin\beta\ \sin\theta\ \sin\phi$	$Z_{11}^{0}(\beta,\theta,\phi) = \frac{\sqrt{2}}{\pi}\sin\beta\ \cos\theta$
$Z_{11}^{1}(\beta,\theta,\phi) = \frac{-\sqrt{2}}{\pi}\sin\beta\ \sin\theta\ \cos\phi$	$Z_{20}^{0}(\beta,\theta,\phi) = \frac{1}{\pi\sqrt{2}}(3-4\sin^2\beta)$
$Z_{21}^{-1}(\beta,\theta,\phi) = \frac{-\sqrt{3}}{\pi}\sin 2\beta\ \sin\theta\ \sin\phi$	$Z_{21}^{0}(\beta,\theta,\phi) = \frac{\sqrt{3}}{\pi}\sin 2\beta\ \cos\theta$

7.3.2 4D Stereographic Projection of q-Space onto Hypersphere

For centuries, cartographers have struggled with the problem of how to represent the spherical-like surface of the Earth on a flat sheet of paper. One way to achieve this is via stereographic projection. To illustrate it, consider the simpler 3D case. The goal of stereographic projection is to associate each 2D point (u, v) in the equatorial plane with a unique point $P = (x, y, z)$ on the unit sphere. To achieve this, we construct the 3D line that passes through the north pole $N = (0, 0, 1)$ of the sphere and the given point $(u, v, 0)$. This line touches the surface of the sphere at exactly one point, P, and so the point $P = (x, y, z)$ is the stereographic projection of the point (u, v).

In order to model the q-space signal with the HSH, we need to map 3D q-space onto a 4D hypersphere of radius p_o, which can be achieved via stereographic projection. The q-space coordinates are defined as

$$q_x = q\sin\theta\cos\phi \quad q_y = q\sin\theta\sin\phi \quad q_z = q\cos\theta$$

The coordinates of the signal-hypersphere are defined by the 4D vector $\mathbf{s}$, whose components are

$$
\begin{aligned}
s_1 &= p_o \sin\beta \sin\theta \cos\phi \\
s_2 &= p_o \sin\beta \sin\theta \sin\phi \\
s_3 &= p_o \sin\beta \cos\theta \\
s_4 &= p_o \cos\beta.
\end{aligned}
$$

We will now derive the relationship between $\mathbf{q}$ and $\mathbf{s}$ as given by stereographic projection.

The 4D line that passes through the north pole of the hypersphere, $(0, 0, 0, p_o)$, and some point in q-space (q_x, q_y, q_z) is parameterized as

$$
s_1 = tq_x, \quad s_2 = tq_y, \quad s_3 = tq_z, \quad s_4 = p_o(1-t), \qquad -\infty < t < \infty \tag{7.3.3}
$$

The line touches the hypersphere when t satisfies

$$
p_o^2 = s_1^2 + s_2^2 + s_3^2 + s_4^2 = t^2(q_x^2 + q_y^2 + q_z^2) + p_o^2(1 - 2t + t^2), \tag{7.3.4}
$$

whose solution is $t = 2p_o^2/(q^2 + p_o^2)$[1]. Substituting our solution back into Eq. (7.3.3)

[1] $t = 0$ is a trivial solution because it corresponds to north pole of hypersphere.

gives the relationship between the two coordinate spaces:

$$\begin{aligned} s_1 &= \frac{2p_o^2 q_x}{q^2+p_o^2} = p_o \sin\beta \sin\theta \cos\phi \\ s_2 &= \frac{2p_o^2 q_y}{q^2+p_o^2} = p_o \sin\beta \sin\theta \sin\phi \\ s_3 &= \frac{2p_o^2 q_z}{q^2+p_o^2} = p_o \sin\beta \cos\theta \\ s_4 &= \frac{p_o(q^2-p_o^2)}{q^2+p_o^2} = p_o \cos\beta \end{aligned} \tag{7.3.5}$$

According to Eq. (7.3.5), the center of q-space $(0,0,0)$ projects onto the south pole $(0,0,0,-p_o)$ of the hypersphere. As $q \to \infty$, the projection (s_1, s_2, s_3, s_4) moves closer to the north pole $(0,0,0,p_o)$. Eq. (7.3.5) establishes a one-to-one correspondence between q-space and the 4D hypersphere. The radius of the hypersphere p_o controls the density of the projected q-space points onto the surface of the hypersphere.

Stereographic projection exhibits two important properties. First, it is conformal, which means it preserves angles - the angles (θ, ϕ) in q-space are preserved in 4D hyperspherical space. However, stereographic projection does not preserve volume; in general, the volume of a region in the 3D plane doesn't equal the volume of its projection onto the hypersphere. In fact, the degree of volume distortion in going from a differential volume element in q-space $d^3\mathbf{q}$ to that of the hypersphere $dV = p_o^3 d\Omega$ can be shown to be

$$d^3\mathbf{q} = \left(\frac{q^2+p_o^2}{2p_o}\right)^3 \frac{1}{p_o^3} dV = \left(\frac{q^2+p_o^2}{2p_o}\right)^3 d\Omega = \left(\frac{p_o}{1-\cos\beta}\right)^3 d\Omega, \tag{7.3.6}$$

where $d\Omega = \sin^2\beta \sin\theta d\beta d\theta d\phi$ is the differential area of the hypersphere. We will derive Eq. (7.3.6) later in this chapter.

7.3.3 Diffusion Signal Modeling via HSH Basis

Stereographically projecting q-space onto the hypersphere results in the q-space signal existing along the surface of the hypersphere. According to Fourier analysis, any square-integrable function defined on a sphere can be expanded in terms of the spherical harmonics. Thus, stereographic projection allows the 3D q-space signal to be expanded in terms of the HSH:

$$E_{p_o}(\beta, \theta, \phi) \approx \sum_{n=0}^{N} \sum_{l=0}^{n} \sum_{m=-l}^{l} C_{nlm} Z_{nl}^{m}(\beta, \theta, \phi), \tag{7.3.7}$$

where E_{p_o} denotes the q-space signal existing on hypersphere of radius p_o. The realness of the diffusion signal requires use of the real HSH, and so we employ a modified real basis proposed in [**?**] for Y_l^m.

An important axiom to state is that the q-space signal, itself, remains invariant after the mapping - that is, for a given q-space point (q_x, q_y, q_z) and its corresponding projection on the hypersphere (s_1, s_2, s_3, s_4), $E(q_x, q_y, q_z) = E_{p_o}(s_1, s_2, s_3, s_4)$. In q-space, the diffusion signal is even i.e. $E(q_x, q_y, q_z) = E(-q_x, -q_y, -q_z)$. Evenness in q-space doesn't necessarily translate into evenness on the hypersphere. According to Eq. (7.3.5), $(-q_x, -q_y, -q_z)$ projects to $(-s_1, -s_2, -s_3, s_4)$, and so evenness in q-space is tantamount to $E_{p_o}(s_1, s_2, s_3, s_4) = E_{p_o}(-s_1, -s_2, -s_3, s_4)$ on the hypersphere, indicating that the signal is not even on the hypersphere. In other words, stereographic projection destroys

evenness, i.e. a function even in the plane is no longer even on the sphere upon projection. For this reason, we are free to use both the even and odd HSH. Thus, for a given truncation order N, the total number of expansion coefficients is $W = (N+1)(N+2)(2N+3)/6$.

7.3.4 Relationship between EAP and q-Space Signal on Hypersphere

Any point in 3D EAP space, the Fourier pair of q-space, is given by

$$k_x = k\sin\theta'\cos\phi' \quad k_y = k\sin\theta'\sin\phi' \quad k_z = k\cos\theta'$$

Now lets stereographically project 3D EAP-space onto a 4D hypersphere of radius p_o, whose coordinates are defined by the 4D vector $\mathbf{v} = (v_1, v_2, v_3, v_4)$. The relationship between $\mathbf{k}$ and $\mathbf{v}$ is then

$$\begin{aligned} v_1 &= \frac{2p_o^2 k_x}{k^2+p_o^2} = p_o\sin\beta'\sin\theta'\cos\phi' \\ v_2 &= \frac{2p_o^2 k_y}{k^2+p_o^2} = p_o\sin\beta'\sin\theta'\sin\phi' \\ v_3 &= \frac{2p_o^2 k_z}{k^2+p_o^2} = p_o\sin\beta'\cos\theta' \\ v_4 &= \frac{p_o(k^2-p_o^2)}{k^2+p_o^2} = p_o\cos\beta' \end{aligned} \tag{7.3.8}$$

The Fourier relationship given in Eq. (7.2.1) between the signal and EAP does not hold true on the hypersphere. The question, then, is what integral transform maps from the signal-hypersphere to the EAP-hypersphere, and this problem is illustrated in Fig.

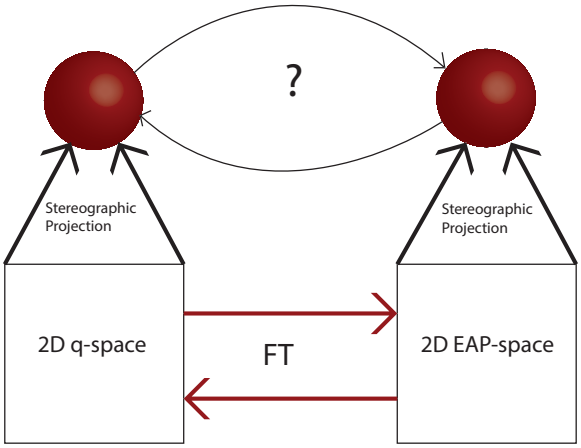

Figure 7.1: Q-space and EAP-space, which are FT pairs, are each stereographically projected onto a sphere. As a result, the diffusion signal and EAP each exist on a sphere, and the question then is finding the integral transform that maps from the signal-sphere to the EAP-sphere.

7.1. We will now proceed to derive this hyperspherical integral transform, which has never been derived before.

First, lets express the Fourier kernel in Eq. (7.2.1) in terms of the hyperspherical coordinates displayed in (7.3.5) and (7.3.8). The dot product of the 3D vectors $\mathbf{q}$ and $\mathbf{k}$ is

$$\mathbf{q} \cdot \mathbf{k} = qk[\sin\theta\cos\phi\sin\theta'\cos\phi' + \sin\theta\sin\phi\sin\theta'\sin\phi' + \cos\theta\cos\theta'] \quad (7.3.9)$$

Similarly, the dot project of the 4D vectors $\mathbf{s}$ and $\mathbf{v}$ is

$$\frac{\mathbf{s}\cdot\mathbf{v}}{p_o^2\sin\beta\sin\beta'} = \sin\theta\cos\phi\sin\theta'\cos\phi' + \sin\theta\sin\phi\sin\theta'\sin\phi' + \cos\theta\cos\theta' + \frac{\cos\beta\cos\beta'}{\sin\beta\sin\beta'}$$

(7.3.10)

We know from (7.3.5) that $\frac{q^2-p_o^2}{q^2+p_o^2} = \cos\beta$, which means $q = p_o\sqrt{\frac{1+\cos\beta}{1-\cos\beta}}$. Similarly, $k = p_o\sqrt{\frac{1+\cos\beta'}{1-\cos\beta'}}$. The relationship between the two dot products, (7.3.9) and (7.3.10), is then

$$\mathbf{q}\cdot\mathbf{k} = \frac{1}{(1-\cos\beta)(1-\cos\beta')}(\mathbf{s}\cdot\mathbf{v} - s_4 v_4) \tag{7.3.11}$$

The next and final step is to find the relationship between the differential volume element in q-space, $d^3\mathbf{q}$, and that of the hypersphere, dV. The differential volume element in q-space is simply $d^3\mathbf{q} = q^2\sin\theta dq d\theta d\phi$, while that of the hyperpshere is $dV = p_o^3\sin^2\beta\sin\theta d\beta d\theta d\phi$. Since $\cos\beta = \frac{q^2-p_o^2}{q^2+p_o^2}$, it can be shown then that $\frac{d\beta}{dq} = \frac{2p_o}{q^2+p_o^2}$ and $\sin^2\beta = \left(\frac{2p_o q}{q^2+p_o^2}\right)^2$. Hence, we have

$$d^3\mathbf{q} = \left(\frac{q^2+p_o^2}{2p_o}\right)^3 d\Omega = \left(\frac{p_o}{1-\cos\beta}\right)^3 d\Omega,$$

which is simply Eq. (7.3.6).

Substituting relations (7.3.11) and (7.3.6) into Eq. (7.2.1) gives the integral transform relating the signal-hypersphere to that of the EAP:

$$P_{p_o}(\mathbf{v}) = p_o^3\int E_{p_o}(\mathbf{s})\frac{e^{-2\pi i[\mathbf{s}\cdot\mathbf{v}-s_4v_4]/(1-\cos\beta)(1-\cos\beta')}}{(1-\cos\beta)^3}d\Omega, \tag{7.3.12}$$

where P_{p_o} denotes the EAP existing on hyphersphere of radius p_o. Just as with the q-space signal, the EAP remains invariant after the mapping. Eq. (7.3.12) is not one of the more familiar integral transforms encountered in mathematics literature.

7.3.5 HSH Metrics

A well-known q-space metric is $Po \equiv P(\mathbf{k} = 0)$ [10, 80], which is a measure of diffusion restrictivity. $\mathbf{k} = 0$ corresponds to the south pole of the EAP-hypersphere i.e. $\beta' = \pi$. Hence using Eq. (7.3.12) and the HSH basis, we can derive a hyperspherical Po:

$$Po = P_{p_o}(\beta' = \pi) = \int_{\Omega \in S^3} \frac{E_{p_o}(\mathbf{s})}{(1 - \cos\beta)^3} d\Omega = \int_{\Omega \in S^3} \left(\frac{q^2 + p_o^2}{2p_o} \right)^3 E_{p_o}(\mathbf{s}) d\Omega \tag{7.3.13}$$

The integral in (7.3.13) is difficult to evaluate analytically, which is due to the non-volume-preserving nature of stereographic projection. To overcome this, we compute an uncorrected Po by assuming q-space is uniformly projected onto the hypersphere:

$$\begin{aligned} Po_{unc} = \int_{\Omega \in S^3} E_{p_o}(\Omega) dV &= p_o^3 \sum_{n,l,m} C_{nlm} \int_{\Omega \in S^3} Z_{nl}^m(\Omega) d\Omega \\ &= \pi\sqrt{2} p_o^3 C_{000} \end{aligned} \tag{7.3.14}$$

where we use the fact that $Z_{00}^0 = \frac{1}{\pi\sqrt{2}}$. Po_{unc} will, naturally, suffer from volume distortion, which is corrected for by a signal weighting operation discussed in the next section.

Examples of q-space distance metrics include the q-space inverse variance (QIV) [47, 81] and the mean squared displacement (MSD) [10, 80], which are measures of diffusivity and only pertinent to planes. A useful distance metric defined on the hypersphere is the chordal distance [65], denoted χ. Consider the two q-space points $Q = (q_x, q_y, q_z)$ and

$\widehat{Q} = (\widehat{q}_x, \widehat{q}_y, \widehat{q}_z)$ and their corresponding projections on the hypersphere $S = (s_1, s_2, s_3, s_4)$ and $\widehat{S} = (\widehat{s}_1, \widehat{s}_2, \widehat{s}_3, \widehat{s}_4)$, respectively. Then the Euclidean (4D) distance between the projections S and $\widehat{S}$ on the hypersphere is given by the chordal distance, and it can be shown that

$$\chi = \chi(Q, \widehat{Q}) = \frac{2p_o^2\sqrt{(q_x - \widehat{q}_x)^2 + (q_y - \widehat{q}_y)^2 + (q_z - \widehat{q}_z)^2}}{\sqrt{q^2 + p_o^2}\sqrt{\widehat{q}^2 + p_o^2}},$$

where $\widehat{q} = \sqrt{\widehat{q}_x^2 + \widehat{q}_y^2 + \widehat{q}_z^2}$. If $\widehat{Q} = \mathbf{0}$, then the distance between the projection S and the south pole is

$$\chi_{sp}(q) \equiv \chi(Q, 0) = \frac{2p_o q}{\sqrt{q^2 + p_o^2}} \tag{7.3.15}$$

Likewise, if $\widehat{q} \to \infty$, then the distance between the projection S and the north pole is

$$\chi_{np}(q) \equiv \chi(Q, \infty) = \frac{2p_o^2}{\sqrt{q^2 + p_o^2}} \tag{7.3.16}$$

Geometrically, χ_{np} and χ_{sp} are the chords on the hypersphere that form the legs of a right triangle (by Thales' theorem), with the hypersphere's diameter the hypotenuse, as shown in Fig. 7.2.

The ratio of these 2 chordal lengths illuminates the relationship between the hypersphere radius p_o and q-space:

$$p_o = q\frac{\chi_{np}(q)}{\chi_{sp}(q)} \ \ (= \text{constant}) \tag{7.3.17}$$

If $p_o > q$ ($\chi_{np} > \chi_{sp}$), then upon stereographic projection the q-space signal will lie on the upper hemisphere of the hypersphere. If $p_o < q$ ($\chi_{np} < \chi_{sp}$), then upon stereographic projection the signal will lie on the lower hemisphere of the hypersphere. If $p_o = q$ ($\chi_{np} = \chi_{sp}$), then the projected signal will lie on the equator of the hypersphere. Thus, the hypersphere radius governs the location on the hypersphere at the which the q-space signal will exist upon stereographic projection.

According to Eq. (7.3.5), $\cos\beta = \frac{q^2-p_o^2}{q^2+p_o^2}$. Using Eq. (7.3.15) and (7.3.16), it can be shown then that

$$CSD(Q) \equiv \cos\beta = \frac{\chi_{sp}^2 - \chi_{np}^2}{4p_o^2},$$

which we define as the chordal squared difference (CSD). We then define the mean chordal squared difference (MCSD) as the CSD averaged over the surface of the signal-hypersphere i.e. $\langle\cos\beta\rangle$:

$$MCSD \equiv \langle\cos\beta\rangle = p_o^3 \int_{\Omega\in S^3} \cos\beta \; E_{p_o}(\Omega) d\Omega = \frac{\pi}{\sqrt{2}} p_o^3 C_{100}, \tag{7.3.18}$$

where we use the fact that $Z_{10}^0 = \sqrt{2}\cos\beta/\pi$. MCSD is an inherently hyperspherical metric, whereas Po is a native q-space metric.

7.3.6 Numerical Implementation and Estimation of ODF

In general, we are given k HARDI shell datasets. The number of encoding directions in each shell does not have to be the same. Each HARDI dataset corresponds to a dif-

ferent b-value. Across all k shells, we have total of M diffusion measurements (including the $b = 0$ measurement). The task then is to estimate the coefficients C_{nlm} in Eq. (7.3.7) from the observed signal.

Let $\Omega_j = (\beta_j, \theta_j, \phi_j)$ denote the hyperspherical angles corresponding to the j^{th} diffusion measurement. Denote $\mathbf{G}$ as the M x 1 vector representing the M diffusion signal measurements across all k shells, $\mathbf{C}$ the W x 1 vector of unknown expansion coefficients C_{nlm}, and $\mathbf{A}$ the M x W matrix constructed with the HSH basis

$$\mathbf{A} = \begin{pmatrix} Z_{00}^0(\Omega_1) & Z_{10}^0(\Omega_1) & Z_{11}^{-1}(\Omega_1) & Z_{11}^0(\Omega_1) & Z_{11}^1(\Omega_1) & \cdots & Z_{NN}^N(\Omega_1) \\ \vdots & \vdots & \vdots & \vdots & \ddots & \vdots & \\ Z_{00}^0(\Omega_M) & Z_{10}^0(\Omega_M) & Z_{11}^{-1}(\Omega_M) & Z_{11}^0(\Omega_M) & Z_{11}^1(\Omega_M) & \cdots & Z_{NN}^N(\Omega_M) \end{pmatrix}$$

Thus, we have a linear model of the form $\mathbf{G} = \mathbf{AC}$. This system of over-determined equations is solved via linear least squares with Laplace-Beltrami regularization (LBR), yielding $\widehat{\mathbf{C}} = (\mathbf{A}^T\mathbf{A} + \lambda_l\mathbf{L}_{reg})^{-1}\mathbf{A}^T\mathbf{G}$, where $\mathbf{L}_{reg}$ is the LBR diagonal matrix with entries $l^2(l+2)^2$ along the diagonal. The regularization serves to reinforce the positivity constraint of the signal.

Using Eq. (7.3.6), we correct for the volume distortion induced in Po_{unc} by weighing each signal shell in q-space by $\left(\frac{q_i^2+p_o^2}{2p_o}\right)^3$, where q_i is the radius of the i^{th} shell, before signal fitting. The resulting "weighted" coefficients are then solely used for computing Po via Eq. (7.3.14). The q-shell radii are listed in Table 1. The volume weighting of each q-shell, in this case, can be viewed as a sampling density correction of the projected q-space points on the hypersphere.

Given the intricacy of Eq. (7.3.12), it is difficult to estimate the EAP analytically

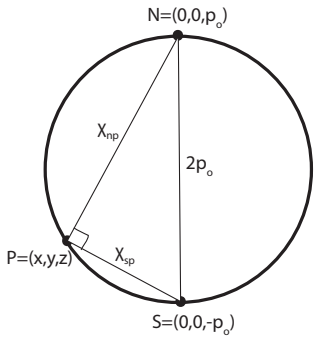

Figure 7.2: Geometric illustration of χ_{np} and χ_{sp}, where P is the stereographic projection onto the sphere of a point on the plane. The two chords form the legs of a right triangle, with the diameter of the hypersphere the hypotenuse.

Table 7.2: HYDI Encoding Scheme

Shell	Ne	q (mm^{-1})	Δq (mm^{-1})	b (s/mm^2)
	7	0		0
1st	6	15.79	15.79	300
2nd	21	31.58	15.79	1200
3rd	24	47.37	15.79	2700
4th	24	63.16	15.79	4800
5th	50	78.95	15.79	7500

using the HSH framework. However, the zeroth-order diffusion ODF [72], given by Eq. (4.11), can be numerically estimated. Lets construct a 11 x 11 x 11 ($-q_{max} : \Delta q : q_{max}$) Cartesian lattice, which we map onto the 4D hypersphere via Eq. (7.3.5). Once we have computed the HSH expansion coefficients via LLS from the acquired data, Eq. (5.7) can then be used the estimate the signal at any location on the hypersphere, including the projected lattice points. The stereographic projection establishes a one-to-one correspondence between the lattice and hypersphere, meaning that a given lattice point and its corresponding projection on the hypersphere have the same signal value. Hence, taking the fast Fourier transform (FFT) of the HSH-estimated signal for the lattice gives the EAP. The radial projection of the EAP then yields the ODF. Since the zeroth-order ODF is not inherently normalized, we min-max normalize it [72].

7.4 Experiments

The synthetic and *in vivo* datasets use a hybrid, non-Cartesian q-space sampling scheme (HYDI) [80], shown in Table 1.

Synthetic Data. Synthetic experiments were done the same way as in [47], with data generated via the bi-exponential mixture model. We look at two equally weighed fibers crossing at 45°, and set eigenvalues of each diffusion tensor to be [1.6,0.4,0.4]e-3, which gives FA=0.7071. Monte Carlo noise simulations were performed to investigate the effect of SNR on the signal reconstruction. Five SNR levels ([10 20 30 40 80]) for the $b = 0$ image were simulated, 1000 times each, in a similar manner as in [47], and the quality of the HSH signal fit is assessed by computing the normalized mean squared error (NMSE), given by $\frac{||S-\widehat{S}||^2}{||S||^2}$. The HSH parameters are $N = 4$, $p_o = 42$, and $\lambda_l = 10^{-6}$ and those of BFOR are taken from [47]. In the signal fitting, *HSH expends* $W = 55$ *parameters while BFOR uses 90.*

Fig. 7.3 displays the HSH signal fit for each shell and the corresponding ground truth in absence of noise, and shows that the HSH basis fits the diffusion signal nearly perfectly across all b-values. Fig. 7.4 displays the results of the noise simulations, with the NMSE plotted against SNR for each shell, and shows that the HSH and BFOR bases have a nearly identical robustness to noise. Fig. 7.5 shows the ground truth, HSH-estimated, and BFOR ODF profiles in absence of noise, indicating that the HSH basis succesfully captures the geometry and orientation of the ODF profile. However, as with the Laplacian modeling framework in diffusion propagator imaging (DPI) [37], the HSH basis smoothens the ODF peaks. The BFOR-estimated ODF is not as accurate as that of HSH.

Real Data. HYDI was performed on a healthy, adult human using a 3 T GE-SIGNA whole body scanner. MR parameters were TE=102 ms, TR=6500 ms, FOV=24 cm, matrix=96 x 96, voxel size=2.5 x 2.5 mm^2, 43 slices with slice thickness=3 mm, and scan time=15 min. Diffusion parameters were $\delta = 37.86$ ms and $\Delta = 43.1$ ms.

Axial slices of Po, computed via HSH and BFOR bases, and MCSD are shown in Fig. 7.6. The Po map closely resembles BFOR's, exhibiting both tissue/CSF and WM/GM constrasts. The HSH Po map, however, has sharper WM/GM contrast than BFOR's (compare the left and right putamen in both maps), which probably arises from the signal weighting operation. The MCSD map has tissue/CSF contrast but very little WM/GM contrast, and interestingly, closely resembles a mean squared displacement map. The MCSD can be viewed as a hyperspherical diffusivity measure, and specifically, an index of isotropic diffusion in neural tissue.

The HSH basis is not symmetric on the hypersphere (since both odd and even HSH are used), which poses a problem with regards to ODF reconstruction for *in vivo* data. Unlike synthetic experiments, where the q-space signal is guaranteed to be symmetric, the q-space signal acquired from *in vivo* data may not be symmetric due to noise, motion, geometric distortion, etc. For BFOR, this is not an issue because its inherent symmetry will impose symmetry on the *in vivo* data. However, for the HSH basis, asymmetric *in vivo* data will result in asymmetric ODF profiles. Since the q-space signal is theoretically a symmetric function, we get around this problem by requiring that the *in vivo* data satisfies $E(\mathbf{q}) = E(-\mathbf{q})$. That is, the mathematical reflection of the q-space coordinates used in the acquisition outputs the measured *in vivo* signal. In essence then, we are inflating our data not by acquiring more data, but by exploiting prior information regarding the q-space signal (in this case, its symmetry). Such an approach is in the

same spirit as the signal extrapolation employed in Chapter 5 to ameliorate truncation effects.

In Fig. 7.7, a 4 x 4 ROI was drawn on a slice from a BFOR-estimated GFA(10) map in a region comprising both signal and crossing fibers. Imposing symmetry on the *in vivo* data, the ODF profile for each voxel in the ROI was estimated with the HSH basis. Based on results shown in Fig. 7.8, we see that the HSH successfully resolve both single and multiple fiber orientations, but have the undesirable effect of oversmoothing the ODF profiles like DPI.

7.5 Discussion

We have introduced a new orthonormal basis to model the 3D q-space signal, and from which various metrics can be analytically derived. 4D HSH signal modeling allows for the capture of the radial and angular contents of the diffusion profile by a single basis function, and the basis' orthonormality provides robust numerical stability. The HSH basis' ability to give as good a signal reconstruction as BFOR and better ODF reconstruction, but with less fitting parameters, implies that it may be better suited to sparser sampling schemes than BFOR. Major drawbacks of the hyperspherical interpretation of q-space, however, are the destruction of the q-space signal's symmetry by stereographic projection and the difficulty in estimating the EAP via Eq. 7.3.12. Future work for HSH signal modeling includes implementing it on sparser q-space sampling schemes, estimating the EAP, and determining the exact biological narrative conveyed by the MCSD.

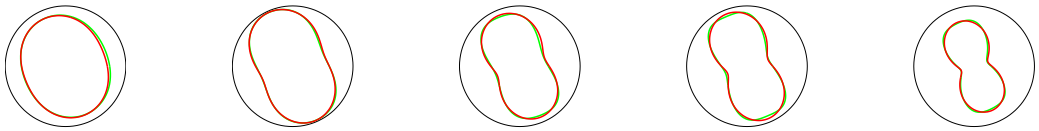

(a) b=300 (b) b=1200 (c) b=2700 (d) b=4800 (e) b=7500

Figure 7.3: The ground truth diffusion signal (green) and reconstructed signal (red) using HSH basis in absence of noise. Two equally weighted WM fibers were simulated crossing at 45°. Measurements from all 5 shells were used.

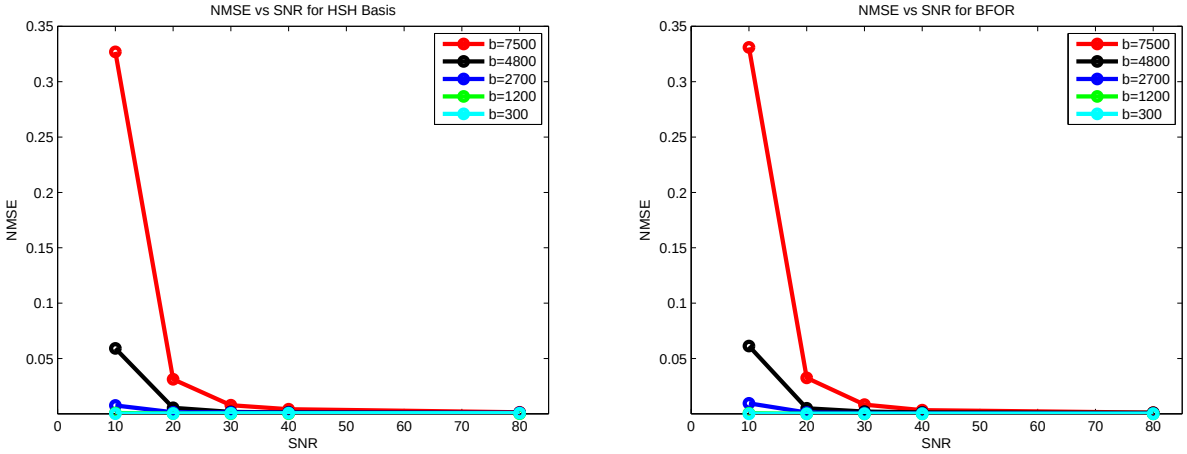

(a) NMSE for HSH basis (b) NMSE for BFOR

Figure 7.4: The normalized mean squared error (NMSE) of the HSH signal fit, left, and BFOR signal fit, right, for each b-value plotted against SNR. 1000 noise trials were simulated for each SNR level for two equally weighted fibers crossing at 45°.

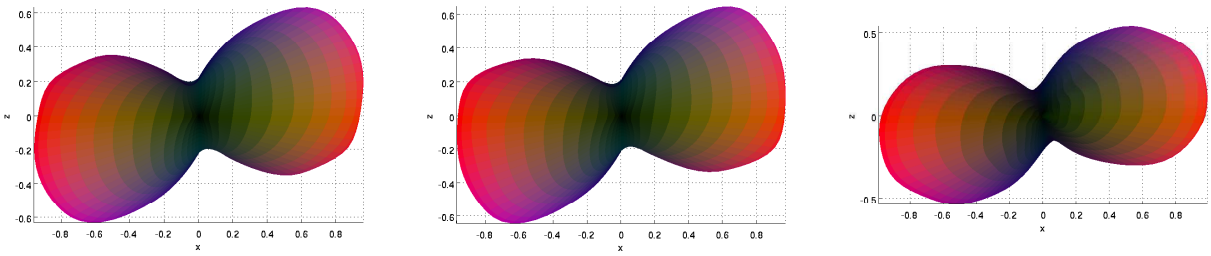

(a) HSH ODF (b) Ground Truth ODF (c) BFOR ODF

Figure 7.5: The HSH-estimated ODF, ground truth ODF, and BFOR ODF in absence of noise for two equally weighted fibers crossing at 45°. The ODF is normalized to [0 1].

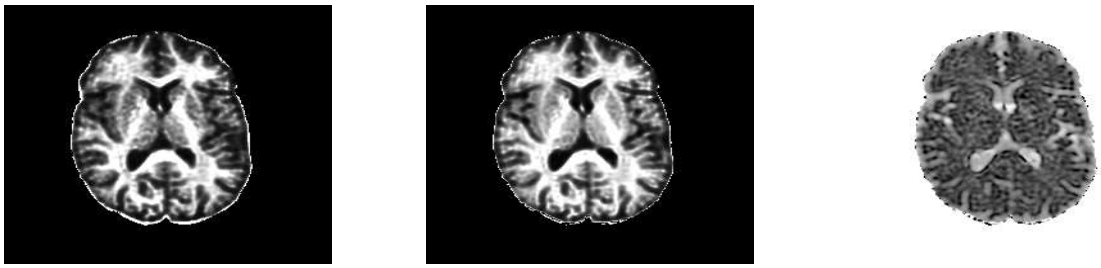

(a) HSH *Po* (b) BFOR *Po* (c) MCSD

Figure 7.6: Axial slices of *Po*, computed via HSH and BFOR bases, and MCSD maps of a healthy, adult human brain.

Figure 7.7: Axial slice of GFA(10) map of adult human brain. A 4 x 4 ROI is drawn on a region (adjacent to splenium) where we expect single and crossing fibers (i.e. dark streaks).

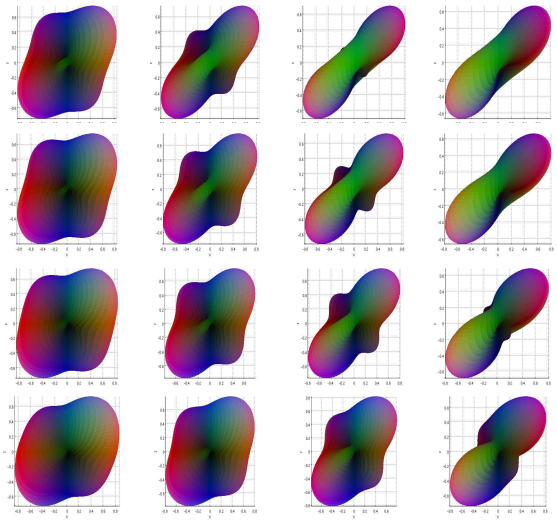

Figure 7.8: Plotted is the HSH-estimated ODF profiles overlaid on ROI in GFA(10) map.

7.A Preservation of Angles in Stereographic Projection

Stereographic projection is an example of a conformal mapping, meaning it preserves angles. In this section, we will prove this property by considering the stereographic projection of 3D space onto a 4D hypersphere. 3D space is defined by Cartesian coordinates (x, y, z), or equivalently by spherical coordinates (r, θ, ϕ). The 4D hypersphere (of radius p_o) is defined by Cartesian coordinates (u_1, u_2, u_3, u_4), or equivalently by hyperspherical coordinates $(p_o, \theta_{sp}, \phi_{sp}, \beta)$. Our task is to show that $\theta = \theta_{sp}$ and $\phi = \phi_{sp}$.

Recall from Section 7.3.2 that stereographic projection dictates the relationship be-

tween (x, y, z) and (u_1, u_2, u_3, u_4) to be

$$\begin{aligned} u_1 &= \frac{2p_o^2 x}{r^2 + p_o^2} \\ u_2 &= \frac{2p_o^2 y}{r^2 + p_o^2} \\ u_3 &= \frac{2p_o^2 z}{r^2 + p_o^2} \\ u_4 &= \frac{p_o(r^2 - p_o^2)}{r^2 + p_o^2} \end{aligned} \tag{7.A.1}$$

Lets look at coordinates u_3 and u_4. In 4D hyperspherical coordinates, $u_3 = p_o \sin\beta \cos\theta_{sp}$ and $u_4 = p_o \cos\beta$. The angle β is then given by $\beta = \arccos(u_4/p_o)$, which substituting into u_3 gives

$$\begin{aligned} u_3 = p_o \sin(\arccos(u_4/p_o)) \cos\theta_{sp} &= p_o \sqrt{1 - \frac{u_4^2}{p_o^2}} \cos\theta_{sp} \\ &= \sqrt{u_1^2 + u_2^2 + u_3^2} \cos\theta_{sp}, \end{aligned} \tag{7.A.2}$$

where we used the fact that $\sin(\arccos(x)) = \sqrt{1 - x^2}$. The angle θ_{sp} is then given by

$$\theta_{sp} = \arccos\left(\frac{u_3}{\sqrt{u_1^2 + u_2^2 + u_3^2}}\right) \tag{7.A.3}$$

Lets look at the argument of the inverse cosine function in Eq. (7.A.3). Substituting Eq. (7.A.1) gives

$$\frac{u_3}{\sqrt{u_1^2+u_2^2+u_3^2}} = \frac{2p_o^2 z}{r^2+p_o^2}\,\frac{r^2+p_o^2}{2p_o^2 r} = \frac{z}{r} = \cos\theta$$

Consequently,

$$\therefore \theta_{sp} = \arccos(\cos\theta) = \theta$$

We can prove $\phi_{sp} = \phi$ in a similar manner. Thus, we have completed our proof that stereographic projection preserves angles.

7.B Parity of Hyperspherical Harmonics

The parity of a function refers to whether it is even or odd. In 3D Cartesian coordinates, the parity operation is

$$x \to -x$$
$$y \to -y$$
$$z \to -z$$

To demonstrate the parity of the HSH, it will be convenient to express Eq. (7.3.1) as

$$Z_{nl}^{m}(\beta,\theta,\phi) = p_{nl}(\beta)\; Y_{l}^{m}(\theta,\phi),$$

where

$$p_{nl}(\beta) = 2^{l+1/2}\sqrt{\frac{(n+1)\Gamma(n-l+1)}{\pi\Gamma(n+l+2)}}\Gamma(l+1)\sin^{l}\beta\; C_{n-l}^{l+1}(\cos\beta)$$

In 4D hyperspherical coordinates, the parity operation is

$$\begin{aligned} r &\rightarrow r \\ \beta &\rightarrow \pi-\beta \\ \theta &\rightarrow \pi-\theta \\ \phi &\rightarrow \pi+\phi \end{aligned}$$

The parity operator acting on the HSH gives

$$\begin{aligned} &Z_{nl}^{m}(\pi-\beta,\pi-\theta,\pi+\phi) = p_{nl}(\pi-\beta)Y_{l}^{m}(\pi-\theta,\pi+\phi) \\ &= 2^{l+1/2}\sqrt{\frac{(n+1)\Gamma(n-l+1)}{\pi\Gamma(n+l+2)}}\Gamma(l+1)\sin^{l}\beta\; C_{n-l}^{l+1}(-\cos\beta)Y_{l}^{m}(\pi-\theta,\pi+\phi)), \end{aligned} \qquad (7.B.1)$$

where we used the fact that $\sin(\pi-\beta)=\sin\beta$ and $\cos(\pi-\beta)=-\cos\beta$. The parity of the spherical harmonics dictates

$$Y_l^m(\pi-\theta,\pi+\phi)=(-1)^l Y_l^m(\theta,\phi)$$

Likewise, the parity of the Gegenbauer polynomials [49] dictates

$$C_\nu^\lambda(-x)=(-1)^\nu C_\nu^\lambda(x),$$

which means $C_{n-l}^{l+1}(-\cos\beta)=(-1)^{n-1}C_{n-1}^{l+1}(\cos\beta)$. Eq. (7.B.1) thus becomes

$$\begin{aligned} Z_{nl}^m(\pi-\beta,\pi-\theta,\pi+\phi) &= (-1)^{n-l}(-1)^l p_{nl}(\beta)Y_l^m(\theta,\phi) \\ &= (-1)^n p_{nl}(\beta)Y_l^m(\theta,\phi) \end{aligned} \tag{7.B.2}$$

According to Eq. (7.B.2), the 4D HSH are even for even-valued n and odd for odd-valued n.

Chapter 8

Concluding Remarks

8.1 Summary and Discussion

The BFOR algorithm provides multiple b-value imaging with a solid framework that allows for the fast, analytical computation of various quantitative metrics and the EAP. It does not require dense sampling like DSI, and seems to work well with hybrid sampling schemes. Unlike DTI, BFOR does not invoke any assumptions on the underlying diffusion process and can successfully resolve white matter intersections.

In the same vein as BFOR, the 4D hyperspherical interpretation models the diffusion signal in terms of an orthonormal basis, namely the 4D HSH, and does not require a specific assumption of diffusion behavior. With respect to BFOR, it gives as good a signal and better diffusion ODF reconstructions using fewer fitting parameters. However, a major limitation of the method is that the intricacy of Eq. (7.3.12) may make it impossible to derive the EAP analytically. In addition, stereographic projection onto

the hypersphere destroys the inherent symmetry of the q-space signal.

A major impediment to wide clinical use of multiple b-value imaging, and hence BFOR, is the scan time. A clinically feasible scan time is 4-6 minutes. The HYDI sampling schemes described in Tables 5.4.4, 6.1, and 7.2 - 5 b-values and 125 diffusion-weighted directions - have an approximate scan time of 15 minutes. The utilization of compressed sensing within the BFOR framework is one possible route to reduce the scan time. Optimization of the HYDI sampling scheme could also potentially result in faster acquisitions. With respect to sampling in dMRI, however, there are several significant and unresolved issues:

1. What is the optimal number of b-values? Are 5 b-values, the number used in HYDI, adequate or sub-optimal?

2. What is the optimal b_{max}? Is there anything gained by going up to very high b-values, i.e. $b \geq 9000$ s/mm^2, where the SNR becomes extremely low? A very high b_{max}, tantamount to a very large q-value, could improve the accuracy of the radial integration in Eq. (7.2.1) when computing the EAP, and so result in a more accurate EAP.

3. Is is better to acquire the same number of directions for each b-value or vary them as in HYDI?

The answers to these questions also depend on whether one is solely interested in computing quantitative q-space indices or reconstructing the EAP.

8.2 Ongoing Work

When browsing the dMRI literature, one finds a complete absence of works regarding clinical application of analytical EAP schemes (the small clinical study discussed in Chapter 5 is the first and only work thus far). Clinical validation of a new method is crucial for its adoption by the research community and so, with respect to BFOR, it is imperative that this deficiency in the literature be rectified. We are currently carrying out a study examining the effects of aging in the human brain on BFOR-derived q-space metrics in a cohort of older adults (age: 50-75 years) comprising about 50 individuals. Only two studies to date have been done investigating cerebral age effects on q-space metrics. The first study [21] looked at changes in q-space measures with age in children and yougn adults (age range: 4 months to 23 years), and found that Po increases and MSD decreases with brain maturation, but these trends then plateau during adolescence. The second and more recent study [83] looked at age effects on q-space metrics beyond young adulthood (age range: 18 to 72 years), and found both Po and MSD to be stable across the age range. However, the latter study consisted of a larger number of young and middle-aged adults (18 to 43 years) than older adults, and so its findings may not be representative for a cohort of older individuals.

In any neuroimaging study, such as the BFOR age study, spatial normalization of the brain data is needed in order to perform voxel-based analysis. However, spatial normalization of multiple b-value data is an open question. The current approach is to simply register the EAP-derived indices, specifically Po [83], but such a route does not take advantage of the full EAP information. Recall that the EAP is a rich diffusion descriptor, containing both the radial and angular contents of the diffusion profile, and so it would be advantageous for any multiple b-value registration algorithm to fully exploit the

EAP. Recently, the authors in [40] pursued such a route, developing a large deformation diffeomorphic metric mapping (LDDMM) algorithm to align HYDI datasets using the BFOR signal basis, termed LDDMM-HYDI. Specifically, LDDMM-HYDI involves applying the deformation diffeometric operation on the BFOR expansion coefficients, and it was used to create the first ever HYDI-based *Po* and EAP atlases comprising seven subjects. LDDMM-HYDI illustrates another useful application of the BFOR algorithm, in addition to EAP reconstruction and computation of quantitative indices. Spatial normalization of the HYDI-BFOR data in the age study is being done via LDDMM-HYDI, and so will allow us to expand the *Po* and EAP atlases made in [40], with the intent of creating a q-space brain template that can be used in future multiple b-value imaging studies.

References

[1] Aganj, I., Lenglet, C., Sapiro, G., Yacoub, E., Ugurbil, K., Harel, N.: Reconstruction of the orientation distribution function in single- and multiple-shell q-ball imaging within constant solid angle. Magn. Reson. Med. 64, 554–566 (2010)

[2] Alexander, A.L., Hasan, K.M., Lazar, M., Tsuruda, J.S., Parker, D.L.: Analysis of partial volume effects in diffusion-tensor MRI. Magn. Reson. Med. 45, 770–780 (2001)

[3] Alexander, A.L., Lee, J.E., Lazar, M., Field, A.S.: Diffusion tensor imaging of the brain. Neurotherapeutics 4, 316–329 (2007)

[4] Andersson, J.L., Skare, S., Ashburner, J.: How to correct susceptibility distortions in spin-echo echo-planar images: application to diffusion tensor imaging. NeuroImage 20, 870–888 (2003)

[5] Assaf, Y., Basser, P.J.: Composite hindered and restricted model of diffusion (CHARMED) MR imaging of the human brain. NeuroImage 27, 48–58 (2005)

[6] Assaf, Y., Ben Bashat, D., Chapman, J., Peled, S., Biton, I.E., Kafri, M., Segev, Y., Hendler, T., Korczyn, A.D., Graif, M., Cohen, Y.: High b-value q-space analyzed

diffusion-weighted MRI: application to multiple sclerosis. Magn. Reson. Med. 47, 115–126 (2002)

[7] Assaf, Y., Cohen, Y.: Non-mono-exponential attenuation of water and n-acetyl aspartate signals due to diffusion in brain tissue. J. Magn. Reson. 131, 69–85 (1998)

[8] Assaf, Y., Cohen, Y.: Assignment of the water slow-diffusing compartment in the central nervous system using q-space diffusion MRS: implications for fiber tract imaging. Magn. Reson. Med. 43, 191–199 (2000)

[9] Assaf, Y., Freidlin, R.Z., Rohde, G.K., Basser, P.J.: New modeling and experimental framework to characterize hindered and restricted water diffusion in brain white matter. Magn. Reson. Med. 52, 965–978 (2004)

[10] Assaf, Y., Mayk, A., Cohen, Y.: Displacement imaging of spinal cord using q-space diffusion-weighted MRI. Magn. Reson. Med. 44, 713–722 (2000)

[11] Assemlal, H.E., Campbell, J., Pike, B., Siddiqi, K.: Apparent intravoxel fibre population dispersion (FPD) using spherical harmonics. In: MICCAI. pp. 157–165 (2011)

[12] Assemlal, H.E., Tschumperlé, D., Brun, L.: Efficient and robust computation of PDF features from diffusion MR signal. Med. Image Anal. 13, 715–729 (2009)

[13] Assemlal, H.E., Tschumperlé, D., Brun, L.: Evaluation of q-space sampling strategies for the diffusion magnetic resonance imaging. In: MICCAI. pp. 482–489 (2009)

[14] Assemlal, H.E., Tschumperlé, D., Brun, L., Siddiqi, K.: Recent advances in diffusion MRI modeling: angular and radial reconstruction. Med. Image Anal. 15, 369–396 (2011)

[15] Bar-Shir, A., Avram, L., Ozarslan, E., Basser, P.J., Cohen, Y.: The effect of the diffusion time and pulse gradient duration ratio on the diffraction pattern and the structural information estimated from q-space diffusion MR. J. Magn. Reson. 194, 230–236 (2008)

[16] Bar-Shir, A., Ducan, I.D., Cohen, Y.: QSI and DTI of excised brain of the myelin-deficient rat. NeuroImage 48, 109–116 (2009)

[17] Basser, P.J.: Relationships between diffusion tensor and q-space MRI. Magn. Reson. Med. 47, 392–397 (2002)

[18] Basser, P.J., Mattiello, J., LeBihan, D.: MR diffusion tensor spectroscopy and imaging. Biophysical Journal 66, 259–267 (1994)

[19] Basser, P.J., Pierpaoli, C.: Microstructural and physiological features of tissues elucidated by quantitative-diffusion-tensor MRI. J. Magn. Reson. 111, 209–219 (1996)

[20] Behrens, T.E., Berg, H.J., Jbabdi, S., Rushworth, M.F., Woolrich, M.W.: Probabilistic diffusion tractography with multiple fiber orientations: what can we gain? NeuroImage 34, 144–155 (2007)

[21] Ben Bashat, D., Ben, S.L., Graif, M., Pianka, P., Hendler, Y., Cohen, Y., Assaf, Y.: Normal whtie matter development from infancy to adulthood: comparing diffusion tensor and high b value diffusion weighted MR images. J. Magn. Reson. Imaging 21, 503–511 (2005)

[22] Bloch, F.: Nuclear induction. Physical Review 70, 460–473 (1946)

[23] Callaghan, P.T.: Principles of Nuclear Magnetic Resonance Microscopy. Oxford University Press, Oxford (1991)

[24] Canales-Rodriguez, E.J., Iturria-Medina, Y., Aleman-Gomez, Y., Melie-Garcia, L.: Deconvolution in diffusion spectrum imaging. NeuroImage 50, 136–149 (2010)

[25] Canales-Rodriguez, E.J., Melie-Garcia, L., Iturria-Medina, Y.: Mathematical description of q-space in spherical coordinates: exact q-ball imaging. Magn. Reson. Med. 61, 1350–1367 (2009)

[26] Caruyer, E., Cheng, J., Lenglet, C., Sapiro, G., Jiang, T., Deriche, R.: Optimal design of multiple q-shells experiments for diffusion MRI. In: MICCAI Workshop on Computational Diffusion MRI-CDMRI'11 (2011)

[27] Caruyer, E., Deriche, R.: Optimal regularization for MR diffusion signal. In: IEEE International Symposium on Biomedical Imaging (2012)

[28] Cheng, J., Ghosh, A., Deriche, R., Jiang, T.: Model-free, regularized, fast, and robust analytical orientation distribution function estimation. In: MICCAI. pp. 648–656 (2010)

[29] Cheng, J., Ghosh, A., Jiang, T., Deriche, R.: Model-free and analytical EAP reconstruction via spherical polar Fourier diffusion MRI. In: MICCAI. pp. 590–597 (2010)

[30] Chung, M.K., Dalton, K.M., Shen, L., Evans, A.C., Davidson, R.J.: Weighted Fourier series representation and its application to quantifying the amount of gray matter. IEEE Transac. Med. Imaging 26, 566–581 (2007)

[31] Clark, C.A., Le Bihan, D.: Water diffusion compartmentation and anisotropy at high b values in the human brain. Magn. Reson. Med. 44, 852–859 (2000)

[32] Cohen, Y., Assaf, Y.: High b-value q-space analyzed diffusion-weighted MRS and MRI in neuronal tissues: A technical review. NMR in Biomedicine 15, 516–542 (2002)

[33] Cook, P.A., Bai, Y., Nedjati-Gilani, S., Seunarine, K.K., Hall, M.G., Parker, G.J., Alexander, D.C.: Camino: open-source diffusion-MRI reconstruction and processing. In: Proc. Intl. Soc. Mag. Reson. Med. (2006)

[34] Cory, D.G., Garroway, A.N.: Measurement of translational displacement probabilities by NMR: an indicator of compartmentation. Magn. Reson. Med. 14, 435–444 (1990)

[35] Cucurella, M.G., Rovira, A., Rio, J., Pedraza, S., Tintore, M.M., Montalban, X., Alonso, J.: Proton magnetic resonance spectroscopy in primary and secondary progressive multiple sclerosis. NMR Biomed. 13, 57–63 (2000)

[36] Descoteaux, M., Angelino, E., Fitzgibbons, S., Deriche, R.: Regularized, fast, and robust analytical q-ball imaging. Magn. Reson. Med. 58, 497–510 (2007)

[37] Descoteaux, M., Deriche, R., LeBihan, D., Mangin, J. F., Poupon, C.: Multiple q-shell diffusion propagator imaging. Med. Image Anal. 15, 603–621 (2011)

[38] Domokos, G.: Four-dimensional symmetry. Physical Review 159, 1387–1403 (1967)

[39] Du, J., Goh, A., Qiu, A.: Diffeomorphic metric mapping of high angular resolution diffusion imaging based on riemannian structure of orientation distribution functions. IEEE Transac. Med. Imaging 31, 1021–1033 (2012)

[40] Du, J., Hosseinbor, A.P., Chung, M.K., Bendlin, B.B., Suryawanshi, G., Alexander, A.L., Qiu, A.: Diffeomorphic metric mapping of hybrid diffusion imaging based BFOR signal basis. In: IPMI (2013)

[41] Fock, V.: Zur theorie des wasserstoffatoms. Z. Physik 98, 145–154 (1935)

[42] Frank, L.R.: Anisotropy in high angular resolution diffusion-weighted MRI. Magn. Reson. Med. 45, 935–939 (2001)

[43] Ghosh, A., Deriche, R.: Fast and closed-form ensemble-average-propagator approximation from the 4th-order diffusion tensor. In: IEEE International Symposium on Biomedical Imaging (2010)

[44] Haselgrove, J.C., Moore, J.R.: Correction for distortion of echo-planar images used to calculate the apparent diffusion coefficient. Magn. Reson. Med. 36, 960–964 (1996)

[45] Hess, C.P., Mukherjee, P., Han, E.T., Xu, D., Vigneron, D.B.: Q-ball reconstruction of multimodal fiber orientations using the spherical harmonic basis. Magn. Recon. Med. 56, 104–117 (2006)

[46] Hosseinbor, A.P., Chung, M.K., Wu, Y.C., Alexander, A.L.: Bessel Fourier orientation reconstruction: an analytical EAP reconstruction using multiple shell acquisitions in diffusion MRI. In: MICCAI. pp. 217–225 (2011)

[47] Hosseinbor, A.P., Chung, M.K., Wu, Y.C., Alexander, A.L.: Bessel Fourier orientation reconstruction (BFOR): an analytical diffusion propagator reconstruction for hybrid diffusion imaging and computation of q-space indices. NeuroImage 64, 650–670 (2013)

[48] Katkovnik, V.: A new method for varying adaptive bandwidth selection. IEEE Transac. Sig. Processing 47, 2567–2571 (1999)

[49] Keiner, J.: Computing with expansions in Gegenbauer polynomials. SIAM J. Sci. Comput. 31, 2151–2171 (2009)

[50] Le Bihan, D.: Molecular diffusion, tissue microdynamics and microstructure. NMR Biomed. 8, 375–386 (1995)

[51] Leary, S.M., Davie, C.A., Parker, G.J.M., Stevenson, V.L., Wang, L.Q., Barker, G.J., Miller, D.H., Thompson, A.J.: Magnetic resonance spectroscopy of normal appearing white matter in primary progressive multiple sclerosis. J. Neurol. 246, 1023–1026 (1999)

[52] Maier, S.E., Vajapeyam, S., Mamata, H., Westin, C.F., Jolesz, F.A., Mulkern, R.V.: Biexponential diffusion tensor analysis of human brain diffusion data. Magn. Reson. Med. 51, 321–330 (2004)

[53] Mair, R.W., Sen, P.N., Hurlimann, M.D., Patz, S., Cory, D.G., Walsworth, R.L.: The narrow pulse approximation and long length scale determination in xenon gas diffusion NMR studies of model porous media. J. Magn. Reson. 156, 202–212 (2002)

[54] Merlet, S., Caruyer, E., Deriche, R.: Impact of radial and angular sampling on multiple shells acquisition in diffusion MRI. In: MICCAI. pp. 113–121 (2011)

[55] Moonen, C.T.W., van Zijl, P.C.M., Le Bihan, D., DesPres, D.: In vivo NMR diffusion spectroscopy. p-31 application to phosphorus metabolites in muscle. Magn. Reson. Med. 13, 467–477 (1990)

[56] Mulkern, R.V., Gudbjartsson, H., Westin, C.F., Zengingonul, H.P., Gartner, W., R., G.C., Robertson, R., W., K., Schwartz, R., Holtzman, D., Jolesz, F.A., Maier, S.E.: Multi-component apparent diffusion coefficients in human brain. NMR Biomed. 12, 51–62 (1999)

[57] Niendorf, T., Dijkhuizen, R.M., Norris, D.G., van Lookeren Campagne, M., Nicolay, K.: Biexponential diffusion attenuation in various states of brain tissue: implications for diffusion-weighted imaging. Magn. Reson. Med. 36, 847–857 (1996)

[58] Nunes, R.G., Jezzard, P., Clare, S.: Investigations on the efficiency of cardiac-gated method for the acquisition of diffusion-weighted images. J. Magn. Reson. 177, 102–110 (2005)

[59] Ozarslan, E., Koay, C., Shepherd, T.M., Blackband, S.J., Basser, P.J.: Simple harmonic oscillator based reconstruction and estimation for three-dimensional q-space MRI. In: Proc. Intl. Soc. Mag. Reson. Med. (2009)

[60] Ozarslan, E., Koay, C.G., Basser, P.J.: Simple harmonic oscillator based estimation and reconstruction for one-dimensional q-space MR. In: Proc. Intl. Soc. Mag. Reson. Med. (2008)

[61] Ozarslan, E., Shepherd, T.M., Vemuri, B.C., Blackband, S.J., Mareci, T.H.: Resolution of complex tissue microarchitecture using the diffusion orientation transform (DOT). NeuroImage 31, 1086–1103 (2006)

[62] Pierpaoli, C., Jezzard, P., Basser, P.J., Barnett, A., Di Chiro, G.: Diffusion tensor MR imaging of the human brain. Radiology 201, 637–648 (1996)

[63] Pruessmann, K.P., Weiger, M., Scheidegger, M.B., Boesiger, P.: SENSE: sensitivity encoding for fast MRI. Magn. Reson. Med. 42, 952–962 (1999)

[64] Rathi, Y., Michailovic, O., Setsompop, K., Bouix, S., Shenton, M.E., Westin, C.F.: Sparse multi-shell diffusion imaging. In: MICCAI. pp. 58–65 (2011)

[65] Saff, E.B., Snider, A.D.: Fundamentals of Complex Analysis with Applications to Engineering and Science. Pearson Education, Inc., 3rd edn. (2003)

[66] Schrödinger, E.: Quantisierung als eigenwertproblem. Annalen der Physik 385, 437–490 (1926)

[67] Skare, S., Andersson, J.L.: On the effects of gating in diffusion imaging of the brain using single shot EPI. Magn. Reson. Med. 19, 1125–1128 (2001)

[68] Stejskal, E., Tanner, J.: Spin diffusion measurements: spin echoes in the presence of a time-dependent field gradient. J. Chem. Phys. 42, 288–292 (1965)

[69] Torrey, H.C.: Bloch equations with diffusion terms. Physical Review 104, 563–565 (1956)

[70] Tournier, J.D., Calamante, F., Gadian, D.G., Connelly, A.: Direct estimation of the fiber orientation density function from diffusion-weighted MRI data using spherical deconvolution. NeuroImage 23, 1176–1185 (2004)

[71] Tournier, J.D., Mori, S., Leemans, A.: Diffusion tensor imaging and beyond. Magn. Reson. Med. 65, 1532–1556 (2011)

[72] Tuch, D.S.: Q-ball imaging. Magn. Reson. Med 52, 1358–1372 (2004)

[73] Tuch, D.S., Reese, T.G., Wiegell, M.R., Makris, N., Belliveau, J.W., Weeden, V.J.: High angular resolution diffusion imaging reveals intravoxel white matter fiber heterogeneity. Magn. Reson. Med. 48, 577–582 (2002)

[74] Turner, R., Le Bihan, D.: Single-shot diffusion imaging at 2.0 tesla. J. Magn. Reson. 86, 445–452 (1990)

[75] Weeden, V.J., Hagmann, P., Tseng, W.Y.I., Reese, T.G., Weisskoff, R.M.: Mapping complex tissue architecture with diffusion spectrum magnetic resonance imaging. Magn. Reson. Med. 54, 1377–1386 (2005)

[76] Werring, D.J., Clark, C.A., Barker, G.J., Thompson, A.J., Miller, D.H.: Diffusion tensor imaging of lesions and normal-appearing white matter in multiple sclerosis. Neurology 52, 1626–1632 (1999)

[77] Wiegell, M.R., Larsson, H.B., Wedeen, V.J.: Fiber crossing in human brain depicted with diffusion tensor MR imaging. Radiology 217, 897–903 (2000)

[78] Wong, S.T.S., Roos, M.S.: A strategy for sampling on a sphere applied to 3D selective RF pulse design. Magn. Reson. Med. 32, 778–784 (1994)

[79] Woolrich, M.W., Jbabdi, S., Patenaude, B., Chappell, M., Makni, S., Behrens, T., Beckmann, C., Jenkinson, M., Smith, S.M.: Bayesian analysis of neuroimaging data in FSL. NeuroImage 45, 173–186 (2009)

[80] Wu, Y.C., Alexander, A.L.: Hybrid diffusion imaging. NeuroImage 36, 617–629 (2007)

[81] Wu, Y.C., Field, A.S., Alexander, A.L.: Computation of diffusion function measures in q-space using magnetic resonance hybrid diffusion imaging. IEEE Transac. Med. Imaging 27, 858–865 (2008)

[82] Wu, Y.C., Field, A.S., Duncan, I.D., Samsonov, A.A., Kondo, Y., Tudorascu, D., Alexander, A.L.: High b-value and diffusion tensor imaging in a canine model of dysmyelination and brain maturation. NeuroImage 58, 829–837 (2011)

[83] Wu, Y.C., Field, A.S., Whalen, P.J., Alexander, A.L.: Age- and gender-related changes in the normal human brain using hybrid diffusion imaging (HYDI). NeuroImage 54, 1840–1853 (2011)

[84] Yeh, C.H., Cho, K.H., Lin, H.C., Wang, J.J., Lin, C.P.: Reduced encoding diffusion spectrum imaging implemented with a bi-Gaussian model. IEEE Transac. Med. Imaging 27, 1415–1424 (2008)